Formability of Polycarbonate

by

Darren Clark

A thesis
presented to University of Waterloo
in the fulfillment of the
thesis requirement for the degree of
Master of Applied Science
in
Mechanical Engineering

Waterloo, Ontario, Canada, 2008

DECLARATION

I hereby declare that I am the sole author of this thesis. This is a true copy of the thesis including any required final versions, as accepted by my examiners.

I understand that my thesis may be made electronically available to the public.

ABSTRACT

Current thermoplastic processing techniques involve high capital costs for moulds and significant use of energy to melt or soften the materials. Single-step process cold forming techniques, such as stretch forming, could be cost effective methods for manufacturing large parts with shallow cross-sections from plastic sheet. The present work is a preliminary investigation of a cold forming technique for polycarbonate.

The objective of this work is to characterize the bulk deformation behaviour of polycarbonate using tensile tests and dome stretch forming tests. Two different molecular weight polycarbonate sheets with 1.6 mm thickness were studied: (i) one with $\overline{M}_w$ = 42,000 g/mol and (ii) the other with $\overline{M}_w$ = 52,000 g/mol. For the latter, 3.2 mm sheets were also studied.

Tensile tests conducted at three different cross-head speeds, i.e., 2, 20 and 200 mm/min showed very similar elastic and plastic deformation properties for the two molecular weights. Correspondingly, the activation volumes at yield were almost identical. There was also negligible difference in the thermophysical properties between the two materials as found by differential scanning calorimetry.

Dome stretch forming tests were conducted on a metal forming machine. Specimens of varying width were tested to give different strain states ranging from deep drawing ($\varepsilon_2 < 0$) to biaxial ($\varepsilon_1 = \varepsilon_2$). The limiting dome height or the maximum level of stretch forming

increases with specimen width. This is due to biaxial deformation which increases the maximum strain. Forming limit diagrams (FLDs) were also constructed from the local strains measured from printed fine circle grid patterns on the polycarbonate sheet surfaces. The FLDs showed common general characteristics with metals except for a few key differences. An area of very few data points was found to lie between the “safe zone” and the “necked zone”. This void was referred to as the “unstable neck formation zone”. It exists because of the large local increases in strain associated with the unstable nature of polymer neck formation.

Much more study is required before polycarbonate can be cold formed at strains below the unstable neck deformation. However, the materials and techniques used in this work have demonstrated that the process can be viable for forming shallow large parts from relatively thin thermoplastic sheet a as long as the local biaxial strains are less than 20%.

ACKNOWLEDGEMENTS

I wish to sincerely thank Dr. Pearl Sullivan for the opportunity that she has provided me and for her help, inspiration and insight throughout this work and my studies.

I'd also like to thank Mr. Norval Wilhelm, Mr. Andy Barber and Mr. Richard Gordon for their technical assistance in testing and setup.

Special thanks to Roger Carrick, Prasad Dasappa, Donna Dykeman, Aaron Law, Jonathan Mui, Allan Rogalsky, and Jack Tang for their help and support.

Financial support from the Ontario Centers of Excellence is gratefully acknowledged.

DEDICATION

This work is dedicated to those whose interests have been piqued in the field of polymers. May they be inspired to pursue their greatest ambitions. Much love and thanks is extended to my family, friends and others who have lent their support and encouragement through this endeavour.

TABLE OF CONTENTS

LIST OF TABLES

LIST OF FIGURES

NOMENCLATURE

42-T1	Material Group 1 (t = 1.59 mm, $\overline{M}_w$ = 42,000 g/mol)
52-T1	Material Group 2 (t = 1.59 mm, $\overline{M}_w$ = 52,000 g/mol)
52-T2	Material Group 3 (t = 3.18 mm, $\overline{M}_w$ = 52,000 g/mol)
α	Constant
α	Thermal Expansion Coefficient
a	Unit Cell Dimension
a	Aging Factor
A	Arrhenius Equation Constant
A	Constant
A_0	Original Area
A_i	Instantaneous Area
A^*	Activation Area
ANOVA	Analysis of Variance
b	Defect Strength
b	Unit Cell Dimension
B_0	Plane-Stress Thickness Threshold
B_c	Plane-Strain Thickness Threshold
$\mathbf{B}$	Backstress Stress Tensor
BPA Model	Boyce-Parks-Argon Model
χ	Mean Jump Time
χ^{-1}	Mean Jump Frequency
C_1	Constant
C_2	Constant

δ	Degree of Yield Transformation
d	Diameter
D_p	Punch Head Displacement
DSC	Differential Scanning Calorimetry
ε	Strain
$\dot{\varepsilon}$	Strain Rate
$\dot{\varepsilon}_0$	Initial Strain Rate
ε_1	Major Strain
ε_2	Minor Strain
ε_{ij}	Triaxial Strains (i,j = x,y,z)
ε_T	True Strain
ε_t	Thickness Strain
ε_w	Width Strain
E	Young's (Elastic) Modulus
E_A	Activation Energy
E_r	Relaxation Modulus
E_s	Zero Stress Activation Energy
ϕ	Angle
ϕ_o	Neutral Angle
F	Load/Force
FLC	Forming Limit Curve
FLD	Forming Limit Diagram
$\mathbf{F}^e$	Elastic Deformation Gradient
f_{max}	Maximum Binding Force
f	Frequency

γ	Shear Strain
$\dot{\gamma}$	Shear Strain Rate
$\dot{\gamma}_0$	Constant
$\dot{\gamma}^P$	Plastic Shear Strain Rate
G	Elastic Shear Modulus
G	Yield Gradient
G	Gibbs Free Energy
G_δ	Yield Gradient at a Given Degree of Transformation
G_r	Strain-hardening Modulus
GPC	Gel Permeation Chromatography
η	Viscosity
η_0	Initial Viscosity
h	Fractional Free Volume
h	Enthalpy
h	Softening Slope
H	Enthalpy
h	Constant
h	Height
$h_{Doolittle}$	Doolittle Fractional Free Volume
I	Identity Matrix
I_1	Principal Stretch Invariant
J	Determinant of Hencky Strain Tensor
K	True Stress-Strain Constant
K	Constant
K_{1c}	Plane-Strain Toughness

k	Rate of reaction
k	Constant
k	Boltzmann Constant
λ	Angle Between Applied Stress and Bond Vectors
λ_n	Draw Ratio
λ_i	Principal Stretches (i = 1,2,3)
λ_{chain}	Stretch of Individual Chain
Λ^P_i	Principal Applied Plastic Stretches (i = 1,2,3)
Λ^P_{chain}	Plastic Stretch of Individual Chain
$\mathtt{L}^{-1}$	Inverse Langevin Funcion
$\mathtt{L}^e$	Fourth Order Tensor Operator
l_0	Original Length
l_i	Instantaneous Length
LDH	Limiting Dome Height
LED	Light Emitting Diode
m	A Non-Fundamental State
$\overline{M}_c$	Critical Molecular Weight Average
$\overline{M}_n$	Number-Average Molecular Weight
$\overline{M}_w$	Weight-Average Molecular Weight
M_v	Viscometric Molecular Weight
M_t	Twist Moment
n	Strain-hardening Exponent
n	Number of Segments
n	Chain Density
N_ρ	Number of Chains

$\sqrt{N}$	Limiting Value of λ_{chain}
p	Pressure
PC	Polycarbonate
PE	Polyethylene
PMMA	Poly(methyl methacrylate)
PS	Polystyrene
PSZ	Plastic Shear Zone
PVC	Polyvinyl Chloride
Θ_l	Equivalent Flow Temperature
ρ_d	Defect Density
ρ_e	Entanglement Density
R	Universal Gas Constant
R	Normal Anisotropy Ratio
R_0	Normal Anisotropy Ratio at 0^o
R_{45}	Normal Anisotropy Ratio at 45^o
R_{90}	Normal Anisotropy Ratio at 90^o
$\overline{R}$	Average Normal Anisotropy Ratio
ΔR	Planar Anisotropy Ratio
$\bar{r}$	Average Molecular Distance
r	Strophon Separation Distance
r_0	Strophon Separation Distance at Minimum Potential Energy
r_p	Punch Radius
σ	Stress
σ_{chain}	Stress of Individual Chain
σ_d	Drawing Stress

σ_i	Principal Stresses (i = 1,2,3)
σ_{ij}	Triaxial Stresses (i,j = x,y,z)
σ_{PR}	Plastic Resistance Stress
σ_{T}	True Stress
σ_{UTS}	Ultimate Tensile Strength
σ_y	Yield Stress
σ_{yc}	Compression Yield Stress
σ_{yt}	Tensile Yield Stress
S	Entropy
s	Athermal Shear Strength
s_{ss}	Steady State Athermal Shear Strength
$\dot{s}$	Athermal Shear Strength Migration Rate
SL EOS	Sanchez-Lacombe Equation of State
SS EOS	Simha-Somcynsky Equation of State
τ	Shear Stress
τ_y	Shear Yield Stress
t	Time
t	Thickness
t_o	Original Thickness
t_f	Final Thickness
T	Temperature
T_{eff}	Effective Temperature
T_g	Glass Transition Temperature
T_{lf}	Liquid Flow Temperature
$\mathbf{T}$	Cauchy Stress Tensor

$\mathbf{T}^*$	Effective Stress Tensor
$\mathbf{T}^{*\prime}$	Deviatoric Stress Tensor of $\mathbf{T}^*$
$U(\phi)$	Energy Required to Move Strophons
U_0	Required Rotational Energy
$\mathbf{U}^e$	Hencky Strain Tensor
v	Oscillation Frequency
V	Volume
$V(r)$	Intermolecular Potential Energy
V^*	Activation Volume
V_0	Potential Energy Minimum
V_a	Specific Volume of Amorphous Region
V_c	Specific Volume of Crystalline Region
V_f	Free Volume
$V_{f\,Doolittle}$	Doolittle Free Volume
V_o	Occupied Volume
$V_{o\,Doolittle}$	Doolittle Occupied Volume
Ω	Pressure Activation Volume
w_o	Original Width
w_f	Final Width
WLF Equation	Williams-Landel-Ferry Equation
x^*	Jump Distance
x_i	Fraction of Flexed to Unflexed Bonds

1 Introduction

1.1 Significance of Work

Cold forming techniques such as stamp forming are widely used in the processing of sheet metal but are less common for thermoplastic sheet. Large thermoplastic parts are usually manufactured by heating to soften or melt plastic material before being moulded into their final forms. The most common technique that only softens plastic sheet stock is vacuum thermoforming. One of the potential advantages of cold forming over thermoforming is the efficiency of the process in terms of operational simplicity and energy consumption. This advantage grows exponentially with the size of the part. Fenders, bumpers, fender flares, rocker panels, etc. are all well suited. The stamping process, for instance, is quick and can typically be performed in seconds, while large moulded parts can take several minutes. Molded parts are also required to be of a certain minimum thickness to ensure good flow through the mold cavity, often leading to unnecessarily thick parts. Other advantages of thermoplastic forming can be seen in the tooling maintenance costs. Compared to metals, thermoplastics are much softer and less rigid requiring small loads during deformation and decreased wear in tooling.

The inherently larger deformability of thermoplastics as compared to metals render them ideal candidates for cold forming especially for making large parts with simple and shallow cross-sections. However, this process has yet to be developed for industrial use due to known instabilities associated with deformation of thermoplastics. A simple

single step process, such as cold stamp forming, would offer a competitive cost advantage for processors of large plastic sheets such as those used in automotive manufacturing. The development of the technique for various plastics, however, needs to begin with a better understanding of the deformation behaviour of plastic sheets.

1.2 Deformation of Polymers

The deformation behaviour of polymers differs greatly from that of metals. Amorphous polymers generally exhibit highly viscoelastic properties. At low temperatures and very low strains (below the yield point), polymers follow the same elastic behaviour as metals, and can be characterized by Hooke's law [1]:

$$\sigma = E\varepsilon \tag{1}$$

At higher temperatures (above or near T_g), the deformation behaviour becomes almost entirely viscous. Intermediate temperatures exhibit behavioural characterstics of both, known as viscoelastic behavior. Most polymers are viscoelastic at room temperature. Figure 1.1 shows the different deformation models. The elastic model acts independent of time, showing instantaneous deformation, while the viscous model is dependant on time [2].

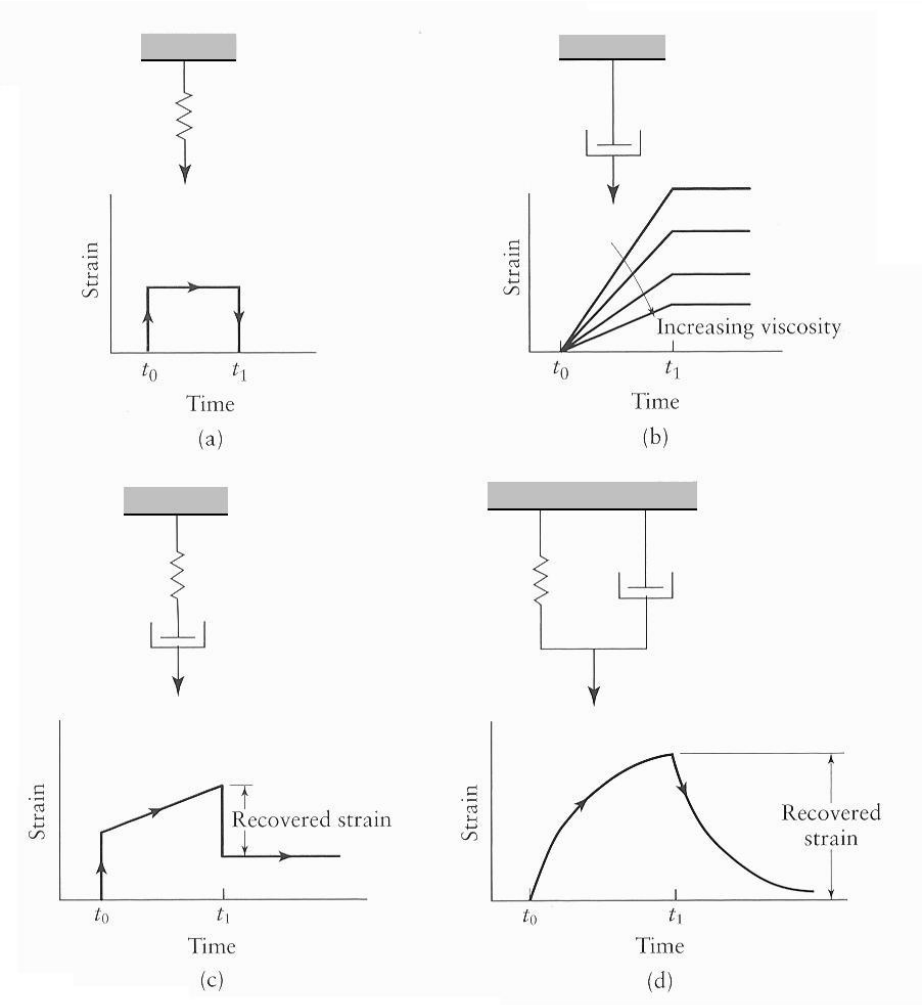

Figure 1.1: Deformation modes based on an instantaneous load applied at time t_0 and removed at t_1. (a) elastic behavior; (b) viscous behavior; (c) Maxwell model; (d) Voight (Kelvin) model. (Reproduced from [2].)

1.2.1 True Stress and True Strain

When considering deformation mechanisms during polymer testing, it is often more meaningful to explore the true stress-strain behavior. The true stress differs from engineering stress greatly after the onset of necking. The main difference is that engineering stress is calculated based on the original cross-sectional area, A_o , while true

stress is a function of the instantaneous cross-sectional area, A_i as shown below, where F is the load being subjected to the given area.

$$\sigma = \frac{F}{A_0} \tag{2}$$

$$\sigma_T = \frac{F}{A_i} \tag{3}$$

The true strain, ε_T, also differs from the engineering strain, and is again, more relevant to deformation processes. Engineering and true strain are respectively defined as:

$$\varepsilon = \frac{l_i - l_0}{l_0} \tag{4}$$

$$\varepsilon_T = \ln\left(\frac{l_i}{l_0}\right) \tag{5}$$

where l_i is the instantaneous length and l_0 the original gauge length. If it is assumed that there is no volumetric change in the material and the cross-sectional area is consistent through the gauge length (ie. $A_i l_i = A_0 l_0$) true stress can be written as a function of the engineering stress and strain:

$$\sigma_T = \sigma(1+\varepsilon) \tag{6}$$

It is important to remember that this relation only holds to the onset of necking.

Figure 1.2 shows the true stress-strain curve deviate gradually from the engineering curve as the neck forms and the cross-sectional area decreases for a metallic material. In comparison as shown in Figure 1.3 the curves deviate rapidly because the neck forms very quickly in polymers.

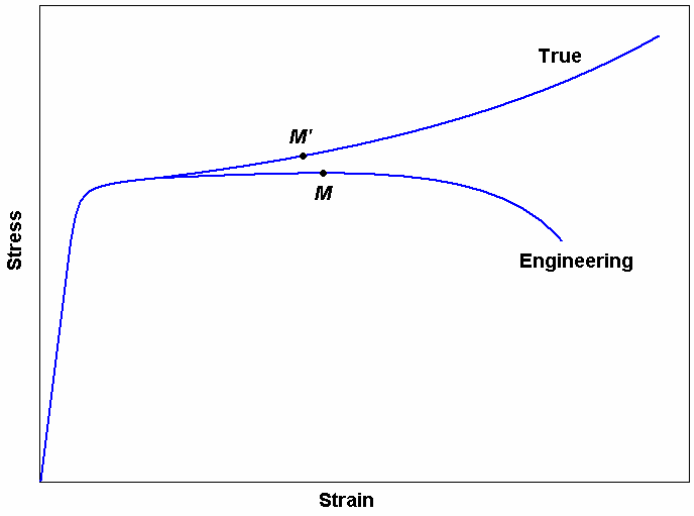

Figure 1.2: Engineering and true stress-strain curves for a typical metal. Necking begins at the maximum engineering stress (point *M*), which corresponds to *M'* on the true stress-strain curve. (Reproduced from [1].)

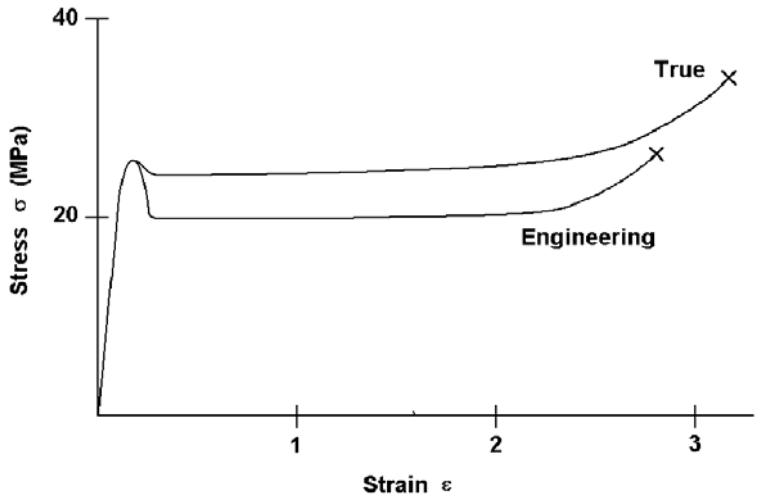

Figure 1.3: Engineering vs. true stress-strain curves for a ductile polymer.

Figure 1.3 also shows that there is an upper and lower yield point present in the true-stress-strain curve, suggesting that part of the drop in engineering stress is due to strain softening, similar to most carbon steels, rather than only necking [3].

1.2.2 Yielding Characteristics

There are a number for different aspects that affect the yield strength and behavior of a material. The state of the stress field will have a significant effect on the yielding behavior. It is always observed that the three fundamental modes of stress result in different yield points. The compressive strength (σ_{yc}) being the highest, shear (τ_y) the lowest, and tensile (σ_{yt}) in the middle. The Tresca yield criteria for the different loading modes are summarized in Figure 1.4. Correspondingly, the true stress-strain curves of the different modes of loading are shown Figure 1.5.

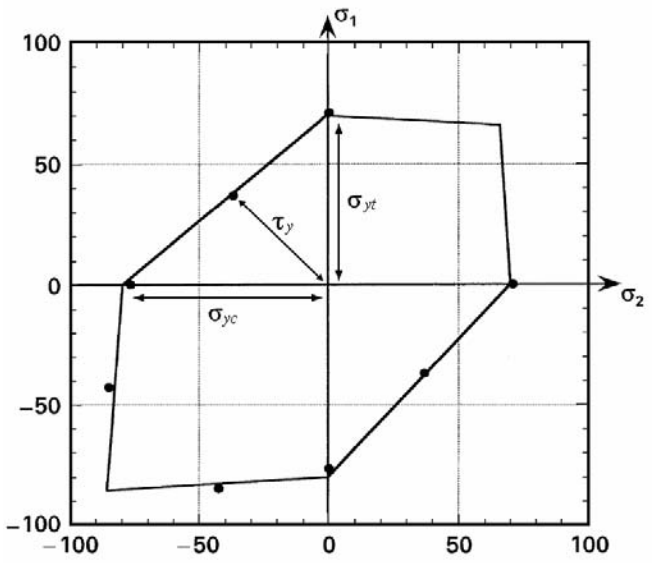

Figure 1.4: A typical Tresca yield criterion diagram shows the three uniaxial yield stresses have following relation: $\sigma_{yc} > \sigma_{yt} > \tau_y$. (Reproduced from [4].)

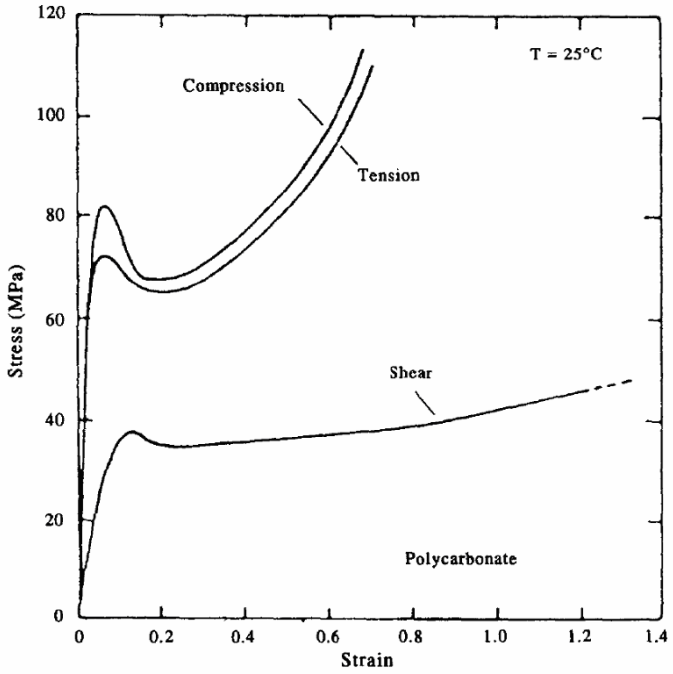

Figure 1.5: True-stress vs. true-strain behavior of polycarbonate (PC) under three modes of deformation: compression, tension and shear. Note that the upper yield point, followed by work hardening in tension and compression is almost non-existent in shear. (Reproduced from [5].)

The yielding behavior in polymers is also very sensitive to the test conditions. It is known that both the temperature and pressure (hydrostatic stress) play a role in determining the yield stress. To explain temperature effect, it is first necessary to define an important physical property of amorphous polymers: the glass transition temperature. The glass transition temperature, T_g, is the point at which the polymer transitions from a rigid material into a leathery material. Below T_g the polymer is said to be glassy, near T_g it becomes leathery, and at temperatures far above T_g the material will turn rubbery.

These ambiguous ranges can be more easily characterized by examining the relaxation modulus, $E_r(t)$ [1].

$$E_r(t) = \frac{\sigma(t)}{\varepsilon_0} \tag{7}$$

where ε_0 is a constant strain, and $\sigma(t)$ is the stress measured over time. Figure 1.6 shows the relation between relaxation modulus and temperature for amorphous polystyrene. T_g occurs at the point of maximum negative slope [1]

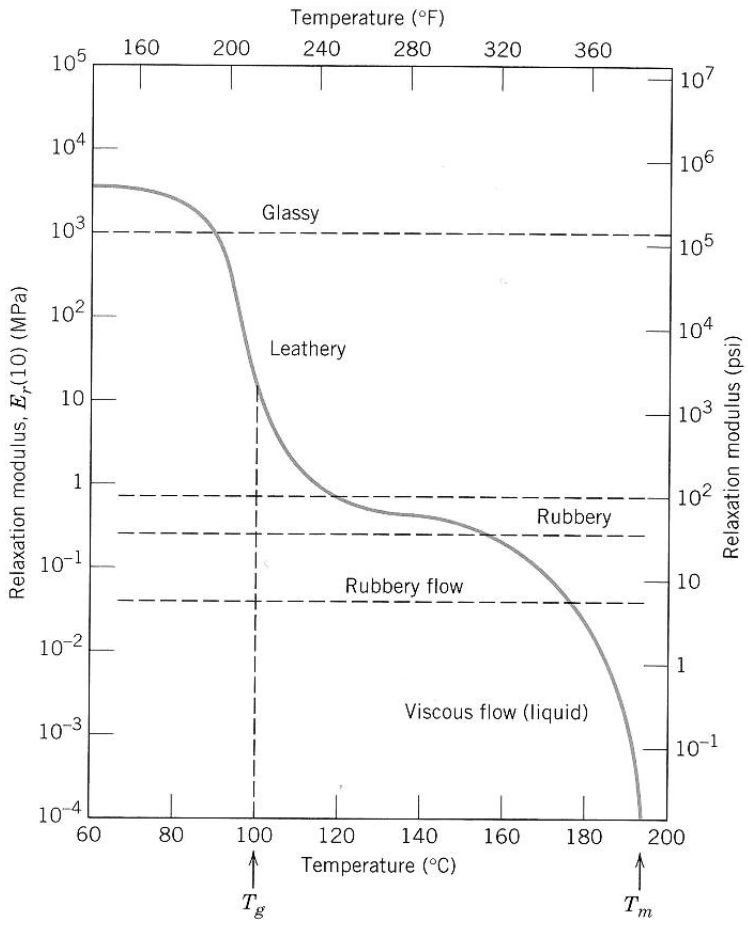

Figure 1.6: Relaxation modulus versus temperature for amorphous polystyrene (PS). (Reproduced from [1].)

To demonstrate temperature dependence, Figure 1.7 shows the behaviour of polycarbonate, a common amorphous thermoplastic, on a shear stress-strain curve. At temperatures below T_g (140^{o}C), the yield stress drops significantly with increasing temperature, though the general shape of the curve does not change [5]. Above the glass transition temperature, however, there is no clear yield point and necking and strain softening do not occur.

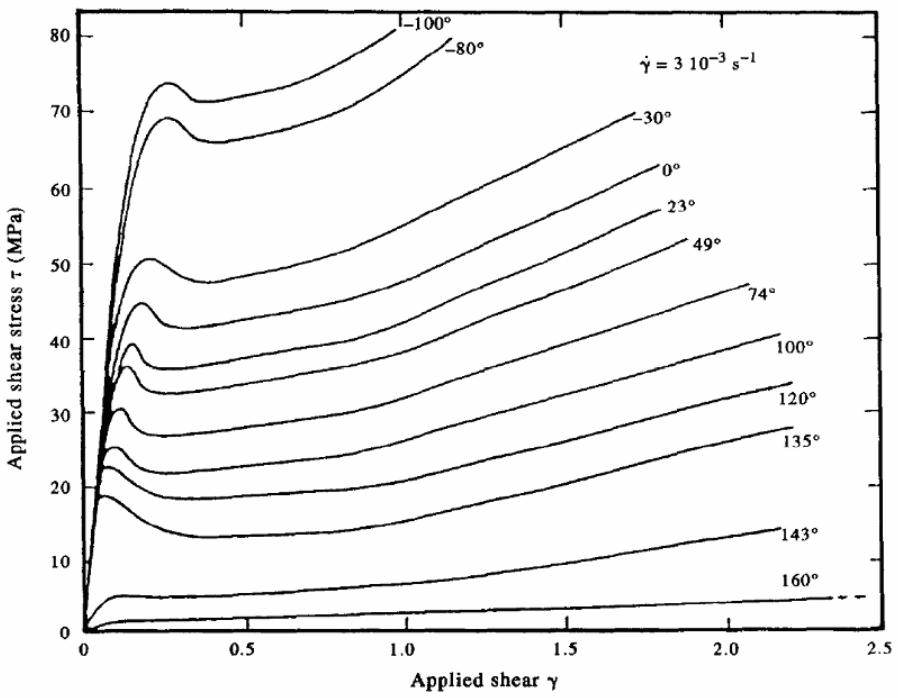

Figure 1.7: Temperature dependence on yield behavior of PC in simple shear at constant shear strain rate ($\dot{\gamma} = 3\times10^{-3}$ s^{-1}). Test temperatures range from: -100°C to 160°C (T_g = 140°C). (Reproduced from [5].)

Increasing the hydrostatic pressure will increase the yield point, ultimate strength and ductility. However, it takes very large pressures to accomplish this. From Figure 1.8 it can be seen that an increase of 450 MN/m^2 in pressure corresponds to an increase in ultimate stress of only ~30 MN/m^2.

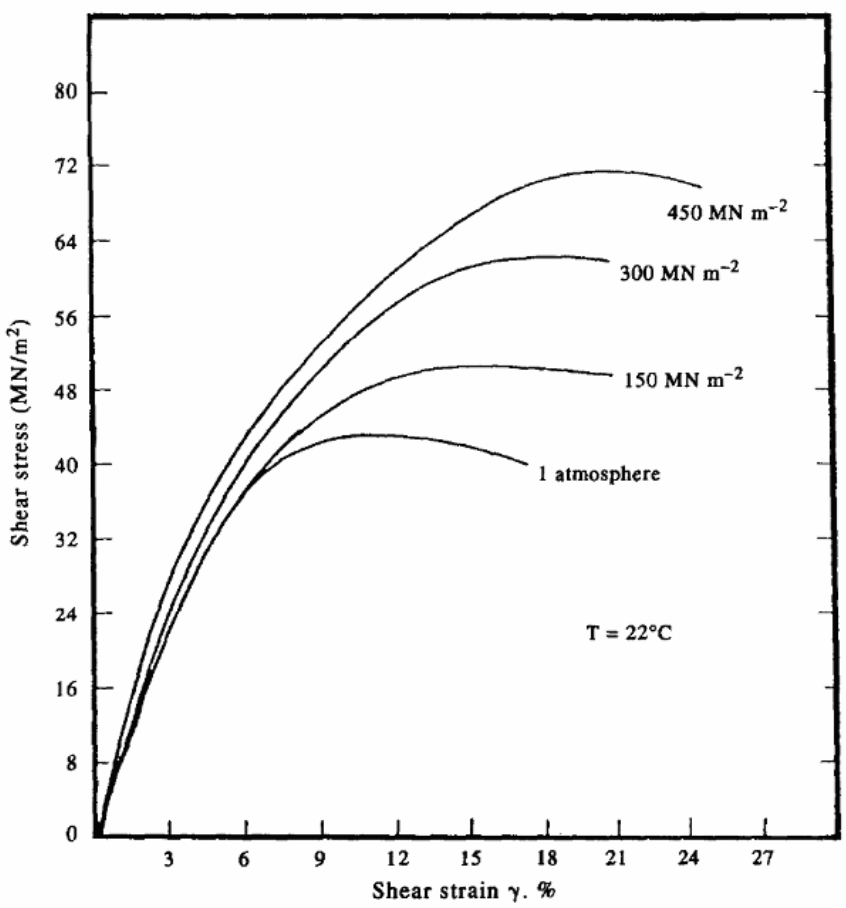

Figure 1.8: Dependence of yield on hydrostatic pressure for PC. Test carried out at room temperature in torsion at constant strain rate. (Reproduced from [5].)

One of the other most important parameters that can effect the yield stress among other things is the strain rate ($\dot{\varepsilon}$). Figure 1.9 shows the effects of altering the strain rate on poly(methyl methacrylate) (PMMA) samples. The higher the strain rate, the higher the yield stress, because the polymer has less time to arrange itself during the test. This is a characteristic of all viscoelastic materials.

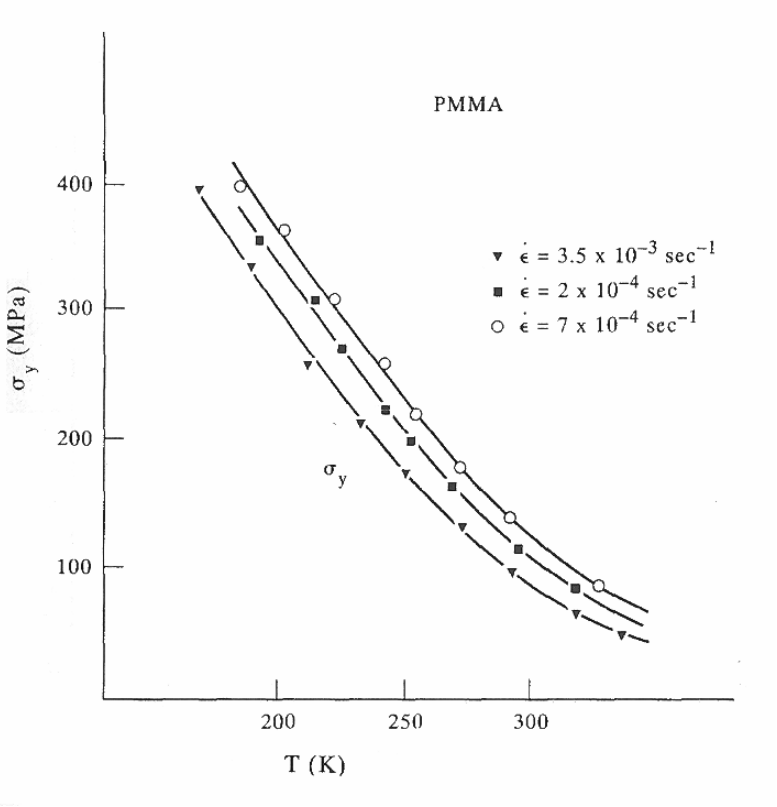

Figure 1.9: Variation of the yield stress with temperature and strain rate for PMMA. (Reproduced from [5].)

1.2.3 Large Strain Deformation

Many polymers are well known for the large amount of deformation that occurs after the yield point. Polyethylene, for example, is known to exhibit large strains on the order of 100-300% [6]. This large strain is typically characterized by four different stages, shown in Figure 1.10. The first stage takes place in the elastic range below the yield point, where the deformation is reversible. The second stage, yielding, occurs at the first peak of the curve. After the initial maximum stress the third stage, unstable neck formation, occurs. A drop occurs in engineering stress because of both strain-softening and the presence of a newly formed neck. The fourth stage, which is important in post yield behavior, is the cold-drawing stage. It occurs after the neck forms and continues until the

necking area has propagated to the ends of the gauge length. The stress at which this phenomenon occurs is called the drawing stress, σ_d. After the neck has reached the end of the gauge length, the specimen will undergo its final stage: strain-hardening leading to fracture [7].

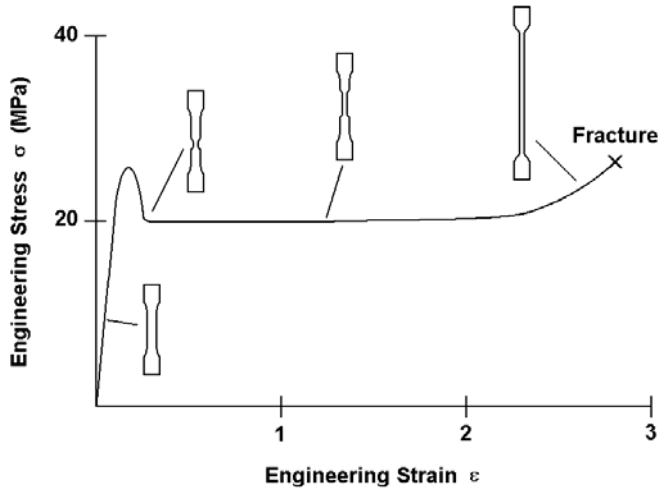

Figure 1.10: Engineering stress-strain curve of polyethylene (PE). σ_d = 20 MPa. (Reproduced from [6].)

One of the most important concepts relating stress-strain curves to the formability of polymers is stability. The unstable neck formation stage is a short period of instability where large local strains increase suddenly up to 60% [8]. This period of neck formation is said to be unstable because once initiated the process does not require an increase in global load or displacement to continue. Beyond the small area of instability, stable neck growth takes over.

Plane-Stress and Plane-Strain

It should also be noted that the state of stress of a part subjected to forming is influenced by part geometry and tool setup. To illustrate, Figure 1.11 shows the generalized stress state [9].

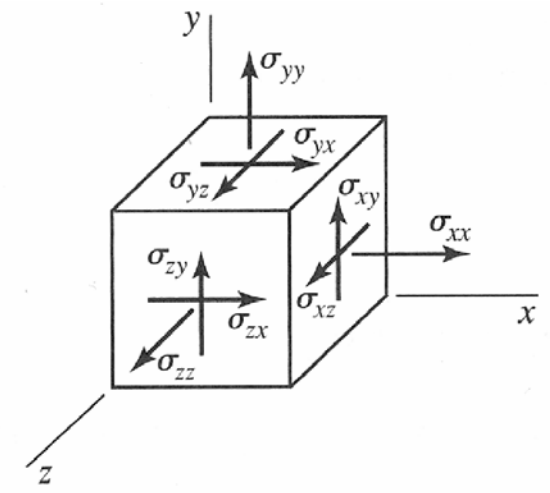

Figure 1.11: Generalized tri-axial stress state. (Reproduced from [9]).

Plane-stress and plane-strain are special stress conditions. Plane-stress usually occurs in thin plates where one dimension in significantly smaller than the other two. The condition for plane-strain is:

$$\sigma_{zz} = \sigma_{zx} = \sigma_{zy} = 0 \tag{8}$$

where σ_{zz}, σ_{zx} and σ_{zy} are stresses defined in Figure 1.11. This isolates the third dimension and simplifies the stress state to two dimensions.

Plane-strain occurs when the strain in one of the dimensions is fixed [10]:

$$\varepsilon_{zz} = \varepsilon_{zx} = \varepsilon_{zy} = 0 \tag{9}$$

where ε_{zz}, ε_{zx} and ε_{zy} are strains defined similarly to the stresses in Eq. **(8)**. The stress state can greatly affect the mechanical properties of the material. For example, the fracture toughness of polycarbonate is dependent on thickness. As seen in Figure 1.12, the fracture toughenss first increases but then gradually decreases as a function of increasing thickness as the stress conditions change from a plane-stress to a plane-strain state [11], .

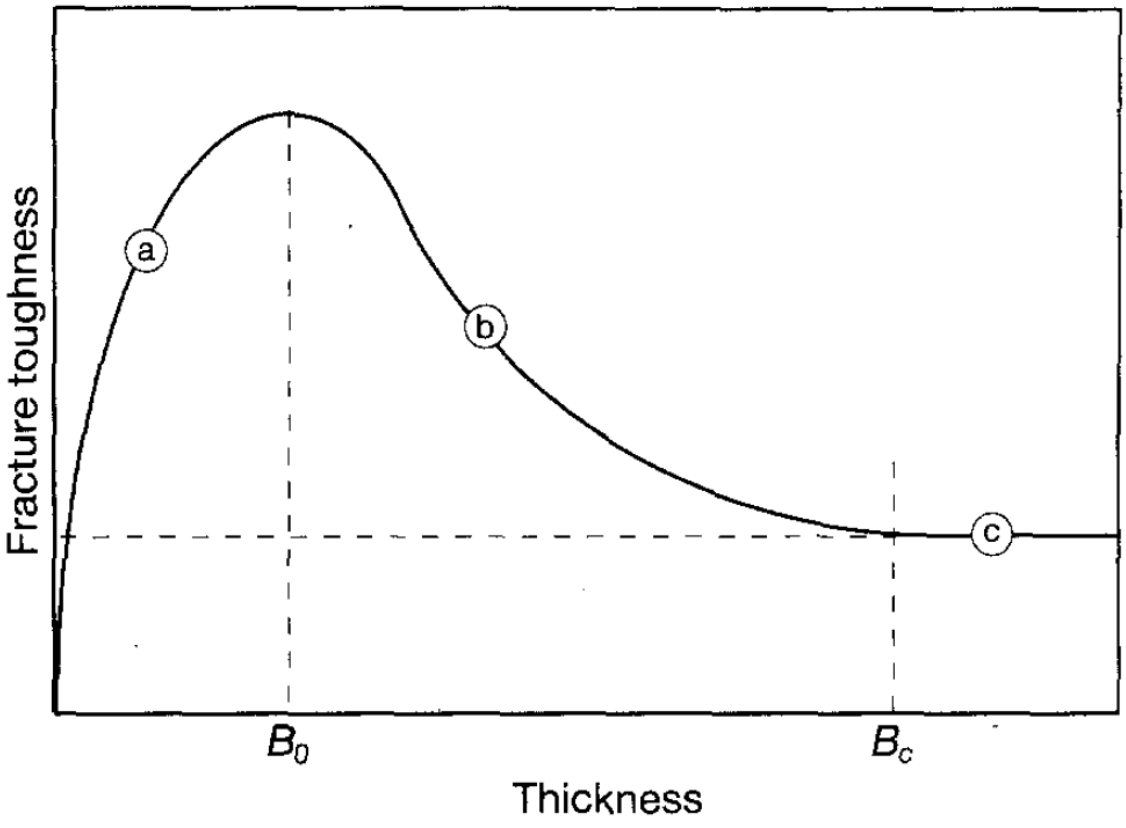

Figure 1.12: Fracture toughness as a function of thickness: (a) pure plane-stress, (b) plane-stress/strain, and (c) pure plane-strain. (Reproduced from [11]).

Points B_0 and B_c represent the threshold at which the stress-strain states change. They are defined in Eq. **(10)** and Eq. **(11)** respectively.

$$B_0 = \frac{1}{3\pi}\left(\frac{K_{1c}}{\sigma_y}\right)^2 \tag{10}$$

$$B_c = 2.5\left(\frac{K_{1c}}{\sigma_y}\right)^2 \tag{11}$$

where K_{1c} is the plane-strain toughness, independent of thickness.

1.3 Formability

The formability of polymers is not as well understood as metals because the pervasive use of melting and moulding processes to manufacture thermoplastics has caused solid state deformation processes to be largely ignored. It is not known if polymers can just as easily be deformed at room temperature like metals and still maintain their formed shape over time given their highly viscoelastic nature.

1.3.1 Metal Forming

Formability of metals is well documented and understood. There are a number of different tests that can be done to determine formability. They are divided into three primary categories: tension tests, torsion tests and compression tests [10]. Because the focus of this investigation is on forming of thin sheet polymer materials, the compression

tests and torsion tests are not relevant. Three main tests, specifically uniaxial tensile tests, limiting dome height (LDH) tests and punch tests are useful for characterizing the formability of sheet materials and will be used in this study.

Tensile Tests

Uniaxial tensile tests can be used to determine the basic mechanical properties of a material, namely the modulus of elasticity, yield stress, ultimate tensile strength, and elongation to failure. All of these can be identified in an engineering stress-strain curve similar to the curve shown in Figure 1.13.

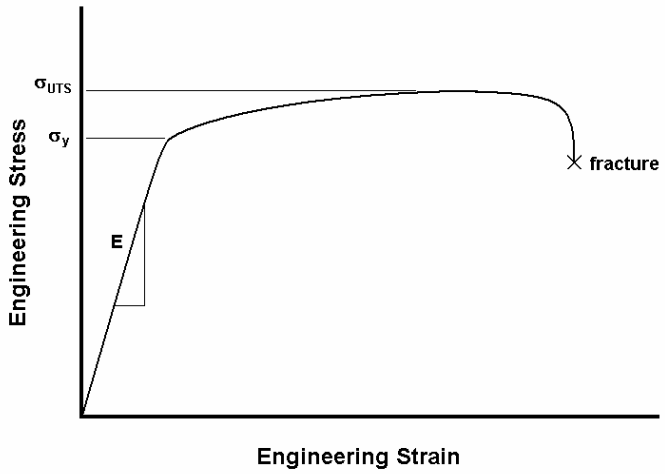

Figure 1.13: Typical engineering stress-strain curve for a metal showing modulus of elasticity, *E*, yield stress, σ_y and ultimate tensile strength, σ_{UTS}.

After necking in most metals, the true stress and strain can be related through Eq. **(12)**.

$$\sigma_T = K\varepsilon_T^n \tag{12}$$

where K is a constant given as the stress at a true strain of one and n is a strain-hardening exponent. The magnitude of the strain- hardening exponent is a measure of the increase in strength obtained from increasing the strain.

Eq. **(12)** can also be written as a logarithmic equation that simplifies the process of calculating the parameters K and n.

$$\log(\sigma_T) = \log(K) + n\log(\varepsilon_T) \tag{13}$$

Figure 1.14 shows the simplification effects that come by changing to a log-log scale though Eq. **(13)**. Notice that there are two distinct sections differing in slope in part (c) of Figure 1.14. The difference is a result from moving from the elastic to plastic range.

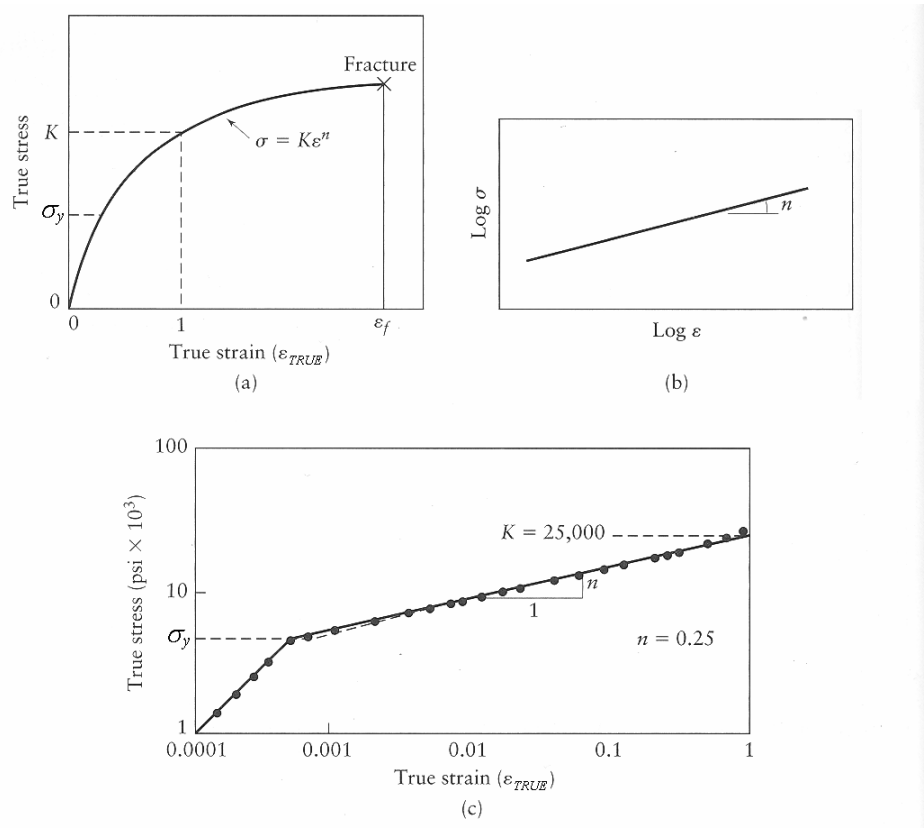

Figure 1.14: True stress-strain curves for: (a) a typical sample curve in tension, (b) a typical sample curve in tension plotted on a log-log scale, (c) 1100-O aluminum plotted on a log-log scale. (Reproduced from [2])

High n values are typically associated with good forming characteristics. The strain-hardening exponent is a measure of how well a material is able to spread out the deformation and avoid localized necking [12]. In metals, a high *n* value will also delay the onset of necking. Metals typically have *n* values in the range of 0.1-0.5 [2]. In comparison, cold-rolled PC had a strain-hardening exponent of 0.22 [13].

Planar anisotropy is another parameter that can be easily derived through tensile tests. Planar anisotropy is a measure of the influence of the direction from which the samples are cut. Often in both polymers and metals, sheets are initially formed by rolling or

extrusion. A sample parallel to the rolling or extrusion direction can often have drastically different mechanical properties than a sample cut perpendicular or at a 45^o angle. The normal anisotropy, *R*, can be calculated by measuring the ratio of strain over the width of the sample to the thickness of the same sample. It is defined in Eq. **(14)**.

$$R = \frac{\varepsilon_w}{\varepsilon_t} = \frac{\ln\left(\frac{w_o}{w_f}\right)}{\ln\left(\frac{t_o}{t_f}\right)} = \frac{\ln\left(\frac{w_o}{w_f}\right)}{\ln\left(\frac{w_f l_f}{w_o l_o}\right)} \tag{14}$$

where the ε_w is the width strain, ε_t is the thickness strain, *w*, *t* and *l* are the width thickness and length respectively and they are denoted as original or final by the subscripts *o* and *f* [2].

The average normal anisotropy ratio, $\overline{R}$, can then be defined as:

$$\overline{R} = \frac{R_0 + 2R_{45} + R_{90}}{4} \tag{15}$$

where the normal anisotropy ratio at the angles 0^o, 45^o and 90^o with respect to the rolling direction are $R_{0,}$ R_{45}, and R_{90} respectively.

In addition to the average normal anisotropy ratio, there is also a parameter known as the planar anisotropy ratio, ΔR.

$$\Delta R = \frac{R_0 - 2R_{45} + R_{90}}{2} \tag{16}$$

If $R_0 = R_{45} = R_{90}$, the planar isotropy ratio will be equal to zero, indicating that the rolling direction has no effect on the deformation of the material. However, if there is a large difference between the individual R values, ΔR will not be equal to zero. The magnitude of this value indicates the influence of rolling direction.

Punch Tests

Punch tests are used to characterize the effects of biaxial strain on the material being tested. Typically a hemispherical punch of 4" or 2" diameter is pushed into a clamped rectangular test piece which has been marked on one surface with a continuous pattern of shall circles or squares. The deformation that takes place can then be measured locally by examining the deformation of specific sections of the grid pattern, or in a more general sense by comparing the position of the punch to the deformation present at failure.

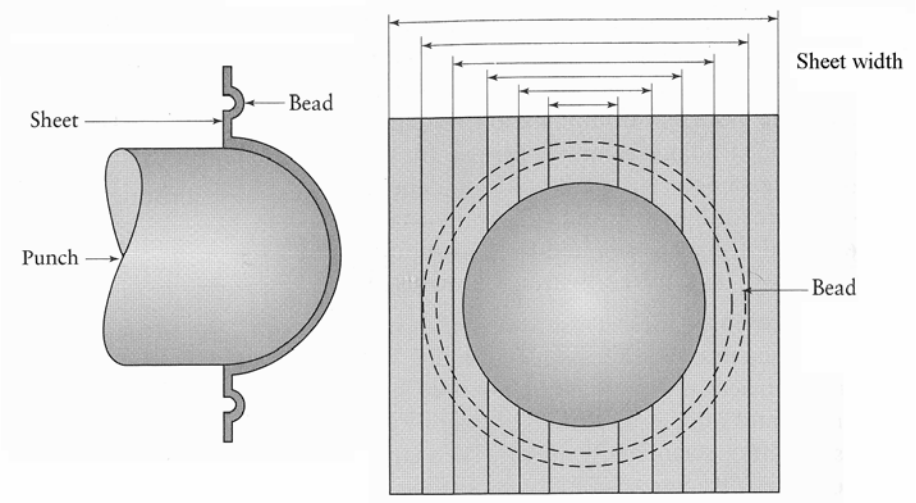

Figure 1.15: Schematic illustration of the punch test on sheet specimens of varying width.

(Reproduced from [2].)

The varying width of sheets, as seen in Figure 1.15 gives different strain conditions ranging from deep draw to pure biaxial strain. With very narrow sheets, deep drawing will occur causing a negative minor strain ($\varepsilon_2 < 0$) with an increase in the major strain ($\varepsilon_1 > 0$). Square sheets will result in biaxial strain with $\varepsilon_1 = \varepsilon_2$. There will be an intermediate width sheet that will provide the plane-strain condition ($\varepsilon_2 = 0$). These three phenomenon are shown in Figure 1.16.

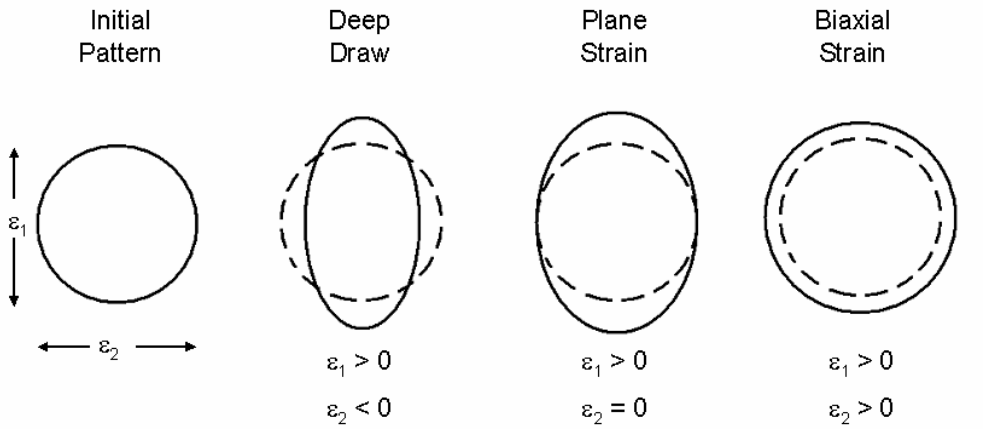

Figure 1.16: Possible changes in shape of the grid pattern caused by forming operations. Initial and final shapes are represented by a dashed line and solid line respectively. (Reproduced from [14].)

A small sample of bulge tests of varying width is shown below in Figure 1.17.

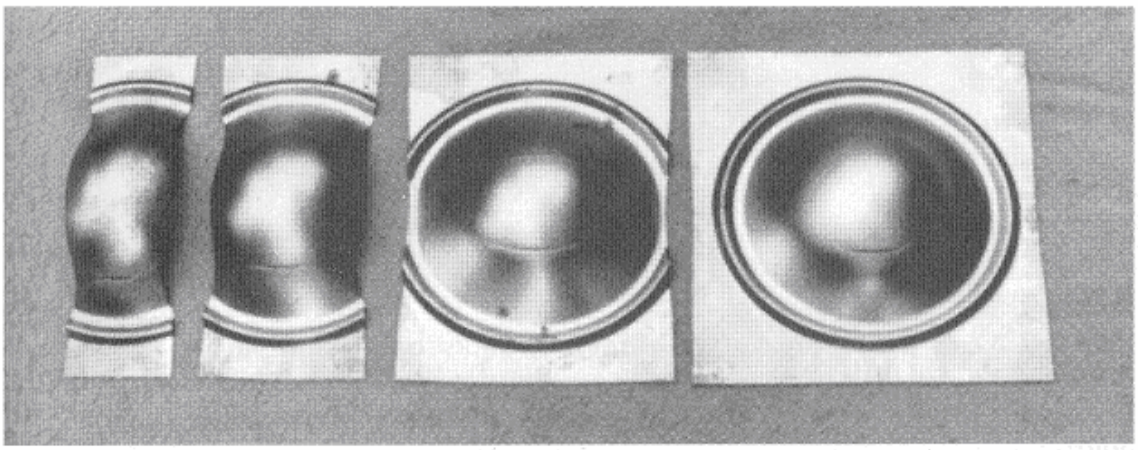

Figure 1.17: Punch test results on steel sheets of various widths. The results range from near uniaxial (farthest left) to pure biaxial stretching (farthest right). (Reproduced from [2].)

Forming Limit Diagrams (FLDs)

Forming limit diagrams have been employed since the early 1960's to help manufacturers and researchers better predict the formability of sheet metals under different deformation criteria [15]. The basic concept behind a FLD is that the major and minor strains are not

independent of one another. The strain to failure along the major axis is a function of the strain in the minor direction (perpendicular to the major axis). A FLD is a plot of the minor strain versus the major strain for many points of varying degrees of failure. Typically, a FLD will be divided into at least two distinct regions: a failure zone consisting of an area where the material is expected to fail if the strains enter this area, and a safe zone where the material is not expected to fail. These zones are sometimes separated by a curve known as the Forming Limit Curve (FLC) [15]. Figure 1.18 shows the FLC for various metals. Note that the failure region for low carbon steels is a wide band rather than a narrow line. This indicates that there is a third "marginal" zone separating failure and safe zones.

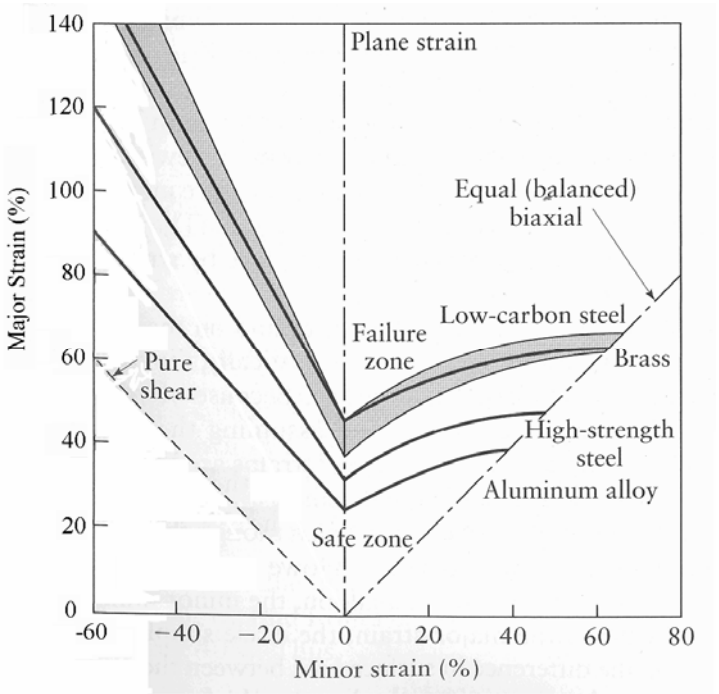

Figure 1.18: Forming limit curves for various metals. The region above the curves is the failure zone. Therefore, the state of strain must remain within the safe zone, below the curves. (Reproduced from [2].)

Limiting Dome Height (LDH)

The limiting dome height is the height of the dome at either the maximum load or failure. LDH tests can be performed using the same specimens as the punch test and can be carried out at the same time as the other punch tests. The LDH test gives a rough idea of the total elongation of the deformed material. It is useful in looking at the properties of the entire piece as opposed to the specific areas examined in FLDs [2].

The limiting dome height can also be converted to an overall strain value along the major strain center line axis. This can be done by considering only a cross-section of the center of the piece. The total distance between the beads is then equated to the final length. It is assumed that the material will follow a path with constant radius equal to the punch radius, r_p, over a given contact angle and a different uniform radius through the rest of the length. This arc radius, r_a, will change with punch head displacement, D_p. A schematic diagram is shown in Figure 1.19 shows the assumptions made. Notice that the original length, l_o, is not equal to the diameter of the punch, because there is a small gap between the bead and the punch.

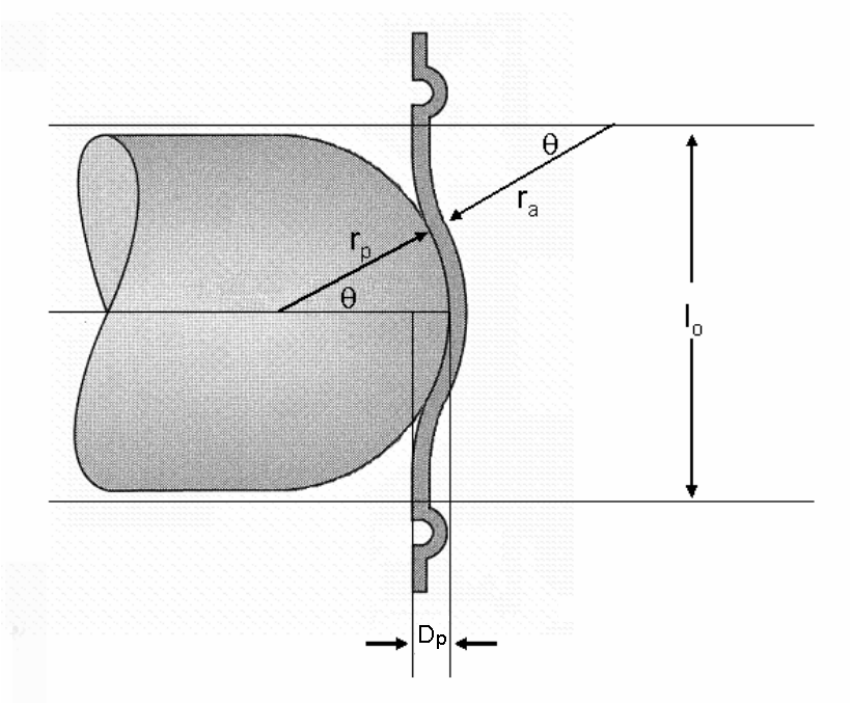

Figure 1.19: Schematic diagram of the punch head.

The instantaneous length, l_i, will be a function of the punch displacement, D_p.

$$l_i = f(D_p) = \theta(r_p + r_a) \tag{17}$$

where θ and r_a are functions of D_p.

By combining equations **(4)** and **(17)** the major strain along the center line can be calculated. From Figure 1.18, it should also be apparent that the major strain at failure increases with increasing minor strain. So, it should be observed that the limiting dome height decreases with decreasing specimen width until the plane-strain condition is met, after which it will begin to increase again.

1.3.2 Forming of Polymers

The properties of polymers contrast those of metals in many different ways. Therefore, forming properties between the two cannot be simply compared. Generally, polymers have very high sensitivity to environmental and testing conditions. The industry standard process for forming of polymer sheets is known as thermoforming.

Thermoforming

Thermoforming involves heating a sheet of plastic to a softening point, typically above T_g, and draping it over a die mould shape to create parts. The most common process, where negative air pressure is employed to help shape the part to that of the die being used, is known as vacuum forming [16]. The opposite process can also be done by adding positive pressure to the top of the sheet and pushing it down to match the die shape. The main problem that occurs as a result of these forming techniques is localized cooling in the polymer as it touches the die surface. This causes wall thinning in parts with a high degree of stretching. Figure 1.20 shows how the degree of stretching can have an adverse effect on the wall thickness.

There are many advanced techniques used in thermoforming, most of which are designed to reduce inconsistency in wall thickness. Plug-assist forming is one such technique that utilizes a plug (or punch) to first deform the material to a shape roughly resembling the final shape. In so doing, the contact area on the plug cools locally, preserving its thickness in the lower corners to a greater extent than traditional vacuum forming [16]. Figure 1.21 illustrates different thermoforming techniques.

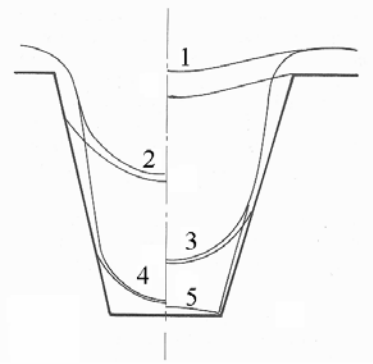

Figure 1.20: Wall thickness variation during draw-down in simple vacuum forming. (Reproduced from Ref. [16].)

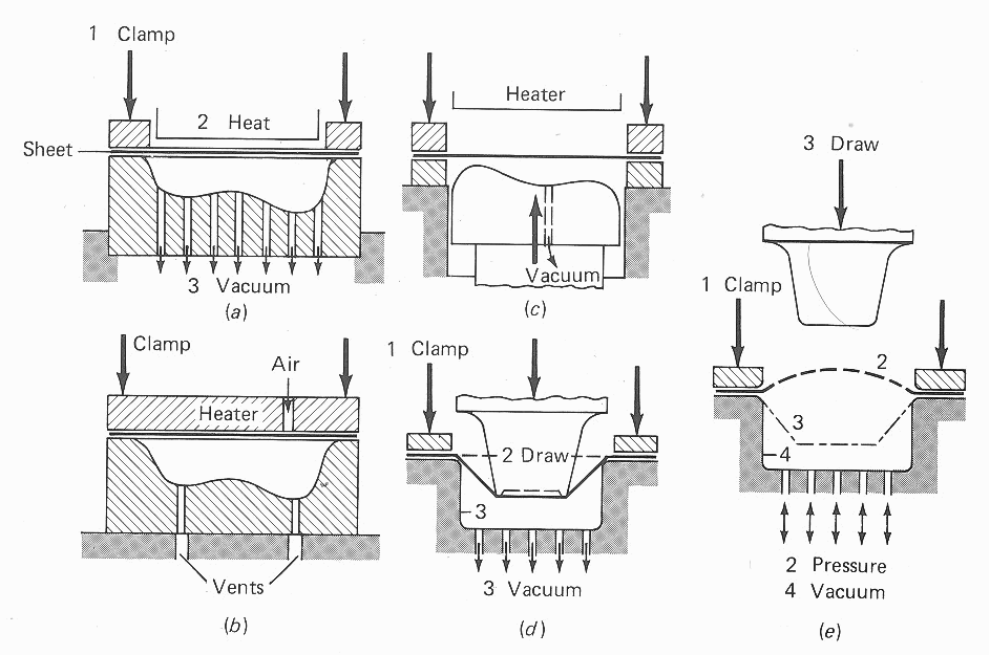

Figure 1.21: Thermoforming processes convert a sheet into a complex shapes by (a) vacuum, (b) pressure, (c) drape-vacuum, (d) plug-assist, and (e) pressure bubble plug-assist methods. Numbers refer to the process sequence. (Reproduced from Ref. [12].)

Comparison to Metal Forming

The main difference between forming techniques typically used for metals and plastics is the absence or presence of heat. Metals, like plastics experience increased ductility and

formability with added heat. However, in metals the softening point is usually extremely high which motivated the development of cold forming processes. In polymers, the softening point is usually quite low (< 200^{o}C) [17] allowing for a relatively simple heating process that makes forming very easy.

There are advantages to both the cold forming processes used for sheet metals and the thermoforming processes of polymers.

Table 1: The advantages and disadvantages of (a) thermoforming and (b) cold forming.

(a) Thermoforming

Advantages	Disadvantages
Increased Formability	Expensive tooling costs (new die for each unique part)
	High energy costs (heating of polymer)
	Alters thermal history
	Variable wall thickness
	Springback

(b) Cold Forming

Advantages	Disadvantages
Cheap tooling costs (incrementally more important with increasing part size)	Decreased formability
	Springback
Low energy costs (no heating of polymer)	
Does not alter thermal history	
Single-step process (rapid production)	

From Table 1, it is clear that the main advantage of thermoforming is increased formability while the main advantage of cold forming is lower cost of processing. Therefore, if the cold formability can either be increased or the design altered to an acceptable level, cold forming should be a cost competitive and viable alternative to thermoforming. The main focus of this study is to determine the limitations of cold forming in an amorphous polymer and explore techniques that might increase these

limits. To achieve this, the most basic theories of deformation have been explored and their effects on the formability of certain polymers quantified.

Other Literature Related to Polymer Forming

Although cold-drawing (necking) and yielding behavior of polymers have been studied extensively, there are currently very few published articles on their formability in the open literature. The use of FLDs and similar techniques has been studied by only a few.

Lee et al. [13] were among the first to publish studies on the formability of polymers. The group investigated formability as a function of the plastic anisotropy ratio, ΔR, and the strain-hardening exponent, n, stating that they governed the polymer's ability to be deep drawn and stretched respectively. Lee et al. studied the effect of cold rolling on formability and concluded that some cold-dolling can improve deep drawability and stretchability due to increases in ΔR and n. In 1989, Lee [18] again studied the effects of cold-rolling on the formability of polymers. This time, Lee used a dome stretch forming test to create FLDs and forming limit curves (FLCs), as seen in Figure 1.22. In 1991, Lee [19] completed yet another study similar to those previous, but with different material.

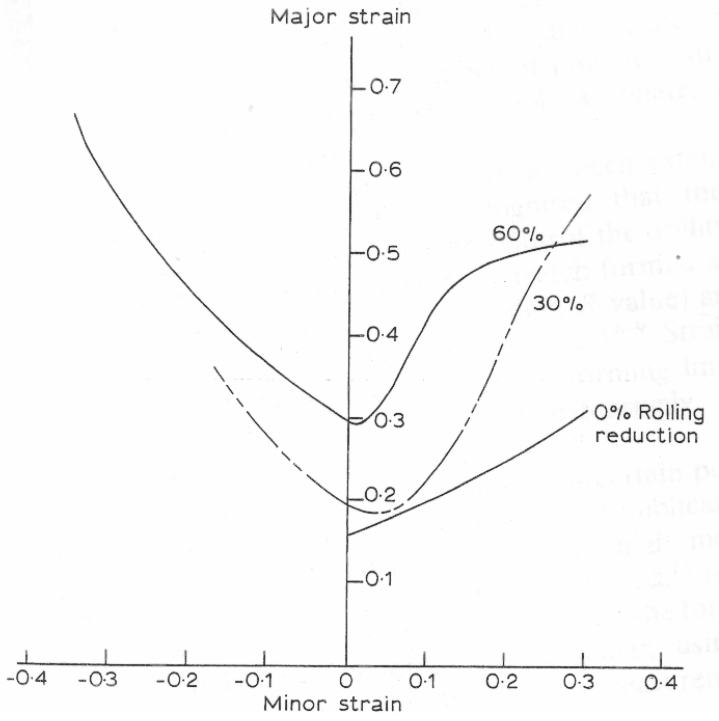

Figure 1.22: Forming limit curve for polyvinyl chloride (PVC) sheets as a function of rolling reduction. (Reproduced from [18].)

More recently [20,21], strain-hardening of polymers has been quantified by a strain-hardening modulus, G_r, rather than n. The strain-hardening modulus is quantified by plotting the yield strength of many polymer samples that were first subject to a given degree of predeformation (rolling reduction). Govaert calculated the strain-hardening modulus based on this type of tests for two different molecular weight polycarbonates at different temperatures. The results are listed in Table 2.

Table 2: Strain-hardening modulus, for two polycarbonates: Lexan® 101 ($\overline{M}_w$ = 30,500 g/mol) and Makrolon® ($\overline{M}_w$ = 18,000 g/mol). (Reproduced from [20].)

Temperature (°C)	Lexan 101 G_r (MPa)	Makrolon G_r (MPa)
25	23.7	23
50	21.3	20.6
75	18.7	17
100	15	13.5
125	10.9	7.6

1.4 Objective and Scope of Study

The primary objective of this work is to characterize the formability of polycarbonate material which is an extremely tough, transparent thermoplastic. This investigation will study two different molecular weight polycarbonates that are commonly used. Tensile and stretch forming tests are conducted to characterize material behavior using stress-strain curves and forming limit diagrams. Forming limit diagrams for two different thicknesses will be constructed to investigate thickness effect. The availability of such diagrams will provide a basis for assessing the feasibility of applying cold forming as a practical technique for processing polycarbonate sheet.

2 Theories on Deformation of Amorphous Polymers

The ultimate goal in any forming process is to be able to accurately predict and control the deformation in order to yield a desired shape with good physical properties. There are a number of theories on the deformation of polymers. Unlike metals which have long-range ordered lattice structures, amorphous polymers do not have well-defined structures that can be simply described. Amorphous polymers lack order among individual polymer chains. Figure 2.1 shows the difference between crystalline (ordered) and amorphous (random) polymer structures. The spaces between the polymer chains allow for increased mobility between chains. These spaces are called the "free volume".

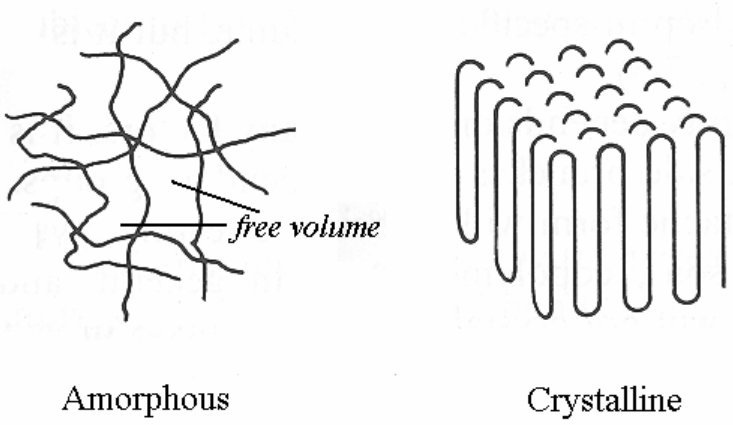

Figure 2.1: Amorphous and crystalline polymer structures. The crystalline structures have higher density (less free volume) than amorphous. (Reproduced from [12].)

The deformation mechanisms of amorphous polymers are complex and cannot be easily characterized using standard microscopic or spectroscopic methods. As will be seen in

this chapter, the various theories offered in the literature are either conceptual models or mathematical expressions describing molecular motion at the atomic level, ranging to molecular, to segmental and finally to bulk scale when the polymer is subjected to the application of stress.

2.1 The Concept of Free Volume

The physical properties of polymers are largely influenced by the effects of temperature and pressure. Free volume theory attempts to explain why and how these conditions influence properties such as yield strength, yield strain, strain at failure, creep rate, formability, ductility, and toughness. [22]. By quantifying the free volume, a better understanding of the polymer's physical behavior can be modeled.

Definition of Free Volume

There is no standard way of defining free volume. There are many different ways of defining free volume depending on the theoretical model that is being used. The first was described by van der Waals in 1873 [23]. Van der Waals explained free volume by using a liquid model, where molecules move within cells. The volume taken up by the molecules, V_o, was considered to be occupied and everything left over volume was called the free volume, V_f. V_f is generally defined as the open, unoccupied space that is found between polymer chains. However, differences arise as a result of the free volume theories which attempt to describe the motion of the molecules. The Simha-Somcynsky equation of state (SS EOS) uses lattice-hole theory to explain free volume, while the

Sanchez-Lacombe equation of state (SL EOS) uses lattice-fluid theory [24]. The lattice-hole theory models changes in free volume mainly by altering the number of unoccupied lattice sites and slightly changing the size of the lattice sites. The lattice-fluid theory has a fixed lattice size and explains changes in free volume only by increasing or decreasing the number of unoccupied lattice sites. Although the SS EOS and SL EOS use Eq. **(18)** to define fractional free volume, *h*, the lattice theories lead to fundamental differences. In lattice-fluid theory the occupied volume, V_o, is constant (ie. no thermal or barometrical volume changes), while in lattice-hole theory, V_o is subject to changes in pressure and temperature [24].

$$h = \frac{V_f}{V} = \frac{V - V_o}{V} \tag{18}$$

where V is the volume as measured conventionally.

Doolittle [25] modeled free volume in polymers as a liquid which defined the occupied volume, $V_{o,}$ as a core volume that the liquid could be reduced to if linearly extrapolated down to absolute zero without a phase change. This core volume included some trapped free space that was not represented as free volume in addition to the molecular volume as theorized by van der Waals. The Doolittle equation [25] also uses a slight variation in its definition of the fractional free volume. Doolittle defined fractional free volume, $h_{Doolittle}$, as the ratio of free volume to occupied volume as seen in Eq. **(19)**.

$$h_{Doolittle} = \frac{V_{f\,Doolittle}}{V_{o\,Doolittle}} = \frac{V - V_{o\,Doolittle}}{V_{o\,Doolittle}} \tag{19}$$

Due to the numerous variations and discrepancies between the free volume theories, it is very important to keep in mind that the variables used to describe free volume (V_f and h) could mean very different things. This must be accounted for when attempting to measure free volume or compare different techniques.

The free volume is dependant on many things. Temperature, hydrostatic pressure and the thermal and mechanical history all affect the free volume present at a given time. Increasing the temperature will also increase the free volume, while increasing pressure will decrease it. Generally, increasing mechanical history (deformation) will also increase the free volume and adding thermal history (annealing) will decrease it. However, complications sometimes arise in these areas. Section 2.4.2 explores the effects of mechanical and thermal history in greater detail.

2.2 Yield Theory

A number of molecular yield theories for polymers are available in the literature. They are very briefly summarized in this section while more details are provided by Stachurski [5] and Ho et al. [26]. Different theories address new considerations or explain specific effects of altering different parameters. The Transition State theory proposed by Eyring will be explored in detail as it will be relevant with the results obtained. The other

theories are provided to strengthen the understanding of yield and highlight shortcomings in Eyring's Transition State theory but are not specifically addressed in the results.

2.2.1 Transition State Theories

Eyring Theory

The Eyring theory for modeling the flow of solids relates the effects of temperature and strain rate to flow stress and the general deformation behavior. The motion of molecules is based on the principle of jumping from one low energy point to another through an energy barrier. Flow is achieved by applying a stress and forcing multiple jumps in the same direction. It is based on the Arrhenius equation (Eq. **(20)**) [27].

$$k = A\exp\left(\frac{E_A}{RT}\right) \tag{20}$$

where k is the rate of reaction, A is a constant, E_A is the energy of activation, R is the universal gas constant and T is temperature. Typically, the Arrhenius equation refers to the rate at which chemical reactions occur based on the temperature and the activation Energy, E_A, for a chemical reaction. By taking this principle and applying it to molecular movement, the rate of reaction, k, can be equated to the strain rate, $\dot{\varepsilon}$. The activation energy, E_A, can be thought of in much the same way: as an energy barrier that needs to be overcome, as illustrated in Figure 2.2.

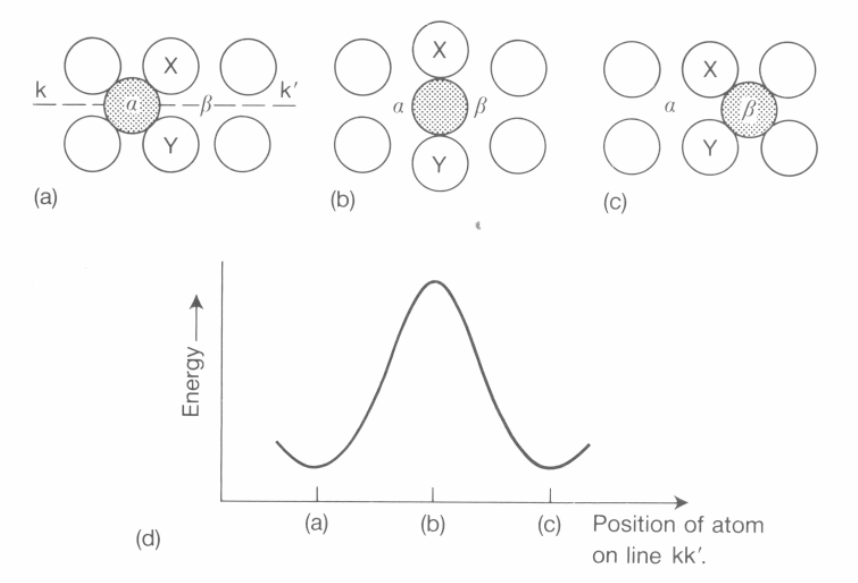

Figure 2.2: The energy required to move the shaded atom from position α to β is directly related to the energy required to temporarily displace atoms X and Y. (Reproduced from [6].)

The atom at position α is assumed to be in a constant state of oscillation with a given probability of ascending the energy barrier and moving from position α to β. In the stress free state, the probability of the atom moving is equal in both directions and extremely low, usually resulting in the atom remaining in its current potential well. The frequency of jumping can be calculated by taking the product of the probability of a jump occurring and the frequency of oscillation. For, example, give a probability of 10^{-16} and an oscillation frequency, *v*, of 10^{13} Hz, we would have:

$$\begin{aligned} mean\ jump\ frequency &= jump\ probability \times oscillation\ frequency \\ &= 10^{-16} \times 10^{13}\ Hz \\ &= 10^{-3}\ Hz \end{aligned}$$

The mean time that an atom would remain in its potential well would be the reciprocal of the mean jump frequency:

$$\chi = \frac{1}{10^{-3}} Hz$$
$$= 10^{3} s.$$

The probability for the occurrence of jumps can be expressed in terms of the Gibbs free energy (ΔG) required to move one mole of atoms/molecules from the bottom to the top of the energy barrier [6].

$$\chi = \frac{1}{v} \exp\left(\frac{\Delta G}{RT}\right) \tag{21}$$

where

$$\Delta G = \Delta H - T\Delta S \tag{22}$$

ΔH and ΔS are the enthalpy and entropy changes required in moving one mole of atoms from the bottom of the potential well to the top [6]. Combining Eqs. **(21)** and **(22)** yields:

$$\chi = \frac{1}{v} \exp - \left(\frac{\Delta S}{R}\right) \exp\left(\frac{\Delta H}{RT}\right) \tag{23}$$

By combining the terms that do not depend on temperature into a common constant, A, we are left with:

$$\chi = A\exp\left(\frac{\Delta H}{RT}\right) \tag{24}$$

The strain rate, $\dot{\varepsilon}$, is proportional to the frequency of jumps, χ^{-1}. Given a new constant, α, we are left with:

$$\dot{\varepsilon} = \alpha\exp-\left(\frac{\Delta H}{RT}\right) \tag{25}$$

One of the key points about the Eyring model is that it allows the shape of the potential well to be altered through the application of a shear stress, τ, as seen in Figure 2.3. The formerly infrequent jumps become common place and occur at an observable rate with the application of a shear stress [6].

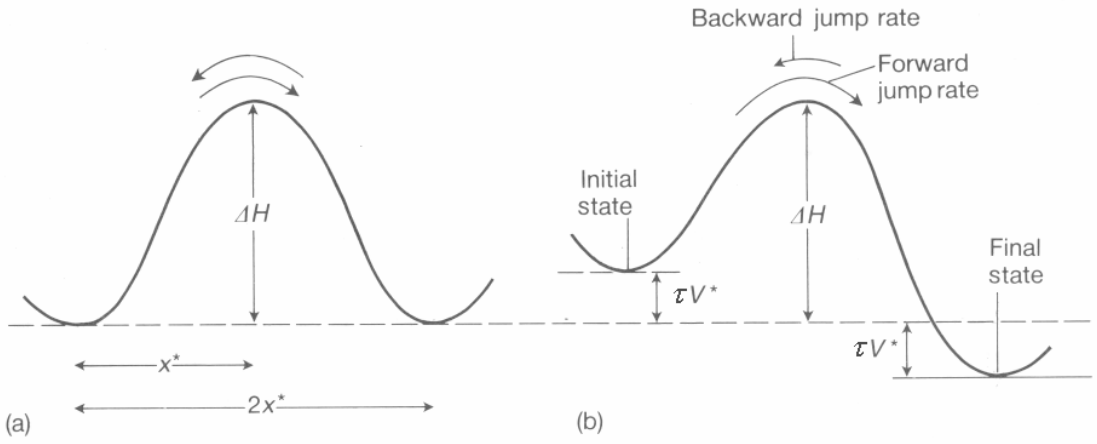

Figure 2.3: Eyring model of solid flow. (a) before stress is applied and (b) after the application of a shear stress. (Reproduced from [6].)

With the application of a shear stress the forward jump rate becomes:

$$\chi_{forward} = A \exp - \left(\frac{\Delta H - \tau V^*}{RT} \right) \tag{26}$$

and the reverse jump rate becomes:

$$\chi_{reverse} = A \exp - \left(\frac{\Delta H + \tau V^*}{RT} \right) \tag{27}$$

where V^* is the activation volume. The net jump rate will be the difference between the forward and reverse jump rates, which will cancel in the equilibrium state (when $\tau = 0$). In the stressed state, however, it gives the net strain rate:

$$\dot{\varepsilon} = \alpha \left[\exp - \left(\frac{\Delta H - \tau V^*}{RT} \right) - \exp - \left(\frac{\Delta H + \tau V^*}{RT} \right) \right] \tag{28}$$

The reverse jump rate is well below that of the jump rate in the equilibrium state, making it negligible in comparison to the forward jump rate. This yields the final strain rate equation in terms of temperature, applied stress and activation volume:

$$\dot{\varepsilon} = \alpha \exp - \left(\frac{\Delta H - \tau V^*}{RT} \right) \tag{29}$$

where V^* is the activation volume defined in Eq. **(30)**. Activation volume is an important concept in Eyring theory. It can be found by equating V^* to an effective activation area, A^*, that must be moved through the distance x^* as seen in Figure 2.3. This gives the V^* the same dimensions as volume, though it is not an actual volume measurement per se, but the product of the distance over which an area has moved. In Figure 2.4 the activation area would be the product of λ_2 and λ_3.

$$V^* = A^* x^* = \lambda_2 \lambda_3 x^* \tag{30}$$

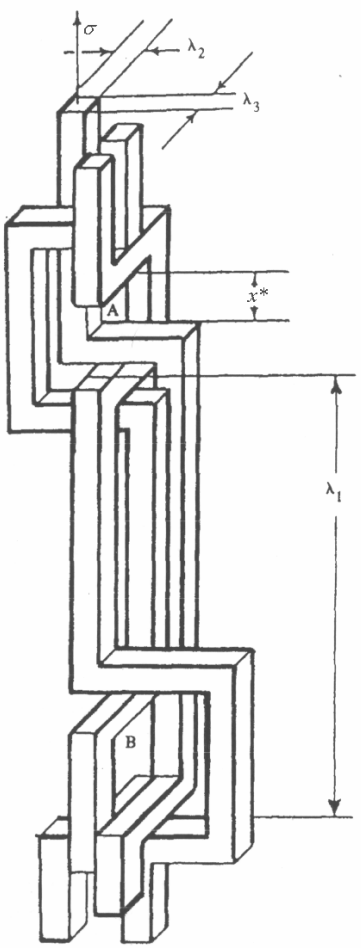

Figure 2.4: Eyring's molecular model of flow in an amorphous polymer. Under an applied load of sufficient magnitude a kink in the molecule will overcome the activation energy barrier and jump to an available hole (at A or B). (Reproduced from [5].)

The activation volume can also be calculated based on tensile tests completed at different testing speeds as shown in Eq. **(31)**. If the slope of the ratio of yield strength to testing temperature versus the logarithmic of strain rate is calculated and input into Eq. **(32)** and **(31)** the activation volume is found.

$$\frac{d(\sigma_y / T)}{d(\log \dot{\varepsilon})} = \frac{2 \times 2.303 \times R}{V^*} \tag{31}$$

where R is the universal gas constant.

Duckett et al. Theory

The effects of hydrostatic pressure are easily observed experimentally (see Figure 1.8). However, these parameters were not taken into account by Eyring. Therefore, Duckett et al. modified the Eyring theory by recognizing the work done by hydrostatic pressure, p, and adding a term to account for it. The modified strain rate relationship can be seen in Eq. **(32)**

$$\dot{\varepsilon} = \alpha \exp - \left(\frac{\Delta H - \tau V^* - p\Omega}{RT} \right) \tag{32}$$

where Ω is the pressure activation volume, similar to the shear stress activation volume proposed by Eyring, V^*. One of the most important conclusions made by Duckett et al. was that the difference between tensile and compressive yielding behaviours was due to the difference in hydrostatic pressure [5]. Because the experiments in this work were completed at atmospheric pressure, the Duckett et al. theory is equivalent to the Eyring theory. At higher pressures, it is recommended that these effects are not ignored.

2.2.2 Free Volume Theories

Rush and Beck Theory

Rusch and Beck proposed that a polymer's deformation response depended on the free volume present. This free volume would "effectively" change the apparent temperature at which the material was being tested. That is, a material tested at a temperature, *T*, will respond as though being tested at T_{eff}.

$$T_{eff} = T + \frac{h}{\Delta\alpha} \tag{33}$$

where *h* is the free volume, based on lattice-hole theory, and $\Delta\alpha$ is the change in thermal expansion coefficient caused by the presence of free volume [5].

Bauwen's Theory

The basis of Bauwen's theory is that a common process generates both plastic deformation and the formation of free volume. Bauwen goes on to make use of the perfect gas law to produce a yield criterion. Yield is said to occur when *n* segments are activated at the same time. The frequency of this event occurring in the unstressed state is [5]:

$$f = \frac{2kT}{h}\left[m\exp\left(-\frac{E_A}{RT}\right)\right]^n \tag{34}$$

where m is any non-fundamental state (capable of creating free volume), E_A is the activation volume for each of n segments and k and h are constants. Accounting for applied stress and hydrostatic pressure, p, the strain rate is given as:

$$\ln \dot{\varepsilon} = K + n \ln m + \frac{1}{RT}\left(E_A - A\tau - np\Delta V_0\right) \tag{35}$$

where ΔV_0 is the change in volume occupied by a segment and K and A are constants [5].

2.2.3 Conformational Change Theories

Robertson's Theory

Robertson assumed that glassy polymers are in a liquid state of extremely low viscosity and that applying a stress will cause viscous deformation by increasing the fluidity of the structure [22]. He also proposed that the state of the bonds between molecules govern viscosity. To do this, it was assumed that covalent bonds can only be in one of two states: 1) an unflexed, low energy state called trans or 2) a flexed, high energy state called cis. Most bonds within a polymer in the glassy state (below T_g) are in a low energy state (trans). Introducing shear stress increases the number of flexed bonds, in turn creating strain via a series of jumps from the flexed state to the unflexed state. The fraction of flexed to unflexed bonds, x_i, is given as:

$$x_i = \frac{\exp\left(-\Delta E_A / kT_g\right)}{1+\exp\left(-\Delta E_A / kT_g\right)} \tag{36}$$

where ΔE_A is the activation energy difference between the high and low energy states. By applying a shear stress at a temperature $T < T_g$, the equilibrium fraction of flexed bonds becomes:

$$x_i = \frac{\exp\left(-(\Delta E - v\tau\cos\lambda)/kT\right)}{1+\exp\left(-(\Delta E - v\tau\cos\lambda)/kT\right)} \tag{37}$$

where the angle λ is the relative angle between the applied stress and bond vectors [22].

The deformation mechanics are governed by the WLF (Williams-Landel Ferry) equation and Newton's constitutive equation. The stress required for plastic deformation is given as:

$$\tau = \eta\dot{\varepsilon} \tag{38}$$

where η is the viscosity.

$$\eta = \eta_0 \exp\left(\frac{-\Delta G(\Theta_1)}{kT}\right) \tag{39}$$

where:

$$\Delta G(\Theta_1) = \frac{C_1 C_2 k \Theta_1}{\Theta_1 - T_g + C_2} \tag{40}$$

C_1 and C_2 are constants and Θ_l is the temperature at which the flowing ability of a liquid phase polymer would be equal to the corresponding solid-phase polymer. Much of Robertson's theory is centered around the Θ_l parameter [5]. It suggests that any solid subjected to a critical minimum load will be changed to a liquid phase allowing plastic flow.

2.2.4 Dislocation/Disclination Theories

Bowden and Raha Theory

Applying a stress gives rise to dislocations which are not present prior to loading within glassy polymers. The stress required to create dislocations is the yield stress. The addition of heat is thought to ease the nucleation process and lower the effective stress the polymer can withstand. Two of the main strengths of Bowden and Raha's model are the inclusion of strain softening after yielding and the absence of σ_y upon immediate reloading. This is due to the energy barrier that must be overcome in order to begin dislocation nucleation [5].

Argon's Theory

Argon's model is centered around the concept that shear plasticity in polymers is similar to that of crystalline metals. Flow in the polymer takes place via propagation of kinks in the polymer chain which form under stress and rotate to orient themselves in the direction of stress [5]. Because kink formation and rotation is the fundamental basis of the model, the activation volume required to produce deformation is extremely small. Figure 2.5 depicts kink formation/propagation.

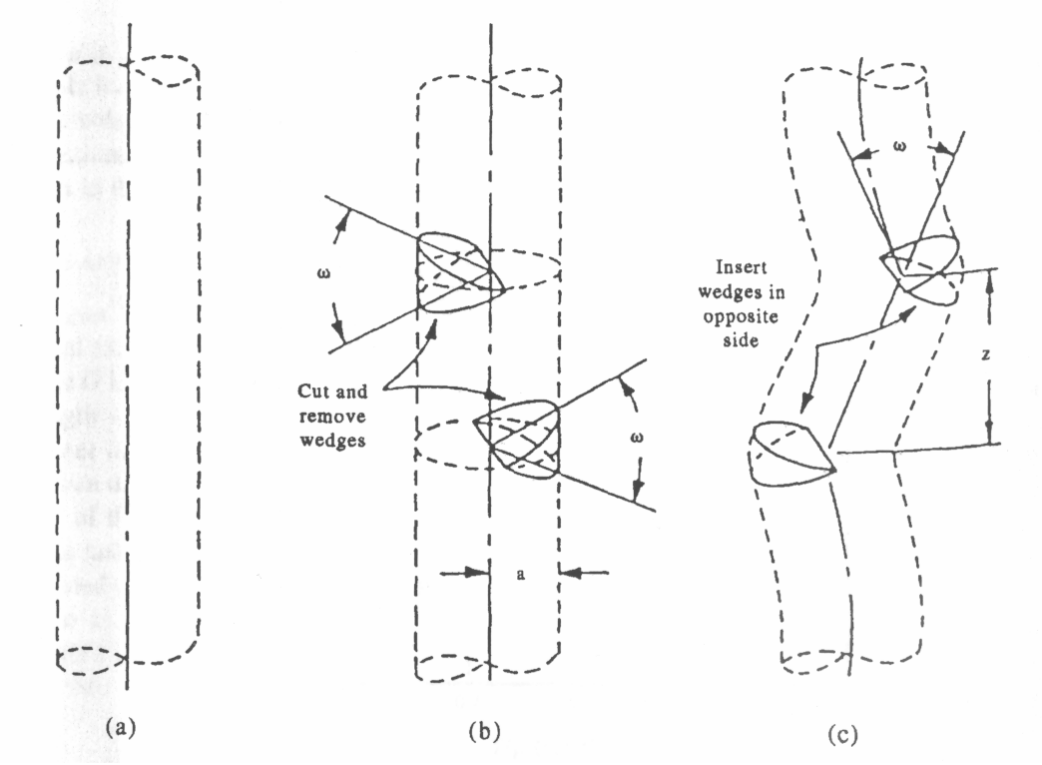

Figure 2.5: The elementary mode of kink propagation by means of disclinations as proposed by Argon. (Reproduced from [5].)

Like other theories, Argon's model is highly sensitive to the effects of temperature and strain rate. Plastic resistance, σ_{PR}, is the stress required to produce plastic flow. It is defined as a function of temperature and strain rate in Eq. **(41)** [5].

$$\sigma_{PR} = Gb\sqrt{\rho_d} \tag{41}$$

where G is the elastic shear modulus, ρ_d is the defect density and b is the strength of the defects. The temperature, T_{lf} at which liquid-like flow will ensue ($\sigma_{PR} = 0$) is:

$$T_{lf} = \frac{1}{bk\ln(\dot{\varepsilon}_0 / \dot{\varepsilon})} \tag{42}$$

where k is the Boltzmann constant. Rearranged for the strain rate, Eq. **(42)** becomes:

$$\dot{\varepsilon} = \dot{\varepsilon}_0 \exp\left(-\frac{1}{bkT_{lf}}\right) \tag{43}$$

2.2.5 Segmental Motion Theories

Yannas Theory

Yannas' model theorizes polymer deformation as a rotational movement of strophons. Strophons being relatively short segments of a polymer joined by covalent bonds. Visible deformation occurs as a result of the motion of many strophons. Many short strophons are connected by hinges to form the larger molecules. The energy required to move the strophons, $U(\phi)$, is [5]:

$$U(\phi) = \frac{U_0}{2}\left[1 - \cos n(\phi - \phi_0)\right] \tag{44}$$

where U_0 is the energy required to ascend the rotational energy barrier and ϕ is the angle measured from a neutral position ϕ_0. The intermolecular potential energy of the strophons is given as the Lennard-Jones potential [5]:

$$V(r) = V_0\left[\left(\frac{r_0}{r}\right)^{12} - 2\left(\frac{r_0}{r}\right)^{6}\right] \tag{45}$$

where V_0 is the potential minimum, r is the strophon separation distance and r_0 is the separation distance at $V = V_0$. The shear modulus, G, can be quantified as a resistance to twist deformation under a moment, M_t:

$$G = \frac{2h}{\pi d^4}\frac{dM_t}{d\phi} \tag{46}$$

where h and d are the height and diameter of the cylindrical strophon. Eq. **(46)** leads into the final governing equation for the system [5]:

$$G = \frac{4h}{\pi d^4}\left(\frac{d^2U(\phi)}{d\phi^2} + \frac{d^2V(r)}{dr^2}\right) \tag{47}$$

Stachurski Theory

Stachurski models amorphous polymers as disordered systems lacking regular "defects" as seen in many other systems [5]. Instead, Stachurski uses the spacing between chains as the basis of the model. This is justified by the fact that any relative movement in 3-D space can be simplified as a 2-D scalar change in distance. The average space between molecules, $\bar{r}$, is denoted as:

$$\bar{r} = \frac{\sqrt{ab/\sqrt{3}}}{1 - \frac{1}{2}\frac{V_a - V_c}{V_c}} \tag{48}$$

where V_a and V_c are the respective specific volumes of the amorphous and crystalline phase and a and b are dimensions of the unit cell.

In contrast to metals and other polymer deformation theories which assume that the strength is a function of the defects found within the structure, Stachurski defines the strength in terms of the maximum binding force, f_{max} which is a function of the molecular bond strength between molecules and chains [5]. The yield strength can then be taken as:

$$\sigma_y = \frac{\alpha N_\rho f_{\max}}{\bar{r}^2} \tag{49}$$

where α is a constant and N_ρ is the number of chains needing to be "unbound" in order to create flow within the matrix. This model is different from the other models in the fact

that it does not directly account for temperature changes, strain rate, shear modulus or matrix defects.

2.2.6 Other Theories

Entanglement Density

The theory proposed by Ho et al. [26] differs from previous theories. The fundamental difference being the fact that other theories generally simplify large polymer chains down to a very small section that can be easily be modeled and have equations applied. However, due to the lack of long-range order this modelling technique is fundamentally flawed [26]. Ho *et al.* model a much larger area called a plastic shear zone (PSZ) in which deformation occurs. This deformation behavior becomes a function of the shear activation volume, V^*, which is governed by the entanglement density, ρ_e.

2.3 Post-Yield Deformation Theory

After yielding most amorphous glassy polymers undergo necking. The formation and propagation of this neck has been largely researched and understanding the cold drawing (necking) process is paramount to understanding and predicting the forming behavior. Cold-drawing behavior of amorphous glassy polymers is a more complex phenomenon than that of polymer yielding.

2.3.1 Constitutive Models of Cold-Drawing

Double Glass Transition Theory

The cold-drawing (necking) phenomenon that occurs within many glassy amorphous polymers has been modeled by Zhou et al. [28] as a process involving two glass transitions. The cold-drawing process is proposed to occur in a series of three steps. First, the polymer undergoes a transition from an isotropic glass to an isotropic rubber at the yield stress. Stretching then occurs in the rubbery state at a relatively constant drawing stress. Lastly, the stretched rubber transitions back to an oriented glass upon unloading, or at a strain where the degree of molecular orientation reaches a certain amount. A schematic diagram of the process can be seen in Figure 2.6.

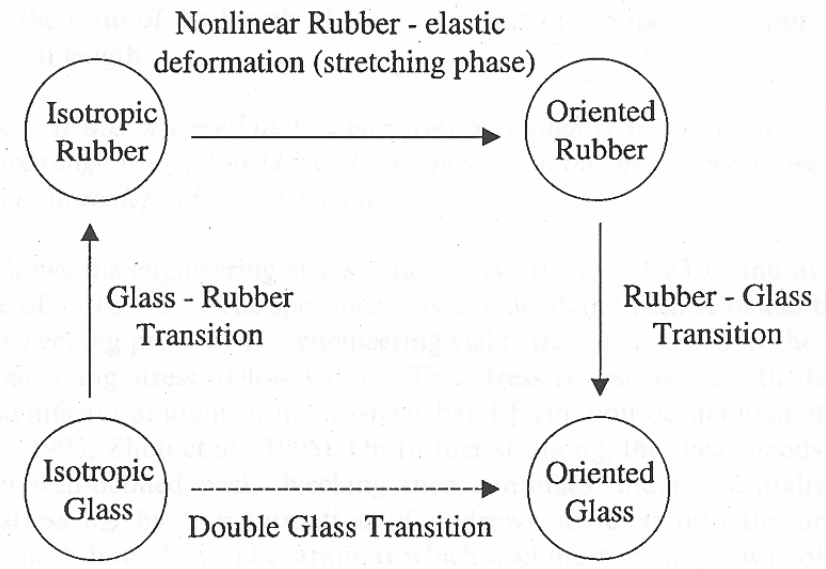

Figure 2.6: Schematic of the double glass transition process. (Reproduced from [29].)

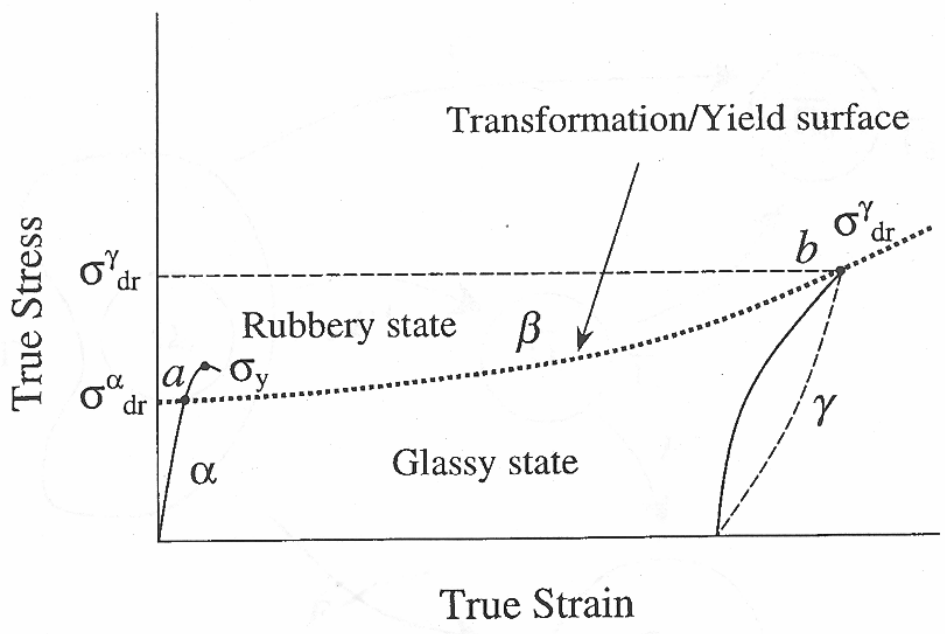

Figure 2.7: The process of cold-drawing as transitions: $\alpha \rightarrow \beta \rightarrow \gamma$. (Reproduced from [29].)

Figure 2.7 shows the true stress-strain behaviour of the material and the points at which the material is in the glassy state and the rubbery state. The gradient, *G*, of this transformation can be expressed at any point in the following equation:

$$G_{\delta} = (1-\delta)I + \delta G \tag{50}$$

where *I* is the identity matrix and G_{δ} is the gradient at the given degree of transformation, δ. δ is a scalar representing the fraction of the drawn state. Therefore $0 \le \delta \le 1$ where the limits are defined as:

$$\delta = \begin{cases} 0 & undrawn\ state\ (\alpha\ state) \\ 1 & fully\ drawn\ state\ (\gamma\ state) \end{cases} \tag{51}$$

When a portion of the material reaches the γ state, the strain remains equal to a constant draw ratio, λ_n, until the entire gauge length has necked. After a complete transition further straining will occur throughout the γ state. This phenomenon is observed during tensile tests of polymers where the necks tend to propagate along the gauge length after formation. Details on the development of constitutive equation can be found in Masud and Chednovsky [29].

BPA Model

Boyce, Parks and Argon [3] proposed a constitutive model for large deformation of glassy amorphous polymers based on the work of Haward and Thackray [30]. They modeled deformation as a three phase system consisting of a linear elastic spring, a nonlinear hardening spring and a viscous dashpot [31]. The three components represent the elastic response, the anisotropic resistance and the isotropic resistance to molecular movement and rotation respectively. The linear elastic portion acts in series with the other two sections paired in parallel (see Figure 2.8).

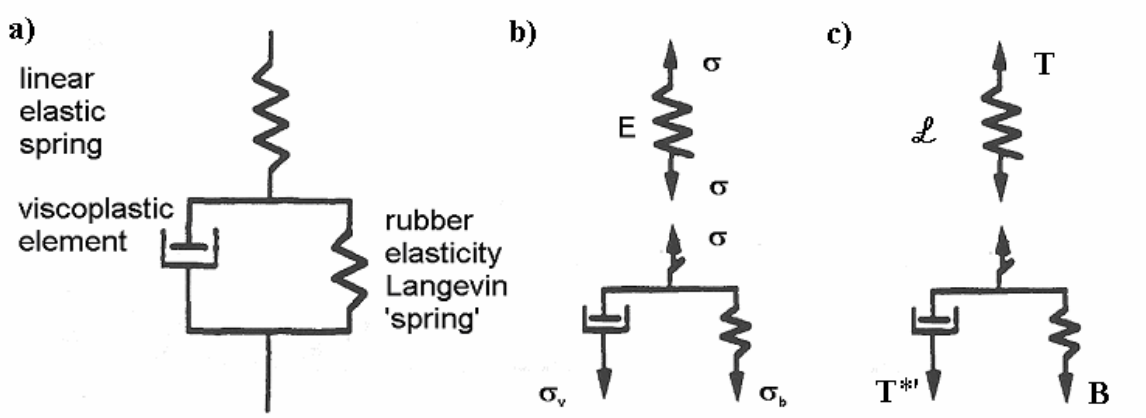

Figure 2.8: Three dimensional representation of the spring and dashpot model of polymer deformation containing an elastic spring in series with a parallel viscous dashpot and nonlinear spring. The governing tensors are labelled in (c). (Reproduced from [31].)

Figure 2.8(c) has been labelled showing tensors acting on each element modeled in figure 2.8(b). The three sections of the model can be broken down individually. The linear elastic spring is characterized by $\mathbb{L}^e$, a fourth order tensor operator:

$$\mathbf{T} = \frac{1}{J}\mathbb{L}^e[\ln \mathbf{U}^e] \tag{52}$$

where $\mathbf{T}$ is the Cauchy stress, $J = \det \mathbf{U}^e$ and $\mathbf{U}^e$ is the Hencky strain [31].

The second piece to be modeled is the viscous dashpot. The strain rate of the dashpot is the plastic shear strain rate, $\dot{\gamma}^P$. It is based on the Arrhenius equation, similar to the Eyring model (see Section 2.2.1):

$$\dot{\gamma}^P = \dot{\gamma}_0 \exp\left[-\frac{E_s}{kT}\left\{1-\left(\frac{\tau}{s}\right)^{5/6}\right\}\right] \tag{53}$$

where $\dot{\gamma}_0$ is a constant proportional to the molecular oscillation frequency, E_s is the zero stress activation energy, k is the Boltzmann constant, T is temperature, τ is the shear stress and s is the athermal shear strength. Equation **(53)** can be rearranged to isolate the shear stress:

$$\tau = s\left[1-\frac{kT}{E_s}\ln\left(\frac{\dot{\gamma}^P}{\dot{\gamma}_0}\right)\right]^{6/5} \tag{54}$$

Strain softening is taken into account by changing the value of s with increasing strain. It is assumed to migrate toward a preferred steady-state, s_{ss}:

$$\dot{s} = h\left(1-\frac{s}{s_{ss}}\right)\dot{\gamma}^P \tag{55}$$

where h is the softening slope. Other factors such as temperature or hydrostatic pressure can also be accounted for by altering s. An aging factor, a, which is a function of the current atmospheric conditions and the current value of s may be added to Eq. **(55)**:

$$\dot{s} = h\left(1-\frac{s}{s_{ss}}\right)\dot{\gamma}^P + a(s,T,p) \tag{56}$$

where p is the hydrostatic pressure [3].

The effective stress on the dashpot element, $\mathbf{T}^*$, is the difference between the total stress, **T**, and the stress subjected to the adjacent spring, **B** (called the backstress). $\mathbf{T}^*$ is responsible for initiating plastic flow.

$$\mathbf{T}^* = \mathbf{T} - \frac{1}{J}\mathbf{F}^e\mathbf{B}\mathbf{F}^{eT} \tag{57}$$

where $\mathbf{F}^e$ is the elastic component of the deformation gradient. **T***', as shown in Figure 2.8, is the deviatoric tensor of **T***.

The final element in the model is the non-linear rubber elasticity Langevin spring. It governs the strain-hardening component of deformation and is characterized by the backstress stress tensor, **B**. The backstress is a function of the internal network geometry and movement. The principal stretches (λ_1, λ_2, λ_3) govern the stretch of any single polymer chain (λ_{chain}) within the material [31].

$$\lambda_{chain} = \frac{1}{\sqrt{3}}\left(\lambda_1^2 + \lambda_2^2 + \lambda_3^2\right)^{1/2} = \frac{1}{\sqrt{3}} I_1^{1/2} \tag{58}$$

where I_1 is the first principal stretch invariant. Relating the stress on the same chain, σ_{chain}, to the stretch, gives:

$$\sigma_{chain} = \lambda_{chain} kT \, \mathrm{L}^{-1}\left\{\frac{\lambda_{chain}}{\sqrt{N}}\right\} \tag{59}$$

where $\sqrt{N}$ is the limiting value of λ_{chain}, $\mathrm{L}^{-1}\{\lambda_{chain}/\sqrt{N}\}$ is the inverse Langevin function and the Langevin function is [31]:

$$\mathrm{L}(\beta) = \coth\beta - \frac{1}{\beta} \quad , \quad \beta = \mathrm{L}^{-1}\left\{\frac{\lambda_{chain}}{\sqrt{N}}\right\} \tag{60}$$

By combining individual chains in Eq. **(59)**, a network response is derived as a function of principal stresses σ_1 and σ_2. Note that σ_3 is omitted due to the redundancy caused by the condition of incompressibility.

$$\sigma_1 - \sigma_2 = \frac{nkT}{3}\sqrt{N} \; \mathrm{L}^{-1}\left\{\frac{\lambda_{chain}}{\sqrt{N}}\right\}\frac{\left(\lambda_1^2 - \lambda_2^2\right)}{\lambda_{chain}} \tag{61}$$

where n is the chain density. The backstress, **B**, is:

$$B_i = \frac{nkT}{3}\sqrt{N} \; \mathrm{L}^{-1}\left\{\frac{\Lambda^P{}_{chain}}{\sqrt{N}}\right\}\frac{\left(\Lambda^P{}_i{}^2 - \frac{1}{3}I_1\right)}{\Lambda^P{}_{chain}} \tag{62}$$

where $I_1 = \left(\Lambda^P{}_1{}^2 + \Lambda^P{}_2{}^2 + \Lambda^P{}_3{}^2\right)$, $\Lambda^P{}_{chain}$ is the plastic stretch on a chain and $\Lambda^P{}_i$ are the principal applied plastic stretches [31].

The BPA model accounts for changes in temperature, strain rate, strain softening and strain-hardening. These four elements largely effect the deformation behavior of the material, allowing this model to be very flexible and account for many testing scenarios.

2.4 Controlling Deformation Behavior

The deformation of polymers, much like metals, is largely a function of the current conditions and thermal/mechanical history of the material. It is generally known that the deformability of polymers is strongly influenced by factors such as temperature, thermal history, pressure, strain rate, molecular weight, free volume and mechanical history. Various approaches to control one or more of these factors have been proposed to enhance formability. Since the interest in this work is to cold form polycarbonate, only methods that are considered feasible in an industrial environment will be described here

2.4.1 Polycarbonate Structure

Polycarbonate (PC) is an amorphous polymer that exhibits very high impact strength and good mechanical properties through a relatively large range of service temperatures. It is an important engineering plastic because of its transparency and relatively high glass transition temperature. The polymer has a wide range of applications including CDs, safety glasses, water bottles, high impact strength glass, and automotive and aircraft parts [32,33]. The chemical structure is shown in Figure 2.9. The T_g for polycarbonate is typically found in the range of 135-160^{o}C. [34]

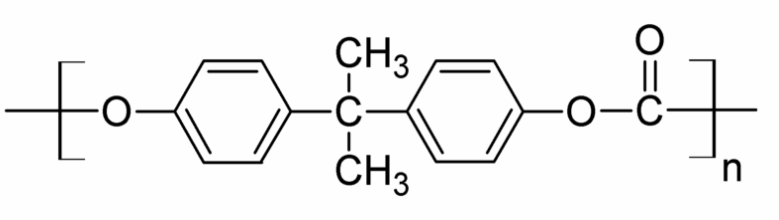

Figure 2.9: Chemical Structure of Polycarbonate. (Reproduced from Ref. [35].)

2.4.2 Thermal Treatments

In general, polymers are largely affected by temperature. Therefore, thermal treatments of polymers can have adverse or beneficial effects on many properties. For example, Figure 1.7 on page 10 shows the extreme effects of temperature on the stress-strain curve of polycarbonate. In this work, however, the aim is to explore deformation behavior at room temperature which is strongly dependent on thermal history.

Glassy amorphous polymers are usually in a metastable state, which is typically far from the thermodynamic equilibrium that they tend to slowly approach. The non-equilibrium state is caused by rapid cooling from above the glass temperature temperature. Many physical properties are directly linked to this metastable state: mechanical and dielectric losses, T_g, creep and relaxation, yield behaviour and toughness. The physical properties depend on the molecular mobility, which in turn depends on the free volume (V_f). Higher free volume can be attained by quenching or fast cooling, thereby "freezing-in" additional free volume before the structure has a chance to reach an equilibrium state, as illustrated in Figure 2.10.

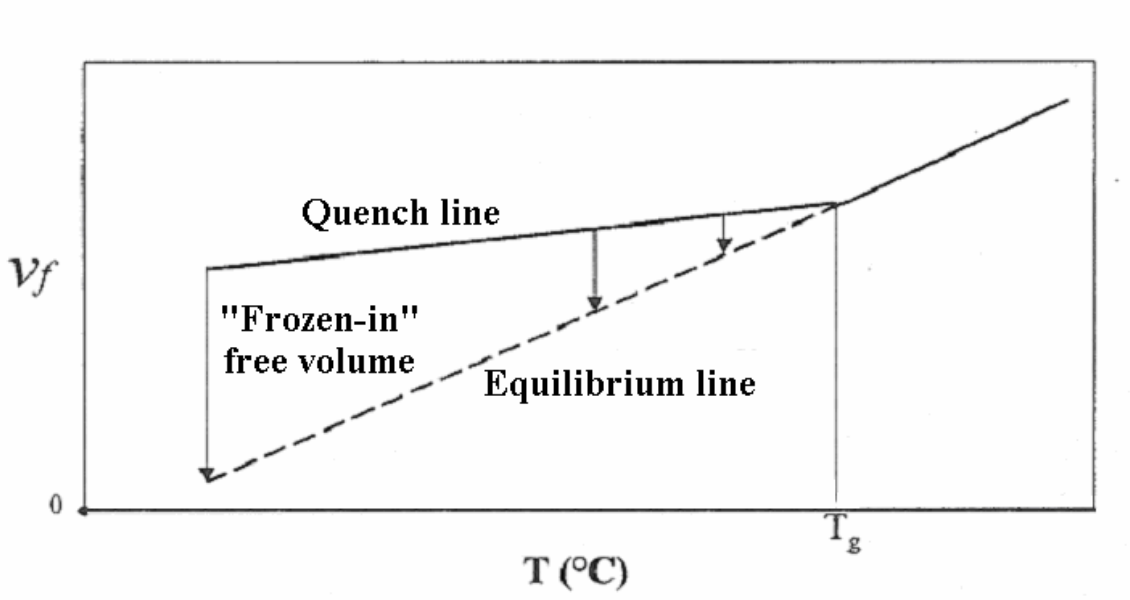

Figure 2.10: Free volume upon fast cooling (quenching) deviates significantly from the thermodynamic equilibrium line obtained through slow cooling. (Reproduced from [36].)

The physical effects of quenching the polymer can be seen in Figure 2.11. Kontou [37] compared the effects of annealing two groups of PC samples above their T_g at 160^{o}C. The samples were either cooled slowly (annealed group) or fast cooled in liquid nitrogen (quenched group) prior to tensile testing. There is a dramatic difference in the yield stress suggesting that increasing free volume also increases the molecular mobility and decreases the resistance to plastic deformation [37].

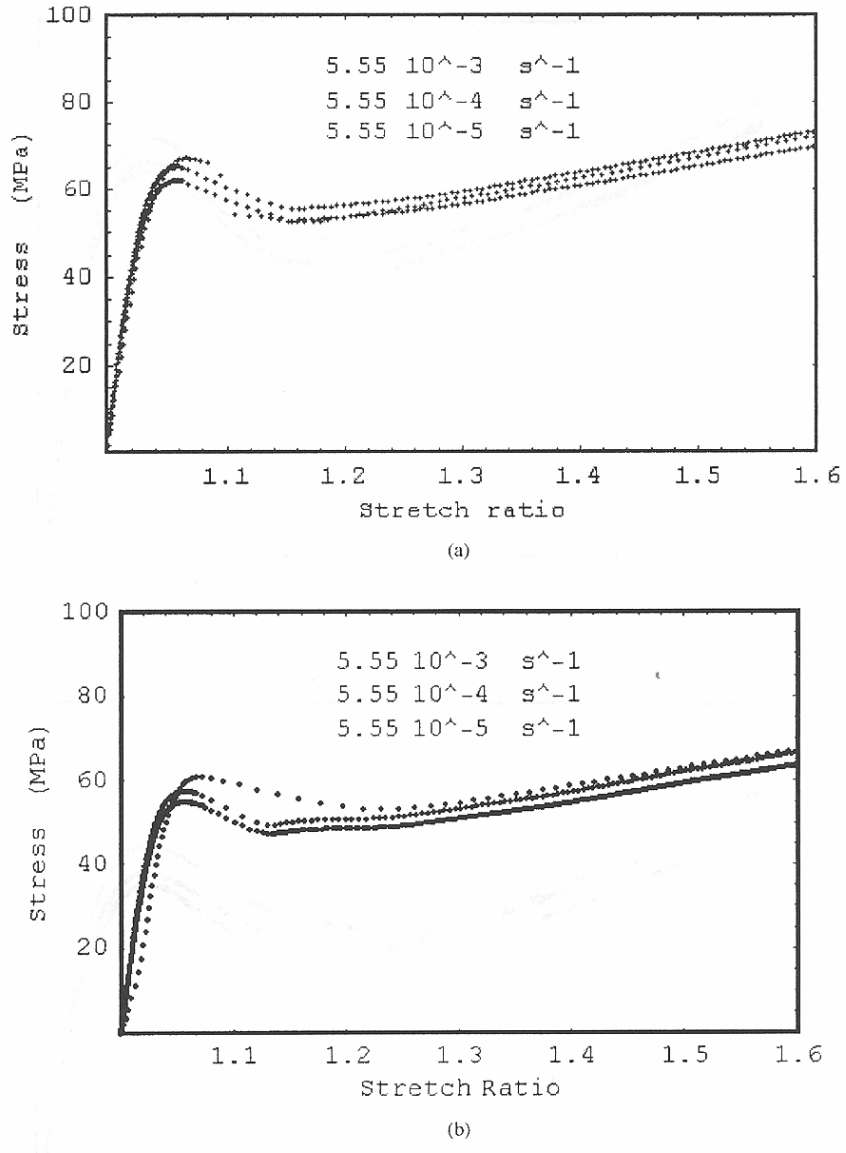

Figure 2.11: Experimental tensile stress/stretch-ratio curves for (a) annealed and (b) quenched PC at three different effective strain rates. (Reproduced from [37].)

2.4.3 Other Factors

Cold rolling

The effect of cold-rolling on the formability of polymers was studied by Lee et al. [13]. It was found that cold rolling the PC decreased the punch head movement to failure, D_p. However, when the punch head movement was normalized with respect to material thickness, the new value, D_p/t, increased with rolling reduction. This led to an overall increase in formability. Table 3 shows the punch head displacement data and Figure 2.12 shows the rolling reduction as a function of punch displacement normalized with thickness.

Table 3: Maximum punch head displacement results for varying degrees of rolling reduction. (Reproduced from [13].)

	D_p (mm)					
Rolling Reduction (%)	0	10	20	30	40	50
Dry	42	38	34	32	28	26
Lubricated	41	33	31	31	29	25

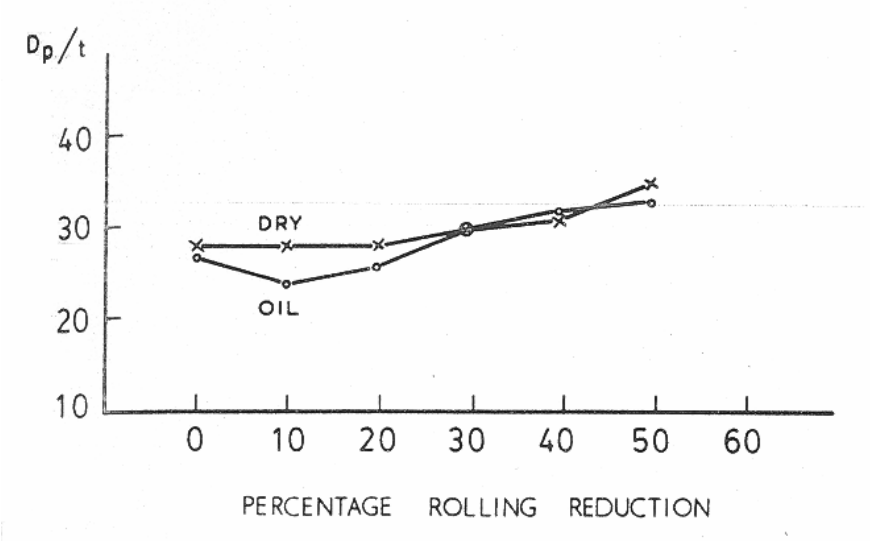

Figure 2.12: Depth of penetration over polycarbonate blank thickness as a function of percentage rolling reduction. (Reproduced from [13].)

Molecular Weight

Many mechanical properties are found to increase with molecular weight. A critical molecular weight, $\overline{M}_c$, exists at the point at which the strength of the primary bonds becomes equal to the stress required to overcome intermolecular forces and chain entanglement [38]. Below $\overline{M}_c$ deformation is primarily a result of slipping motion between chains therefore the mechanical properties are highly dependant on the molecular weight. However, above $\overline{M}_c$ slip between chains no longer occurs and plastic deformation occurs due to primary bonds being broken. In this range the mechanical properties are much less dependant on molecular weight. Figure 2.13 shows the yield strength, strain and elastic modulus as functions of molecular weight for polycarbonate. The critical molecular weight would be in the range of 11000-13000 g/mol in this particular case. Large variances in parameters occur below $\overline{M}_c$, but above $\overline{M}_c$ they are far less sensitive to changes in molecular weight.

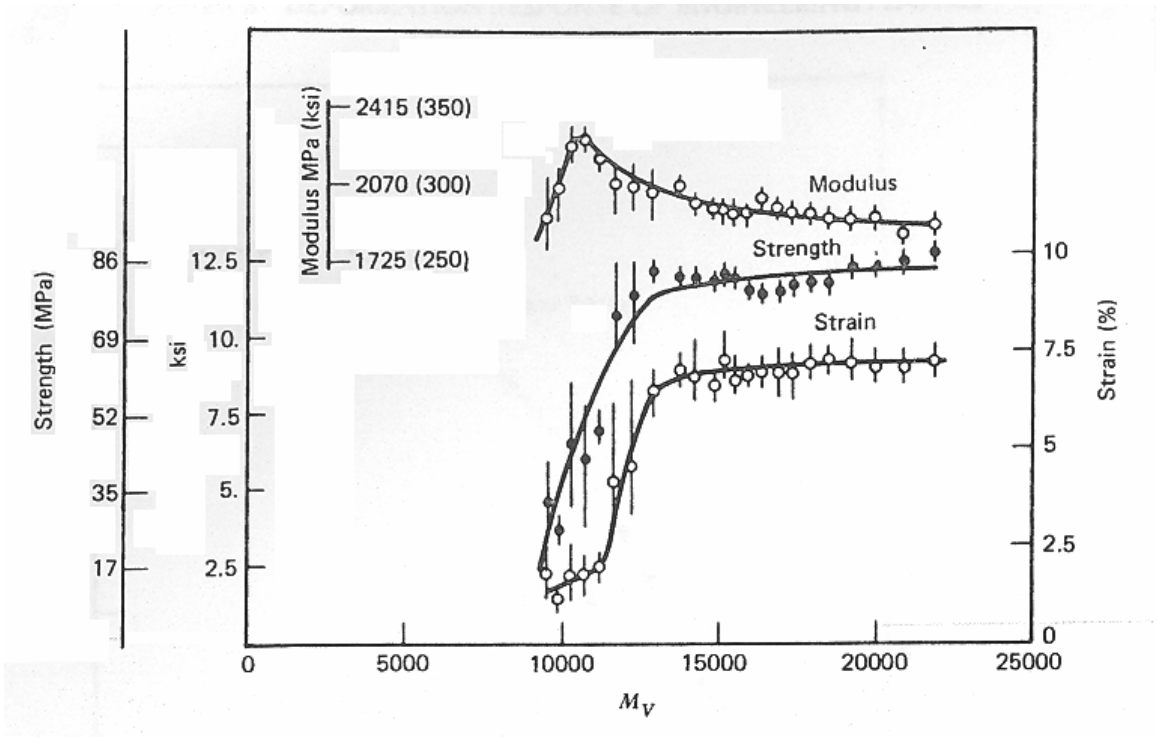

Figure 2.13: Mechanical properties in polycarbonate as a function of viscometric molecular weight (M_v). (Reproduced from Ref. [38].)

There are many ways to define molecular weight. $\overline{M}_n$ is called the number average molecular weight. $\overline{M}_w$ is called the weight average molecular weight. $\overline{M}_w$ is more sensitive to higher individual molecular masses, meaning that a polymer with a given $\overline{M}_n$ and high variance in individual molecular weights will have a higher $\overline{M}_w$ than one with the same $\overline{M}_n$ and a small variance. Both are used in various applications depending on what property is being characterized. However, with mechanical properties such as those found in Figure 2.13 it is not clear which average correlates best [38]. In this investigation, $\overline{M}_w$ was examined.

2.4.4 Conditions for Higher Formability

Generally, the maximum formability can theoretically be attained when the yield stress is minimized and the elongation to failure is maximized. Factors to achieve this include:

- increasing forming temperature
- increasing hydrostatic pressure
- increase free volume (decrease activation volume)
- optimize polymer molecular weight (typically by decreasing)
- favourable thermal history (such as quenching)
- favourable mechanical history (such as cold-rolling)

This work will focus on the effects of molecular weight.

3 Experimental Details

3.1 Materials

Three different polycarbonate sheets were used in this study. All of them are commercially known as Lexan®. The first is a sheet supplied by SABIC Innovative Plastics (formerly GE Advanced Materials) in Cobourg, Ontario. This is referred to as group "42-T1". The other two sheet materials which have higher molecular weights were purchased off the shelf. Groups 42-T1 and 52-T1 had a sheet thickness of 1/16" (1.59 mm) while 52-T2 had a sheet thickness of 1/8" (3.18 mm).

Table 4: Material properties for different batches used in this study. Molecular weight values are relative to polystyrene standards.

	Thickness	$\overline{M}_n$ (g/mol)	$\overline{M}_w$ (g/mol)	Product Number	Source
42-T1	1.59 mm	9,300	42,400	N/A	Supplier
52-T1	1.59 mm	24,400	51,600	Lexan* 9030	Commercial
52-T2	3.18 mm	24,500	52,300	Lexan* 9030	Commercial

Material data sheets for Lexan* 9030 can be found in Appendix A. Molecular weight data obtained through gel permeation chromatography (GPC) studies are attached in Appendix B.

3.2 Characterization Tests

Two different types of tests were performed to characterize the polycarbonate sheets. In the first, differential scanning calorimetry tests were conducted to determine the glass transition temperature. The second consisted of tensile tests using dog-bone shaped samples to determine stress-strain behaviour and anisotropy.

3.2.1 Differential Scanning Calorimetry

A TA Instruments' Differential Scanning Calorimeter (DSC) 2050 was used to characterize the glass transition range. Samples weighing 11 ± 2 mg were sealed in aluminum hermetic pans prior to testing. Each sample was first equilibrated at 30^{o}C and then heated at a rate of 10^{o}C/min up to 180^{o}C. The sample was held at this temperature for 5 minutes in order to erase the thermal history [39,40]. A second heating was done at 10^{o}C/min after cooling back to 30^{o}C. The second curve was used to find the glass transition temperature (T_g) as well as the change in enthalpy (Δh) that occurs during the glass transition. The second heating curve was preferred over the first as it better quantifies the enthalpic properties of the material itself, rather than the effects of thermal history. In a typical DSC curve Figure 3.1, an endothermic peak is usually very distinct upon heating past phase transition. In this case, the glass transition temperature, T_g, is about 152^{o}C.

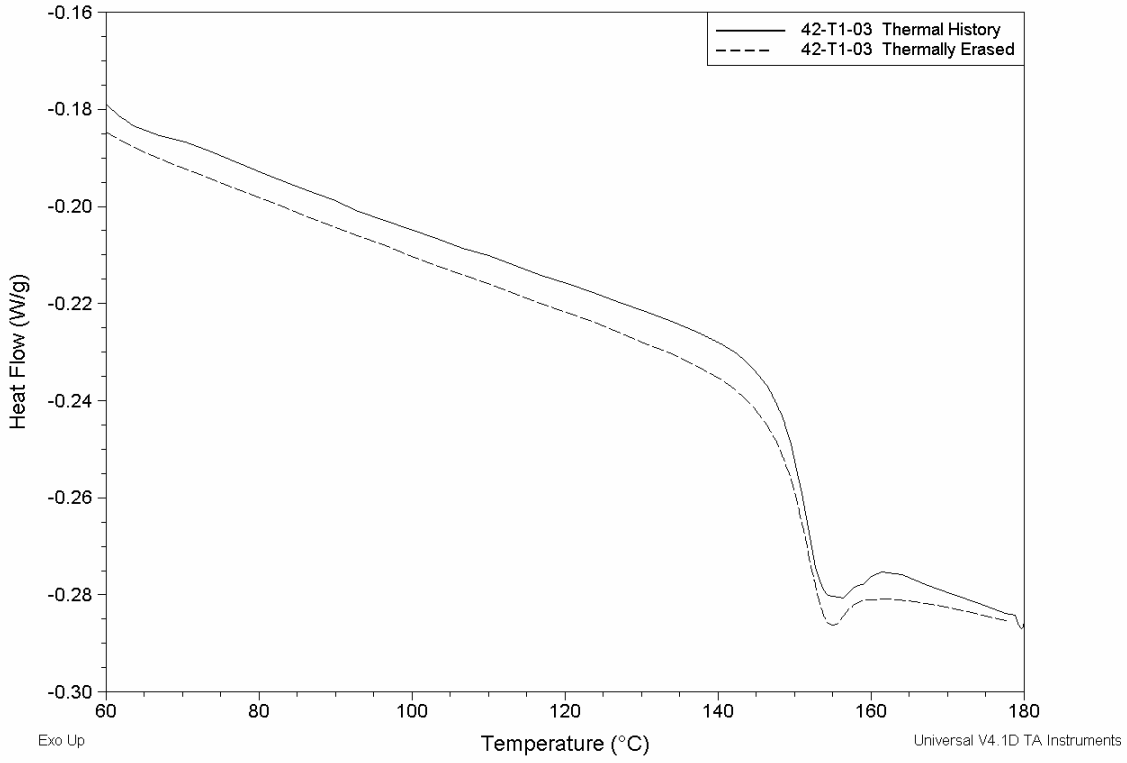

Figure 3.1: Typical DSC scan for a 42-T1 sample.

The TA Universal Analysis® software was used to find the glass transition temperature of each sample. The enthalpy change, Δh, that occurs upon heating past the glass transition can be measured by taking the area under the endothermic peak. Figure 3.2 shows how the values of Δh and T_g were determined.. Four samples of each material were tested. The scans for all the specimens provided in Appendix C.

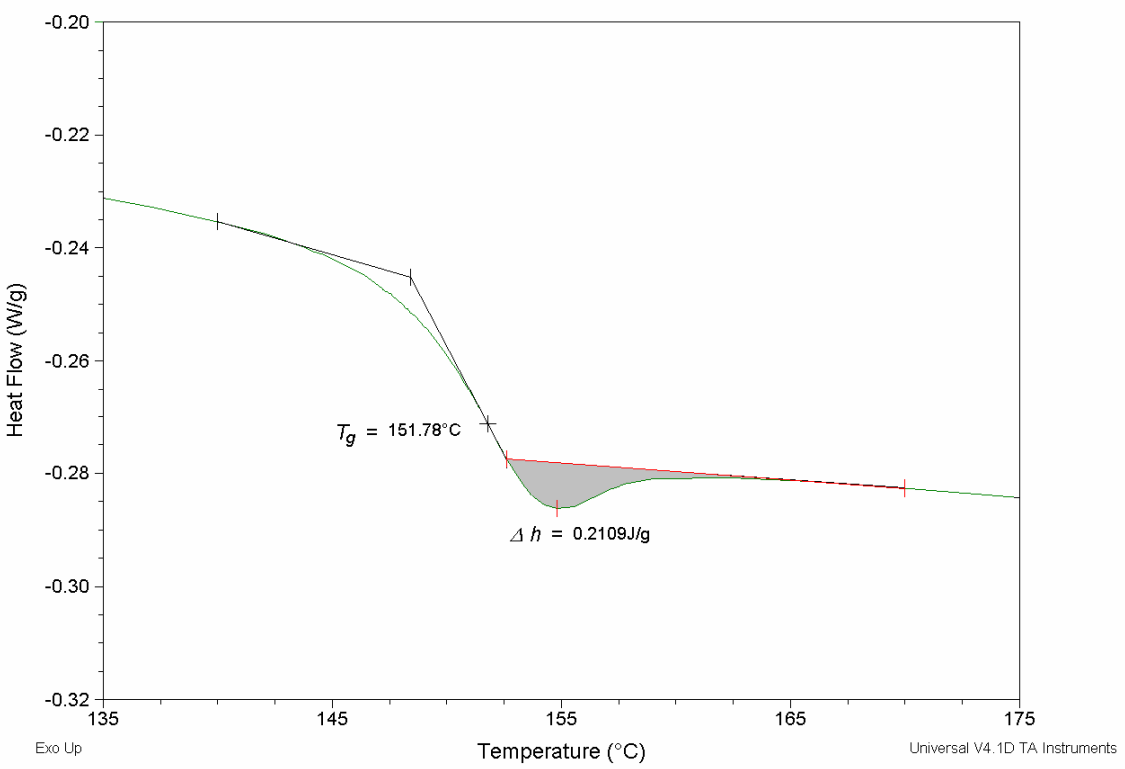

Figure 3.2: Glass transition temperature and change in enthalpy for a 42-T1 sample.

According to Petrie, the change in enthalpy that occurs during the glass transition can be used to compare the distribution of free volume in a polymer [41]. Qualitatively, a larger and broader endothermic peak at the glass transition can be interpreted a larger amount of free volume present in the polymer for the same heating conditions.

3.2.2 Tensile Testing

Specimens were machined into dog-bone shapes in accordance to Type I specifications of the ASTM D638-03 [42] (shown in Figure 3.3) using a water jet cutter.

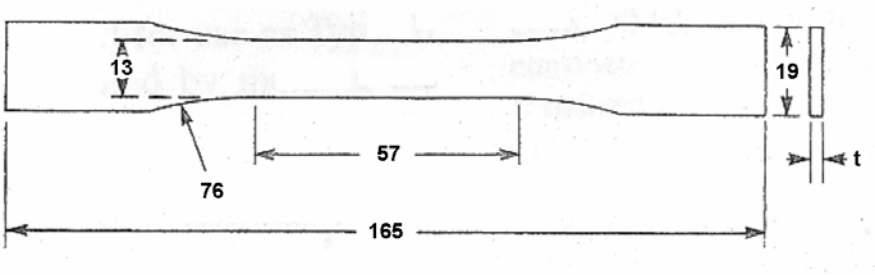

Figure 3.3: Dimensions of ASTM D638-03 Type I tensile coupons. All dimensions in mm. (Reproduced from Ref. [42].)

Tensile tests were performed on an Instron Model 1331 servo-hydraulic testing machine using a 25 kN load cell. An Instron Dynamic Extensometer Model 2620-601 with gauge length 50 mm was used to record the strain. Tensile tests were performed at three different cross-head speeds: 2 mm/min, 20 mm/min and 200 mm/min. Three specimens from each group were tested at each speed. The strain was recorded up to 10% with the extensometer, after which the extensometer was removed and tests were resumed. Figure 3.4 shows a load-displacement curve and corresponding engineering stress-strain curve for a typical specimen. Notice the stress-strain curve does not exceed 10% strain. Also, the load displacement curve has a significant drop in stress at a cross-head displacement of approximately 8.5 mm. This is the point at which testing momentarily stopped while the extensometer was removed before continuing the test. The drop in stress was due to stress relaxation occurring while the sample was stationary. Upon resuming, the load returned to the same level prior to the test interruption. This drop in stress/load is present in all tensile tests performed that exceeded 10% strain. It is also important to note that for nearly all tensile specimens, the neck that formed did not occur within the limits of the extensometer. Often it occurred outside or on the end of the extensometer, causing all strain data beyond the onset of necking to become inaccurate.

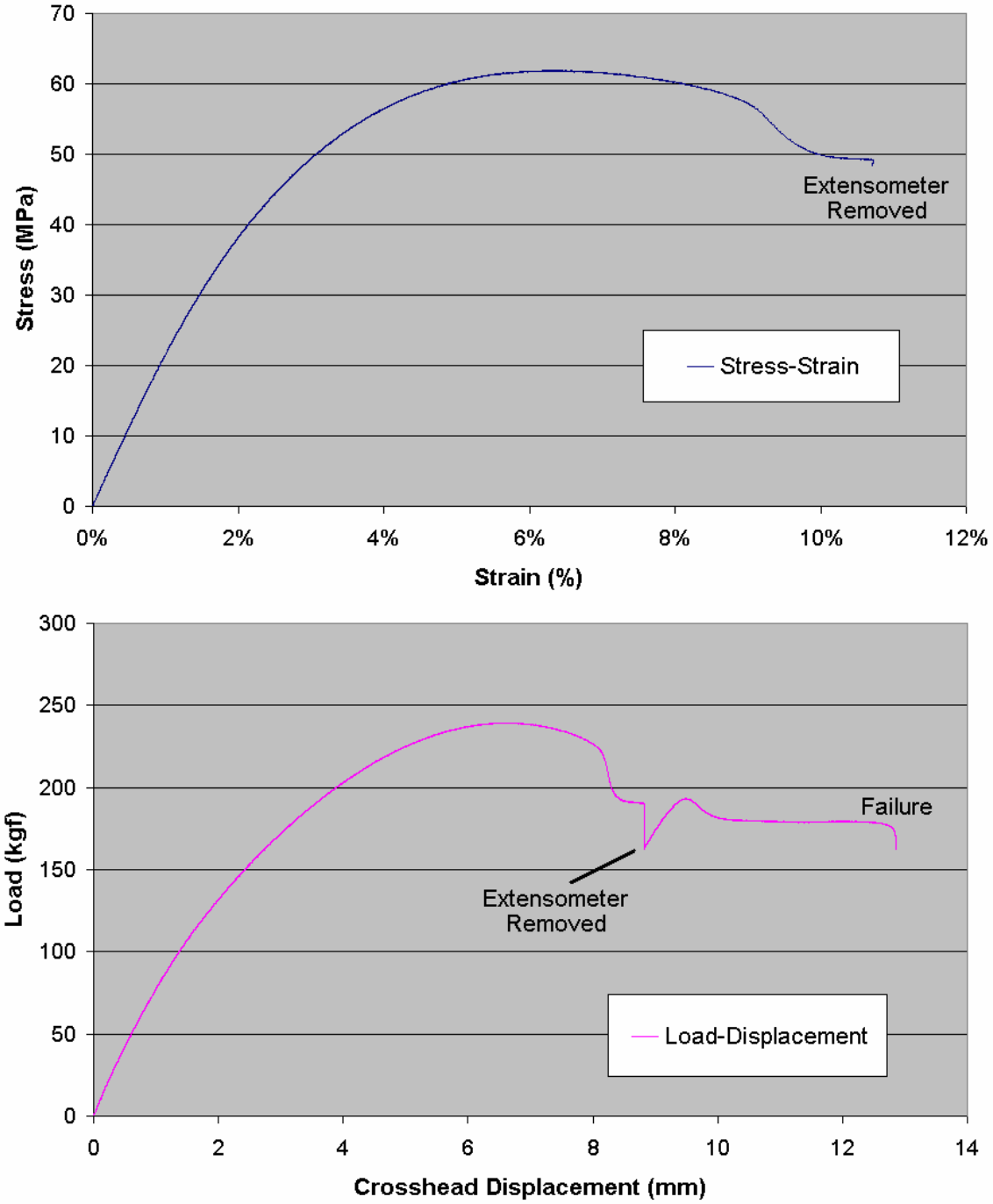

Figure 3.4: Typical stress-strain curve (above) and load-displacement curve (below) for a 52-T2 specimen tested at 20 mm/min.

The yield stress was calculated based on a 0.2% offset method. For each sample, the slope of the engineering stress-strain curve was calculated based on strains below 1% (where the curve is linear). A line was then drawn offset 0.2% strain from the origin and a having a slope equal to the calculated modulus of elasticity. The point where the engineering curve intersected this 0.2% offset line was the yield point.

ANOVA

The analysis of variance (ANOVA) is a statistical analysis technique used to compare data based on fixed effects [43]. It incorporates the variance in the data to generate a confidence interval or percent chance that a given effect plays a significant role. An effect was said to be "statistically significant" if the probability that it was significant exceeded 90%. In this study, the effects of material type (42-T1, 52-T1, 52-T2) and cross-head speed (2, 20, 200 mm/min.) were analyzed.

Anisotropy

To study sheet anisotropy, samples were cut along and transverse to the rolling directions from material group 42-T1 only. The samples cut parallel to the rolling direction were called "horizontal" and samples are denoted with an "H", while those cut perpendicular were called "vertical" and are denoted with a "V". Preliminary test results (seen in Table 5) were analyzed using statistical analysis of variance techniques. The effect of direction had no statistically significant effects on any of the parameters listed. There was statistical significance found in the effect of strain rate, however this is discussed in Section 4.2.

Table 5: Summary of data to evaluate anisotropy.

Sample Name	Relative Orientation (deg.)	X-Head Speed (mm/min)	Max Stress (MPa)	Yield Stress (MPa)	X-Head Disp. @ Failure (mm)	Modulus of Elasticity (MPa)	Anisotropy Ratio
H04	0	2	59.42	34.83	8.72	2165	0.520
H06-1	0	2	59.20	34.96	7.87	2201	N/A
H07	0	2	59.08	35.21	8.77	2184	0.518
H09	0	20	61.97	36.03	7.75	2273	N/A
H10	0	20	61.83	36.46	8.02	2214	N/A
H11	0	20	61.24	36.30	9.95	2172	0.469
H12	0	200	64.75	38.32	9.67	2206	0.512
H13	0	200	64.63	37.90	8.25	2254	N/A
H14	0	200	64.61	37.06	7.88	2267	N/A
Averages	0	2	59.23	35.00	8.46	2183	0.519
	0	20	61.68	36.26	8.57	2219	0.469
	0	200	64.66	37.76	8.60	2242	0.512
	0	all	61.86	36.34	8.54	2215	0.505
Standard	0	2	0.3%	0.5%	6.0%	0.8%	0.3%
Deviation	0	20	0.6%	0.6%	14.0%	2.3%	-----
(%)	0	200	0.1%	1.7%	11.0%	1.4%	-----
	0	all	3.8%	3.4%	9.5%	1.8%	4.8%
V01-1	90	2	58.65	36.00	8.95	2178	0.502
V02	90	2	58.84	35.04	13.21	2173	0.515
V05	90	2	58.91	35.47	12.58	2189	0.515
V08	90	20	61.13	36.69	11.06	2239	0.481
V09-1	90	20	61.30	36.54	10.58	2190	0.515
V06-1	90	20	61.19	36.60	8.15	2220	N/A
V10-3	90	200	64.63	38.08	8.09	2236	N/A
V11	90	200	63.66	37.17	9.92	2231	0.487
V12	90	200	64.01	37.06	7.86	2223	N/A
Averages	90	2	58.80	35.50	11.58	2180	0.511
	90	20	61.21	36.61	9.93	2216	0.498
	90	200	64.10	37.44	8.62	2230	0.487
	90	all	61.37	36.52	10.04	2209	0.502
Standard	0	2	0.2%	1.4%	19.9%	0.4%	1.4%
Deviation	0	20	0.1%	0.2%	15.7%	1.1%	4.9%
(%)	0	200	0.8%	1.5%	13.1%	0.3%	-----
	0	all	3.8%	2.5%	19.7%	1.2%	3.1%

There were difficulties in measuring the anisotropy ratio accurately. Based on Eq. **(14)**, the anisotropy ratio was calculated by measuring the material thickness and width before

the tests and then measuring again at the region of failure afterwards. In many cases the neck that formed near fracture did not have a uniform cross-section where the final width and thickness could be easily measured. In these cases the anisotropy ratio could not be calculated and the values were left absent (marked "N/A") from Table 5. Figure 3.5 shows a complete neck where the anisotropy ratio was easily measured and an incomplete neck where there was no point at which the cross-section could be accurately measured. The different types of necking arise due to different deformation modes that take place within the polymer. Initially, the specimen undergoes shear yielding, which occurs at an angle. The neck then propagates into neighbouring regions where it begins to undergo uniform neck growth. If the failure took place during shear yielding, the failure would contain an incomplete neck. Note that the samples used (16^{th}_25 and 16^{th}_53) had identical test conditions, so the formation of the different neck types is random. However, it was observed that only the thinner samples (groups 42-T1 and 52-T1) resulted in non-uniform necking and variation in failure modes.

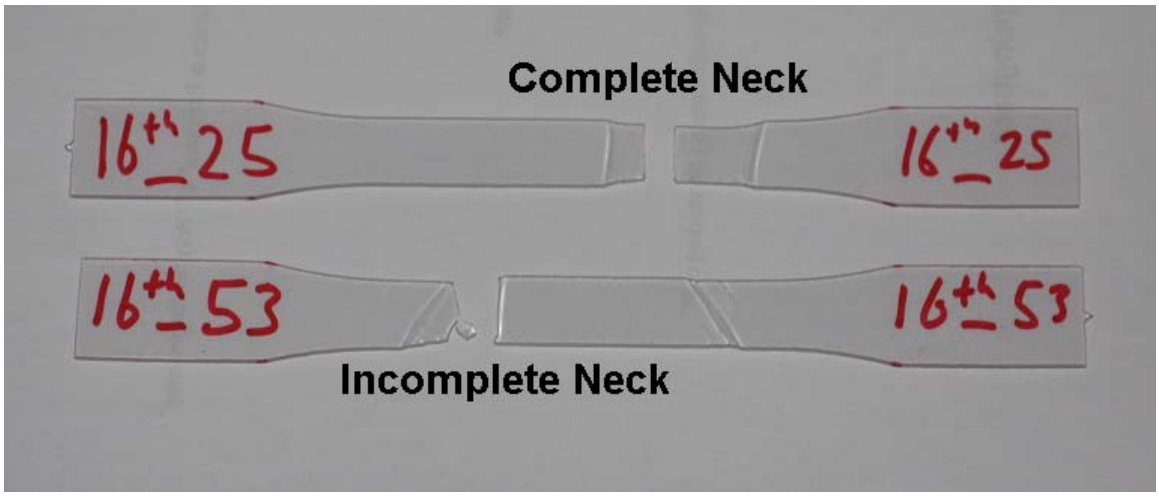

Figure 3.5: Complete and incomplete necks for two samples from a set of 52-T1 samples tested at 20 mm/min to failure.

For the remainder of the study, only one set of data from group 42-T1 was used in order simplify things (V series of tests shown in Table 5 is omitted). Tests for groups 52-T1 and 52-T2 were also completed. Due to the lack of directional effects found in group 42-T1, it was assumed that only one direction would need to be tested for the other groups.

3.3 Dome Stretch Forming

The dome stretch forming tests were performed on an MTS Metal Form machine. The basic apparatus consisted of two parts: a blank holder clamp and a movable hemispherical punch with a diameter of 101.6 mm (4”). During the tests, a clamping force of 44,480 N (10,000 lb) was used to eliminate any drawing effects. For these tests, the thin protective film of polyethylene that comes on the surface of the polycarbonate was used as a lubricant between the punch head and the polycarbonate. A punch head speed of 152.4 mm/min (0.1 in./s) was used during all tests. Figure 3.6 shows a diagram of the forming machine, the clamp and punch head.

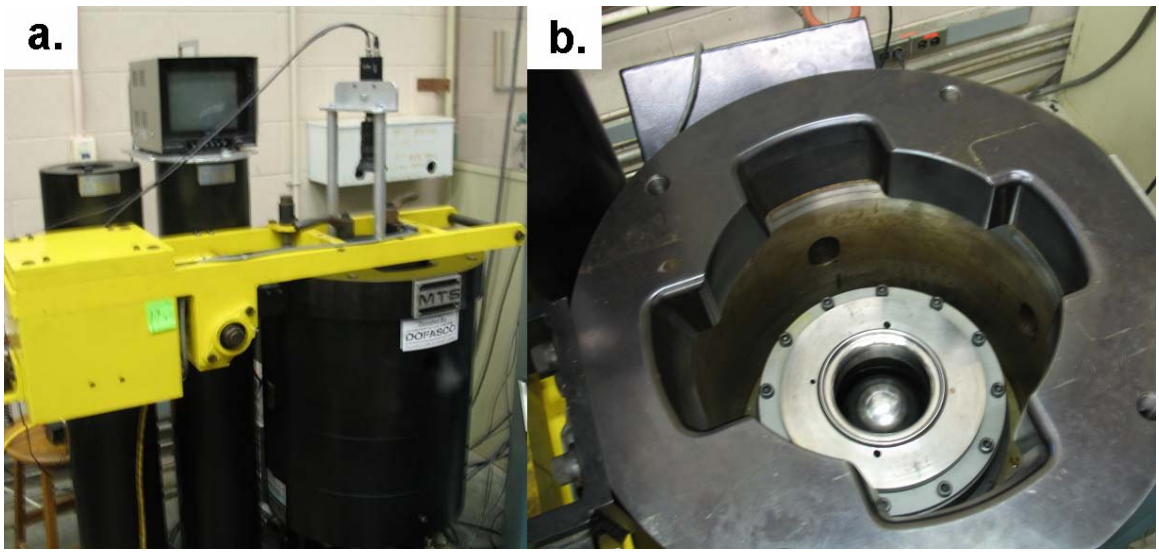

Figure 3.6: a.) Dome testing machine. b.) Clamp and punch head view of dome testing machine.

Two basic sample shapes were used during the forming tests. The first type were cut into rectangles of similar length (~8" or 20.3 mm) and varying widths. The widths used for the tests were 1" (25.4 mm), 2" (50.8 mm), 3" (76.2 mm), 4" (101.6 mm), 5" (127 mm) and 7" (177.8 mm). A second type of specimen was also used because the failure zones of the rectangular specimens were often found in hard to measure areas near the clamping zone. These specimens were dog-bone shaped with dimensions as shown in Figure 3.7.

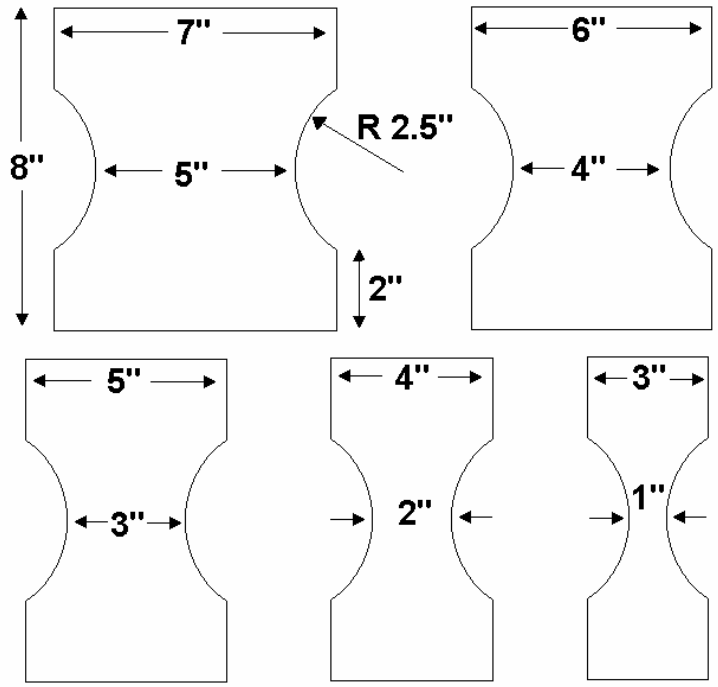

Figure 3.7: Dog-bone forming specimens used in forming tests with dimensions. (Not to scale.)

Three rectangular specimens of each width were tested for each group. Two of those three were tested to failure and the other was tested to a dome height past the yield point, but before failure occurred. Only two of each width for the dog bone shaped specimens were tested, both to failure. This is a total of 28 specimens per group (84 total).

All forming specimens were printed with a grid pattern of small 2.5 mm diameter circles superimposed onto square grids which were 6 mm wide, in accordance to ASTM Standard 2218-02 [14]. A close up of the grid pattern is shown in the far right hand frame in Figure 3.8.

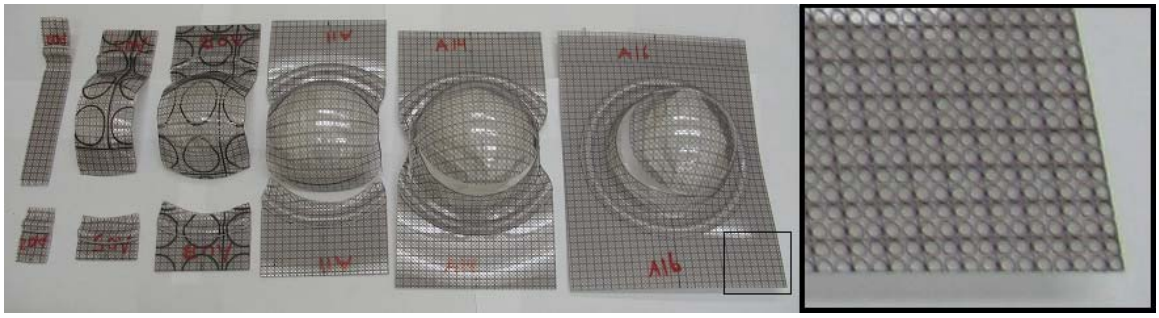

Figure 3.8: Formed rectangular specimens (left) and a zoomed-in view of the printed grid (right).

The grid pattern printed on the surface of the specimens was used to measure localized strain. A MS112 camera fitted with LED lights was used to take close up images of the grid pattern. An image analysis program measured the strain of individual circles before and after forming within the grid pattern. This was done on the computer by marking an electronic image with a series of five points along the edge of the deformed circle, which defined an ellipse. The image analysis software automatically compares the elliptical shape with images of the undeformed original circles, or the reference template. The new elliptical shapes are defined as the deformed states with the major and minor strain being the corresponding differences in dimensions. Figure 3.9 shows the typical undeformed grid pattern (part a) and the deformed grid pattern in the necked region (part b).

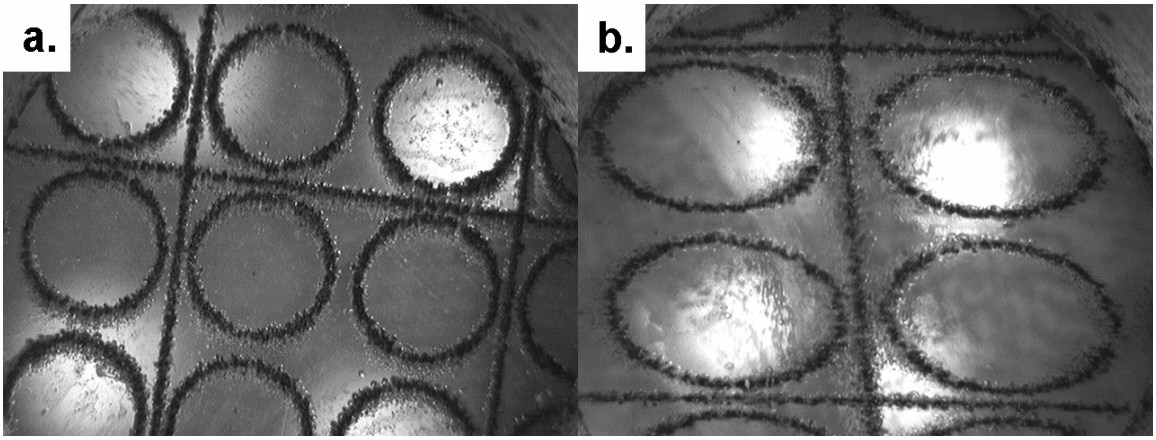

Figure 3.9: a.) Undeformed grid pattern. b.) Deformed grid pattern of a necked area.

Approximately seven or eight measurements were taken from each of the 28 forming specimens tested in each group (~600 total). They were plotted into three different forming limit diagrams in Section 4.3.

4 Results and Discussion

4.1 DSC

Using the method described in Section 3.2.1 to analyze the DSC scans as shown in Figure 3.12, the T_g and area under the endothermic peak (Δh) for the three polycarbonates are provided in Table 6.

Table 6: Glass transition data for each polycarbonate group.

	Glass Transition Data	
	T_g (^{o}C)	Δh (J/g)
42-T1-01	152.6	0.2182
42-T1-02	152.5	0.2353
42-T1-03	151.8	0.2109
42-T1-04	152.4	0.1896
Average	152.3	0.2135
St. Dev. (%)	0.25%	8.9%
52-T1-01	151.2	0.2411
52-T1-02	151.4	0.2588
52-T1-03	152.1	0.1824
52-T1-04	152.4	0.1536
Average	151.8	0.2090
St. Dev. (%)	0.38%	23.6%
52-T2-01	152.0	0.2332
52-T2-02	152.9	0.1986
52-T2-03	152.2	0.2164
52-T2-04	151.3	0.1529
Average	152.1	0.2003
St. Dev. (%)	0.44%	17.3%

It is clear that although the relatively large difference in weights of 42-T1 ($\overline{M}_w$ = ~42,000) and 52-T1 and 52-T2 ($\overline{M}_w$ = ~52,000), there is almost no difference in glass transition temperatures for the two materials. The error within individual tests is extremely small as well, showing a high degree of consistency in the polymer samples.

Free Volume Comparison

If the area under the endothermic peak, Δh, is used to qualitatively compare the level of free volume in the material, as described in Section 3.2.1. there does not appear to be a clear relationship between molecular weight and the endothermic peak size. As shown in Figure 4.1 there is quite a variation in the enthalpic change; the higher molecular weight materials seem to have slightly more variation in free volume size and distribution than the 42-T1 material

Generally, based on DSC test results alone, there is negligible difference in the glass transition and free volume characteristics of the two molecular weights studied.

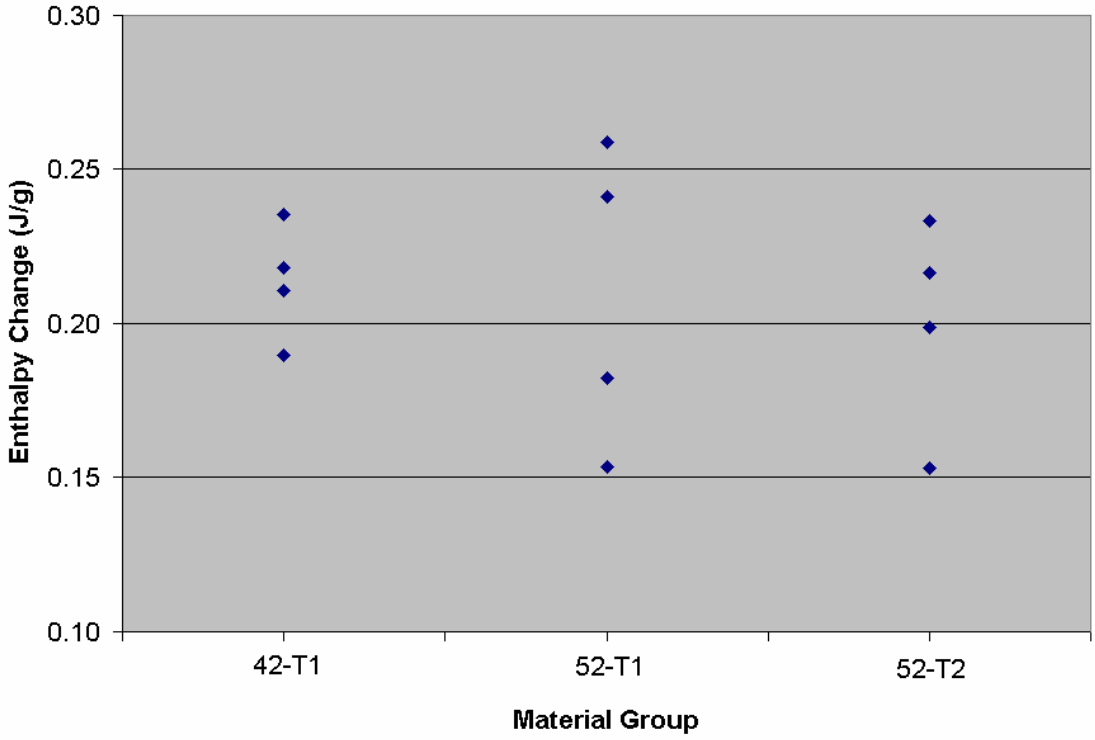

Figure 4.1: Enthalpy change for each material group.

4.2 Tensile Tests

Figure 4.2 shows typical load-displacement curves determined from tensile testing three samples from group 42-T1 at 200 mm/min. Corresponding stress-strain curves for the same three specimens are shown in Figure 4.3. The elastic and yield regions are very repeatable, but post-yield behaviour varies considerably. Again, the stress-strain curves are not accurate beyond the onset of necking (see Section 3.2.2). Additional load-displacement and stress-strain curves for other materials and testing rates can be found in Appendix D and Appendix E respectively.

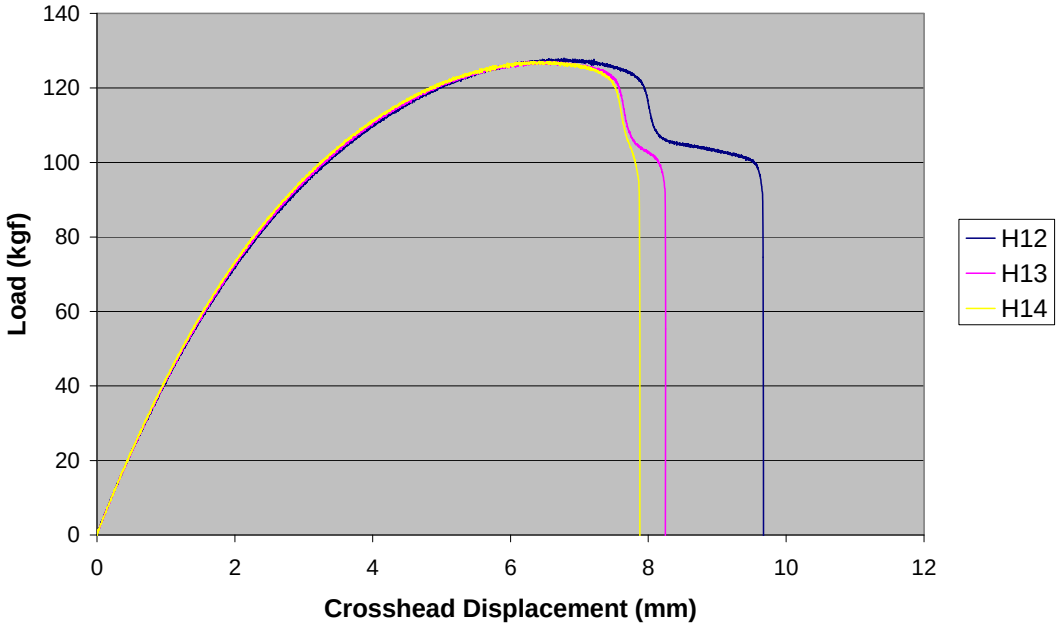

Figure 4.2: Load-displacement curve for group 42-T1 samples tested at 200 mm/min.

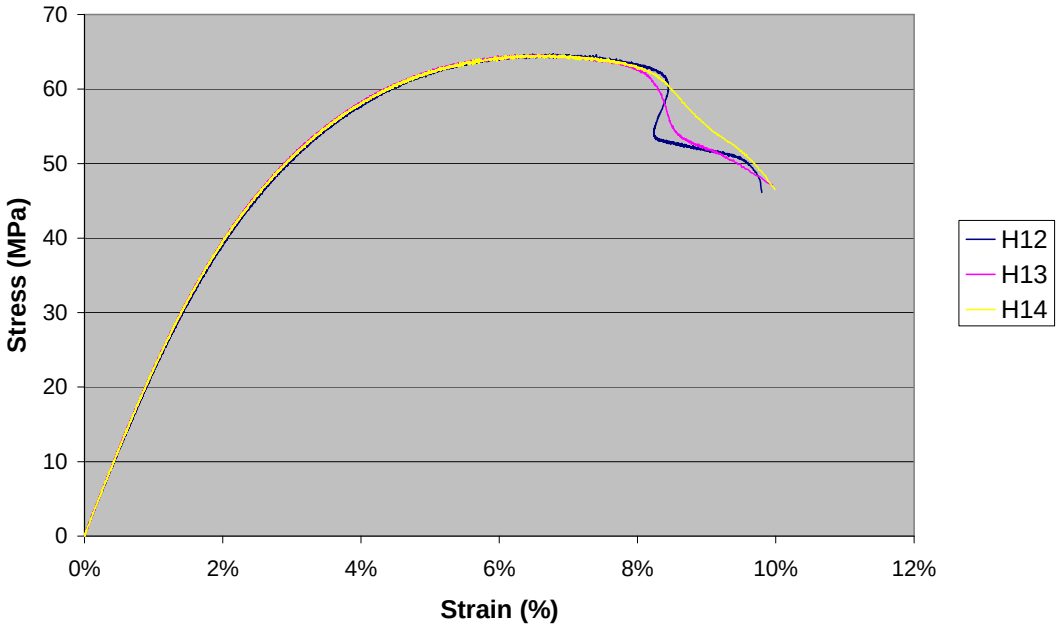

Figure 4.3: Stress-strain curve for group 42-T1 samples tested at 200 mm/min.

All tensile test data for material groups 42-T1, 52-T1 and 52-T2 are listed in Table 7, Table 8 and Table 9 respectively. Statistically significant results based on ANOVA criteria (see Section 3.2.2) are summarized in Table 10.

Table 7: Tensile data for material group 42-T1.

	Sample Name	X-Head Speed (mm/min)	Material Thickness (mm)	Max Stress (MPa)	Yield Stress (MPa)	Strain @ Yield Point	X-Head Disp. @ Failure (mm)	Modulus of Elasticity (MPa)	Anisotropy Ratio
42-T1	H04	2	1.51	59.4	34.8	0.0181	8.72	2165	0.52
	H06-1	2	1.48	59.2	35.0	0.0179	7.87	2201	N/A
	H07	2	1.48	59.1	35.2	0.0181	8.77	2184	0.52
	H09	20	1.48	62.0	36.0	0.0179	7.75	2273	N/A
	H10	20	1.48	61.8	36.5	0.0185	8.02	2214	N/A
	H11	20	1.49	61.2	36.3	0.0187	9.95	2172	0.47
	H12	200	1.49	64.8	38.3	0.0194	9.67	2206	0.51
	H13	200	1.47	64.6	37.9	0.0188	8.25	2254	N/A
	H14	200	1.48	64.6	37.1	0.0183	7.88	2267	N/A
	Averages	2	1.49	59.2	35.0	0.0180	8.46	2183	0.52
		20	1.48	61.7	36.3	0.0183	8.57	2219	0.47
		200	1.48	64.7	37.8	0.0188	8.60	2242	0.51
		all	1.48	61.9	36.3	0.0184	8.54	2215	0.50
	Standard Deviation (%)	2	1.2%	0.3%	0.5%	0.6%	6.0%	0.8%	0.3%
		20	0.3%	0.6%	0.6%	2.4%	14.0%	2.3%	N/A
		200	0.5%	0.1%	1.7%	2.7%	11.0%	1.4%	N/A
		all	0.7%	3.8%	3.4%	2.7%	9.5%	1.8%	4.8%

Table 8: Tensile data for material group 52-T1.

	Sample Name	X-Head Speed (mm/min)	Material Thickness (mm)	Max Stress (MPa)	Yield Stress (MPa)	Strain @ Yield Point	X-Head Disp. @ Failure (mm)	Modulus of Elasticity (MPa)	Anisotropy Ratio
52-T1	16th_29	2	1.51	58.8	36.3	0.0184	8.96	2210	0.41
	16th_16	2	1.52	59.4	36.2	0.0183	12.99	2229	0.49
	16th_53-1	2	1.51	59.1	36.6	0.0184	8.64	2233	N/A
	16th_35-1	20	1.54	61.7	37.7	0.0189	13.16	2228	N/A
	16th_25	20	1.51	61.5	37.6	0.0187	13.17	2259	0.46
	16th_22	20	1.54	61.5	36.8	0.0182	7.47	2267	N/A
	16th_22	200	1.53	64.6	38.0	0.0186	7.72	2283	0.42
	16th_13	200	1.52	64.7	38.3	0.0188	7.44	2277	N/A
	16th_43	200	1.53	64.7	38.1	0.0189	7.90	2261	N/A
	Averages	2	1.51	59.1	36.4	0.0184	10.20	2224	0.45
		20	1.53	61.5	37.4	0.0186	11.27	2251	0.46
		200	1.53	64.6	38.1	0.0188	7.69	2274	0.42
		all	1.52	61.8	37.3	0.0186	9.72	2250	0.45
	Standard Deviation (%)	2	0.4%	0.5%	0.6%	0.5%	23.8%	0.6%	11.8%
		20	1.2%	0.2%	1.3%	1.9%	29.2%	0.9%	N/A
		200	0.3%	0.1%	0.4%	0.7%	3.0%	0.5%	N/A
		all	0.8%	3.9%	2.2%	1.4%	26.7%	1.1%	7.9%

Table 9: Tensile data for material group 52-T2.

	Sample Name	X-Head Speed (mm/min)	Material Thickness (mm)	Max Stress (MPa)	Yield Stress (MPa)	Strain @ Yield Point	X-Head Disp. @ Failure (mm)	Modulus of Elasticity (MPa)	Anisotropy Ratio
52-T2	8th_15-1	2	2.99	59.2	36.1	0.0185	8.30	2183	0.45
	8th_09	2	2.99	59.1	35.0	0.0185	17.95	2117	0.61
	8th_51-1	2	3.02	58.9	35.3	0.0184	8.96	2152	0.53
	8th_16	20	2.99	62.1	37.2	0.0190	8.18	2193	0.47
	8th_20-1	20	2.97	62.1	37.0	0.0190	12.65	2179	0.53
	8th_26	20	2.96	61.9	36.8	0.0191	12.86	2160	0.64
	8th_04-1	200	3.01	65.2	38.0	0.0194	9.59	2190	0.50
	8th_54-1	200	3.02	64.8	37.8	0.0193	10.31	2184	0.58
	8th_48-1	200	3.02	65.1	37.7	0.0192	11.43	2193	0.45
	Averages	2	3.00	59.1	35.5	0.0185	11.74	2151	0.53
		20	2.98	62.0	37.0	0.0190	11.23	2177	0.55
		200	3.01	65.1	37.8	0.0193	10.44	2189	0.51
		all	3.00	62.1	36.8	0.0189	11.14	2172	0.53
	Standard Deviation (%)	2	0.5%	0.2%	1.7%	0.5%	45.9%	1.5%	15.3%
		20	0.4%	0.2%	0.5%	0.3%	23.5%	0.8%	15.7%
		200	0.2%	0.3%	0.5%	0.4%	8.8%	0.2%	12.9%
		all	0.7%	4.2%	3.0%	1.9%	27.7%	1.2%	13.1%

Table 10: Statistically significant results from tensile tests between material groups 42-T1, 52-T1 and 52-T2 and cross-head speeds 2, 20 and 200 mm/min.

	ANOVA Analysis of Significant Effects	
Material Property	Material Type	X-Head Speed (mm/min)
Max Stress	No Significant Effect	2 v 20 2 v 200 20 v 200
Yield Stress	No Significant Effect	2 v 200
Strain @ Yield Point	No Significant Effect	No Significant Effect
X-Head Displacement @ Failure	No Significant Effect	No Significant Effect
Modulus of Elasticity	No Significant Effect	No Significant Effect
Anisotropy Ratio	No Significant Effect	No Significant Effect

The results provided above are discussed below.

4.2.1 Material Variation

The material properties of the two different molecular weight polycarbonate materials are very similar. A large number of samples were tested. to investigate variability. If the 42-T1 and 52-T1 results are compared, the strains at yield point are almost identical but the displacement at failure values suggest that the higher molecular weight specimens can sustain higher degrees of neck growth. This is expected due to the higher molecular chain length. Although the difference is not statistically significant, the modulus of elasticity appears to be lower for the thicker specimen group, 52-T2. The apparently higher modulus for the 52-T1 material could be due to the higher orientation caused by rolling a thinner sheet.

4.2.2 Effect of Strain Rate

As expected, the results show that the yield and maximum strengths increased very slightly with strain rate [6]. The difference between the lowest and highest cross-head speed is about 7%. Although the data shows a hint of strain rate effects on the yield strain and modulus of elasticity, the increases with cross-head are statistically insignificant.

4.2.3 Anisotropy Ratio

The anisotropy ratios for each sample listed in Table 7 were plotted in Figure 4.4. As noted earlier, the anisotropy ratio could not be calculated for some of the thinner samples (see Section 3.2.2). Of the three materials, the thicker 52-T2 had the most consistent failure behaviour with an anisotropy ratio of about 0.53.

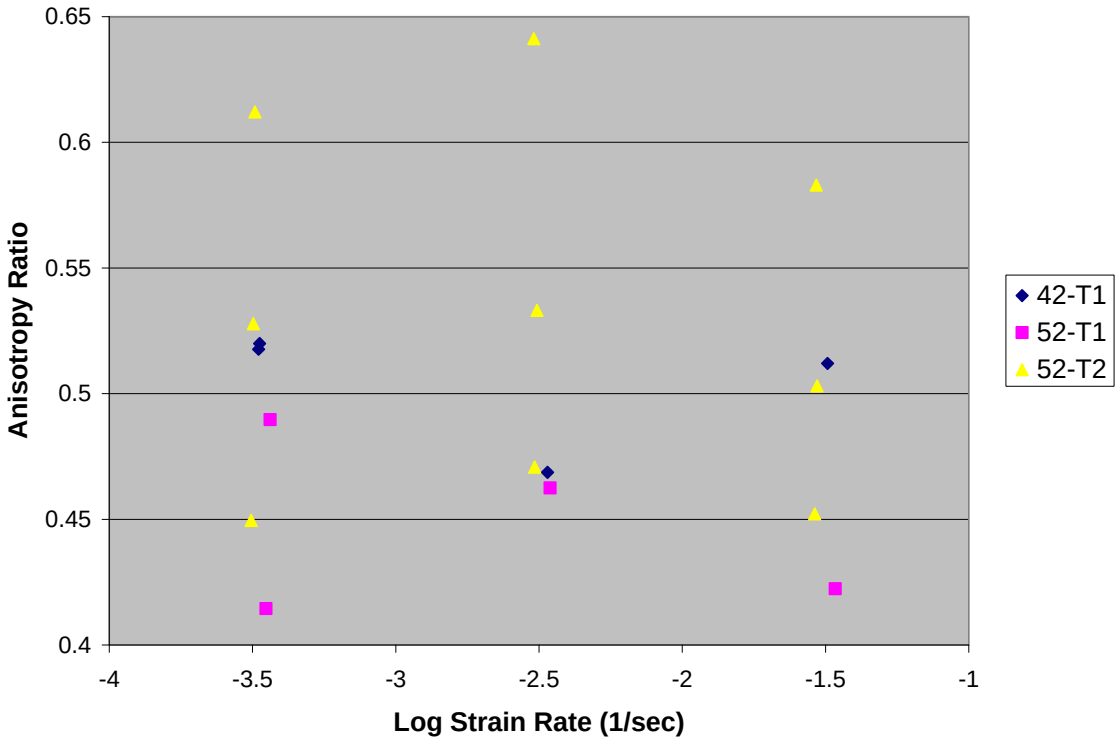

Figure 4.4: Anisotropy ratios for tensile samples in groups 42-T1, 52-T1 and 52-T2.

4.2.4 Activation Volume

The activation volume was calculated from the slope of the plot (σ_y/T) against log (strain rate) as in Eq. **(31)**. Figure 4.5 shows the plots for the three materials. As shown in Table 11, the difference in activation volume between the 42-T1 and 52-T1 samples is negligible. However, the 52-T2 slope appears to be about 10% lower than the other two. Since there is negligible differences in the material free volume and the 52-T2 sheet is twice as thick as 52-T1, it is very possible that the slightly lower activation volume is caused by the differences in microstructural morphology developed during the rolling process. The thinner 42-T1 sheet would have higher level of orientation due to relatively thicker "skin" surfaces, which explains the higher activation volume than 52-T2. This

suggests that the thicker polycarbonate material would be more amenable to yielding and plastic deformation.

Table 11: Activation volume by material.

	Activation Volume (m^3/mol)
42-T1	0.004214
52-T1	0.004096
52-T2	0.003778

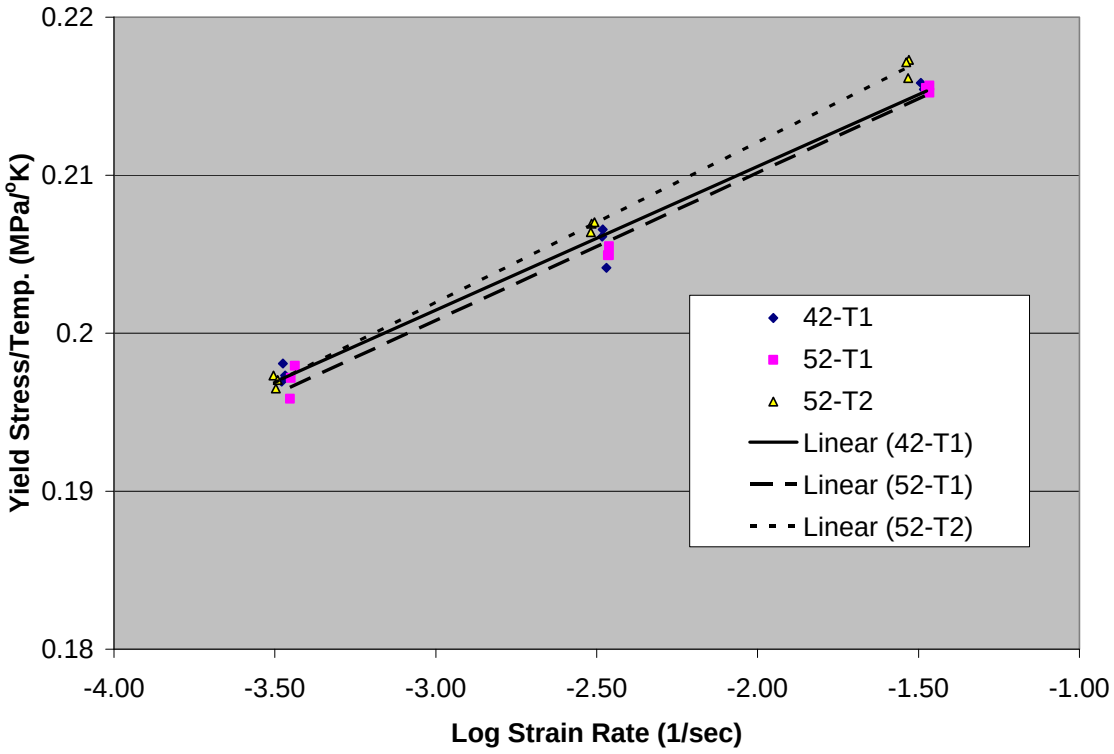

Figure 4.5: The ratio of yield stress to testing temperature vs. logarithmic strain rate. The slope derived from this curve was used in calculating the activation volume, V^*.

4.3 Dome Stretch Forming

A typical set of raw data showing punch force as a function of dome height is plotted in Figure 4.6. The curve displays a small shoulder when it reaches a dome height of approximately 22 mm. This is due to strain softening which is known to occur at the onset of necking [3]. The curve also shows the sudden and catastrophic nature of the failure. Failure was accompanied by a loud "pop" sound as the crack spread across the sample.

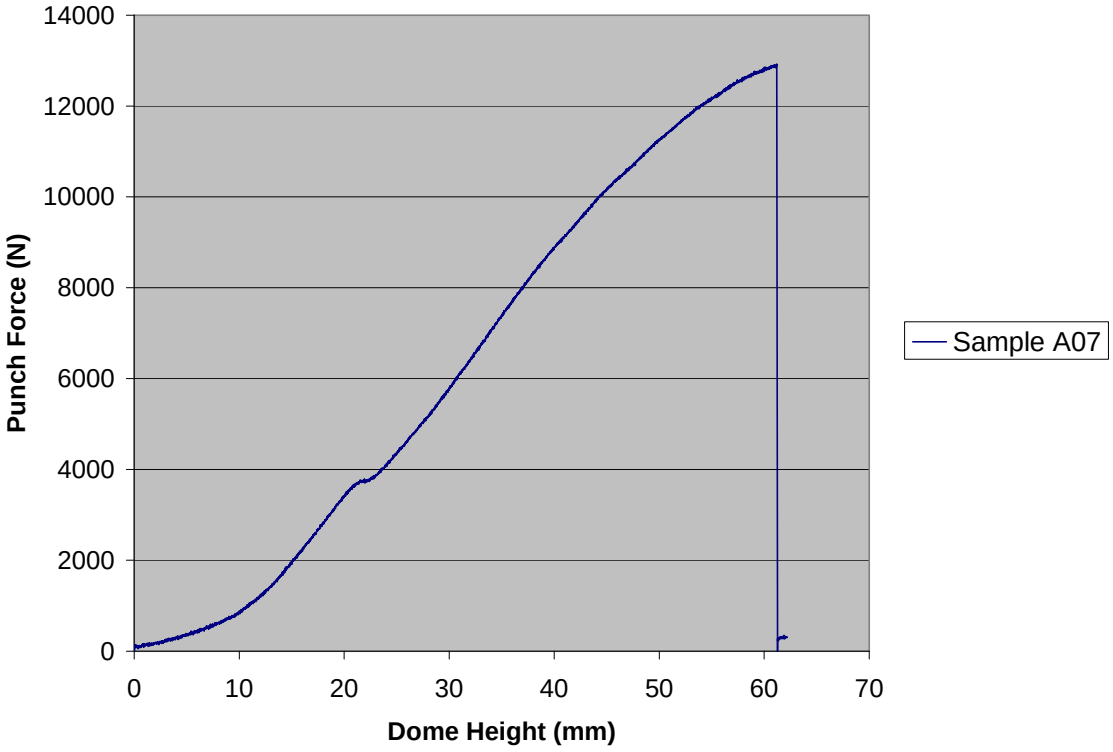

Figure 4.6: Load-displacement curve for a 3" wide specimen from group 42-T1.

Figure 4.7 shows the equivalent stress-strain relationship of the plot in Figure 4.6 as derived in Section 1.3.1. Strain in this case is the major strain along the center-line of the sample. The stress is roughly approximated as the punch force divided by specimen thickness and width.

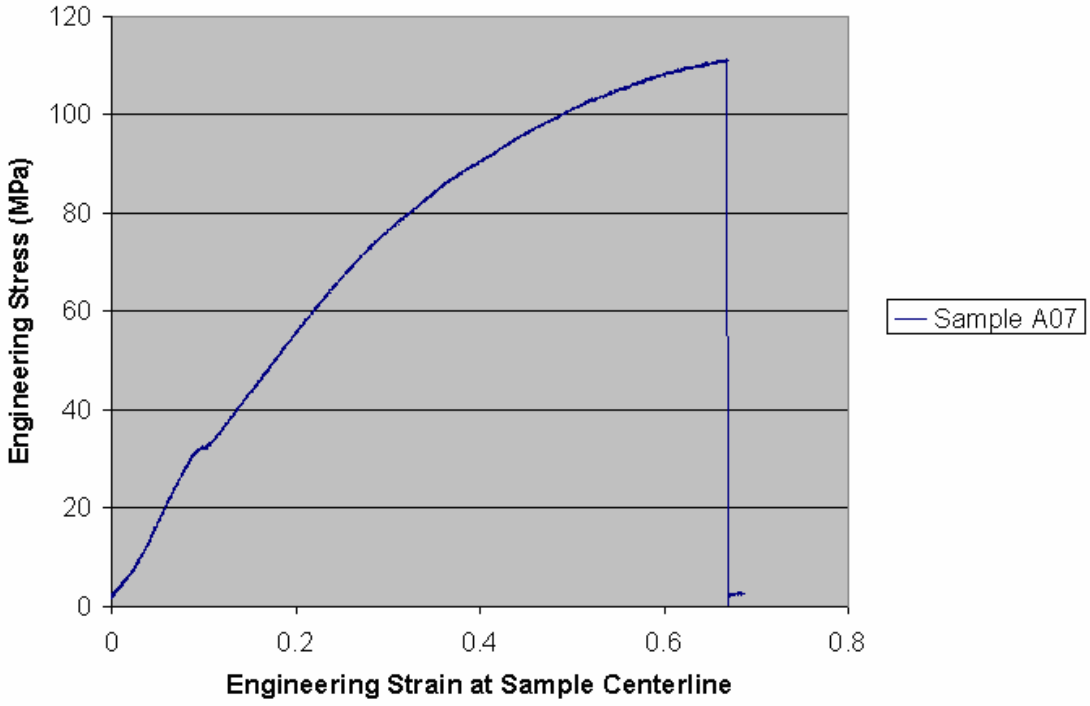

Figure 4.7: Stress-strain curve for a 3" wide specimen from group 42-T1.

The necking patterns in the samples vary with the specimen width. For the narrowest 1"-wide samples, a pair of necked bands formed near the clamped edge and propagated inward toward the center (see Figure 4.8). In slightly wider samples (~3-4"), the necking pattern became more complex. Symmetrical arrays of necked bands formed on the specimens with either two or three bands on each side totalling four or six respectively. As seen in Figure 4.9, the necking pattern of a 3" wide specimen showed near perfect

symmetry with three necked bands per side. With the wider samples that were fully or near fully clamped around the outside, the necks originated in the center of the sample and propagated radially toward the outer clamping area.

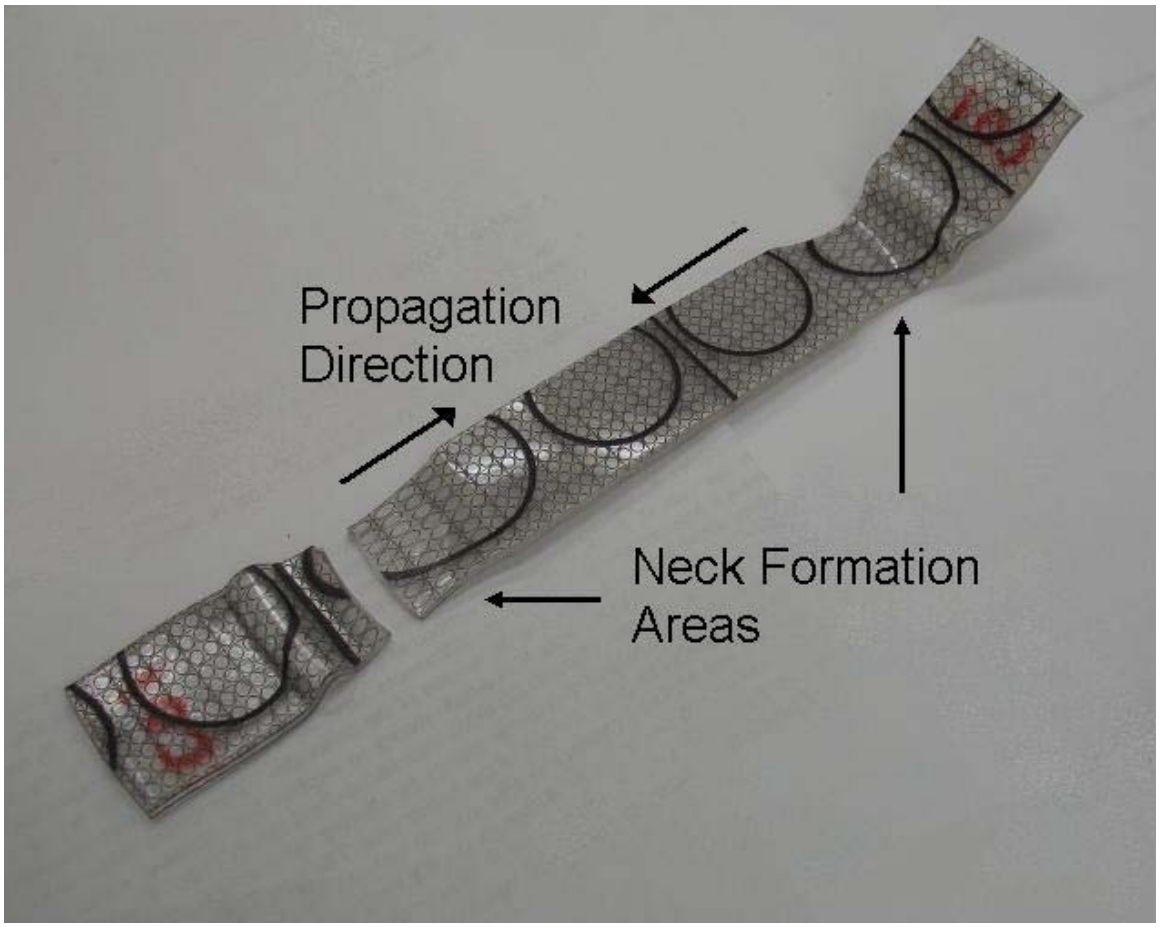

Figure 4.8: Neck formation in 1" wide forming specimens. Pictured sample from group 52-T1.

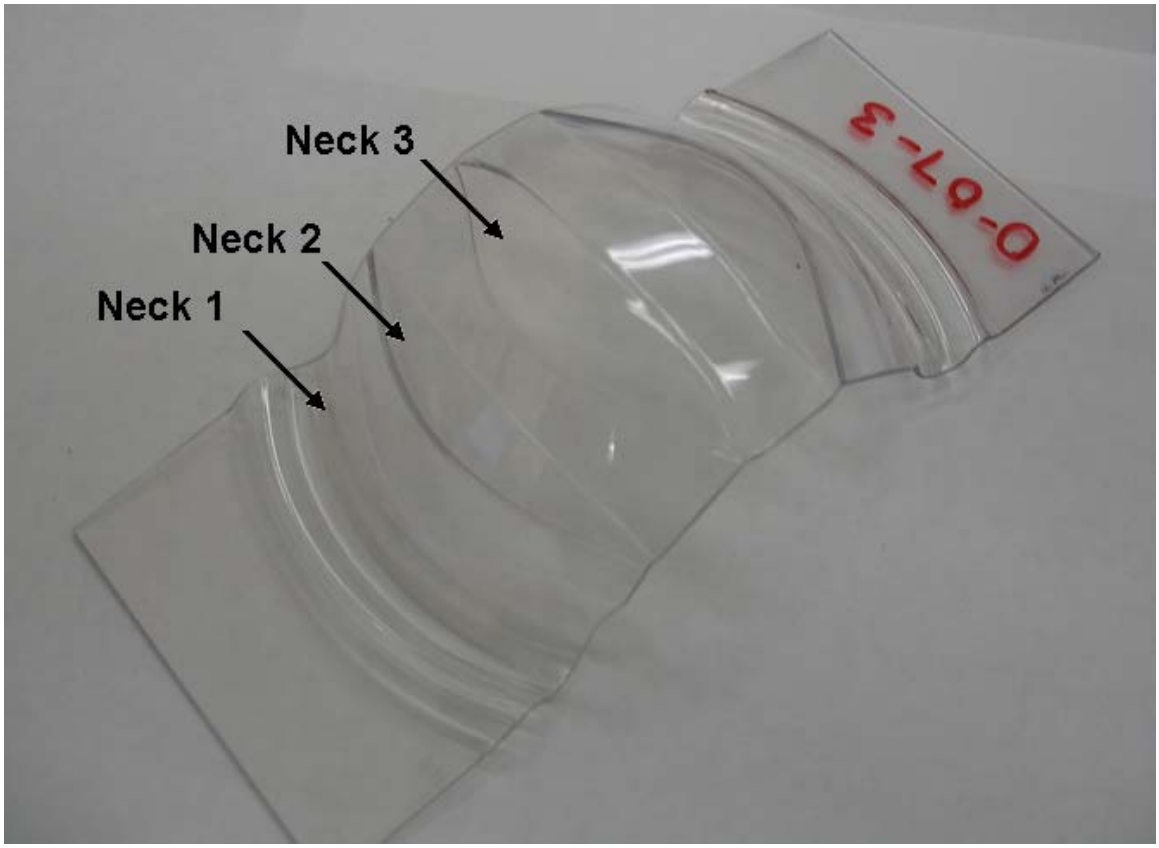

Figure 4.9: Necking pattern of a 3" wide sample. Pictured is an unfractured sample that did not have the circle grid printed in order to better display the neck formation.

4.3.1 Limiting Dome Height (LDH)

In total, three tests were performed for each width of rectangular specimens for each group. One was tested to a predetermined dome height well below failure, while the other two were tested to failure. When the data from the failure tests are plotted in Figure 4.10, the limiting dome height (LDH) increased with increasing specimen width. The LDH, however, reached an upper limit due to the physical constraint of the test equipment. The clamping area where the specimen was held during the test had a diameter of approximately 4.5" (114 mm). As a result, any samples over 4.5" (114 mm) in width were fully clamped and had similar deformation responses. It is also worth

noting that there is a step increase in LDH values from 100 to 125 mm specimen widths for the thicker (3.2 mm) 52-T2 samples. Evidently, the thicker sheets allowed higher levels of forming as long as there is sufficient material in the width direction. This will be discussed further in Section 4.3.2.

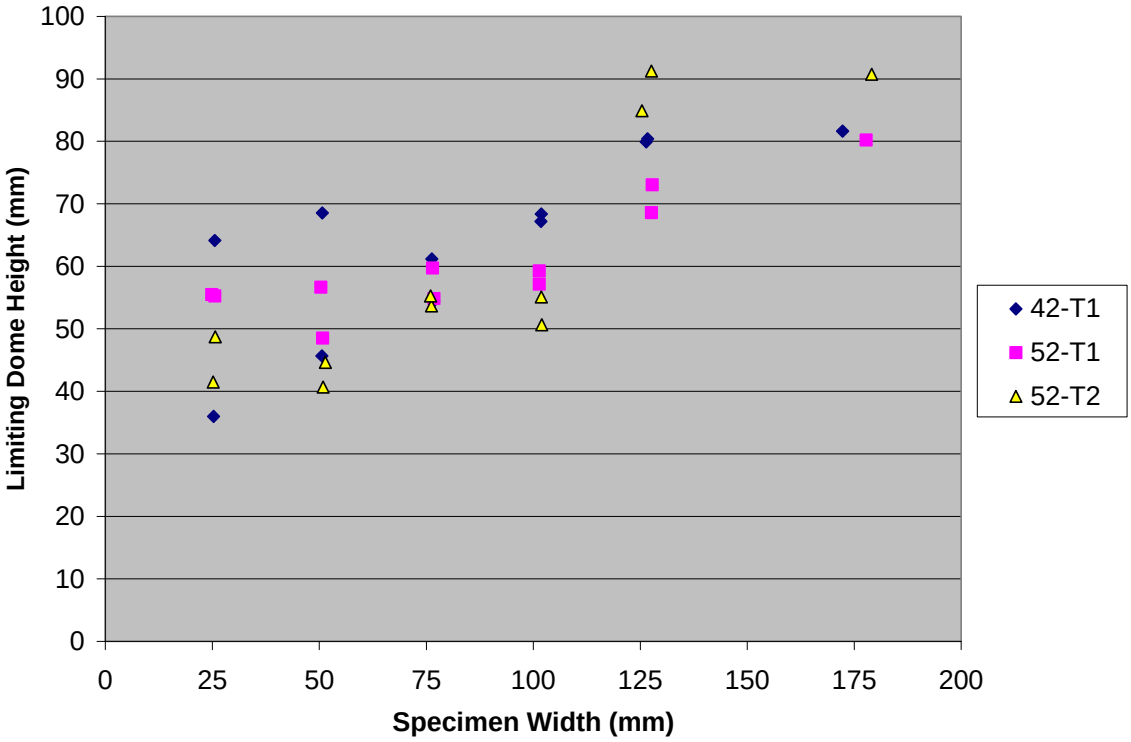

Figure 4.10: LDH diagram for all rectangular forming specimens.

The LDH tests clearly demonstrate that polycarbonate forming is influenced by stress state, particularly the presence of biaxial stresses. Large increases in strain were observed between the tensile test data and the forming data. Table 12 shows the equivalent major strain to failure for forming tests. The major strain for the forming tests was calculated using the method described in Section 1.3.1.

Table 12: Strain to failure for tensile tests tested at 200 mm/min and equivalent strain to failure along the major axis for forming tests.

		Average Major Strain to Failure		
		42-T1	52-T1	52-T2
Dome Forming Specimens	1"	0.489	0.553	0.378
	2"	0.607	0.504	0.339
	3"	0.602	0.591	0.537
	4"	0.812	0.608	0.508
	5"	1.12	0.884	1.34
	7"	1.16	1.12	1.42

4.3.2 Forming Limit Diagrams (FLDs)

The FLDs for 42-T1, 52-T1 and 52-T2 are plotted in Figure 4.11, Figure 4.12 and Figure 4.13 respectively. Each diagram was constructed with over 180 points taken from 28 forming specimens (18 rectangular, 10 dog-bone). Unlike typical FLDs for metals, a slightly different approach was needed to properly analyze the data. FLDs for metallic materials usually have only three zones: "near failure", "necked" and "safe". For polycarbonate it was necessary to add a fourth zone, referred to as the "unstable neck formation" zone. This zone is between the typical safe and necked zones and occurs as a result of the necking process associated with many plastics [8]. Similar to a tensile test, the necked bands form in an unstable manner and are accompanied by decreases in load due to strain softening. The result is a large localized increase in strain where the neck forms and almost no change in strain in the areas adjacent to the necked bands. Once the necking process is initiated, the material behaviour "jumps" immediately from the safe zone to the necked zone.

It is well known that the construction of FLDs is subjective at best and can be influenced by material variability. The latter is reflected in the diagrams constructed in this work. For consistency, the diagrams were plotted using a clear set of criteria. For instance, the failure demarcation line was estimated on the following basis:

(a) the upper limit of necked points

(b) the lower limit of the failure points

Necked regions are readily visible especially in the specimens with necked bands. A failure point was identified as a full circle closest to the failure line, although itself was not cracked. The upper limit demarcation line for the “unstable neck formation zone” is estimated by the lower limit of the necked points.

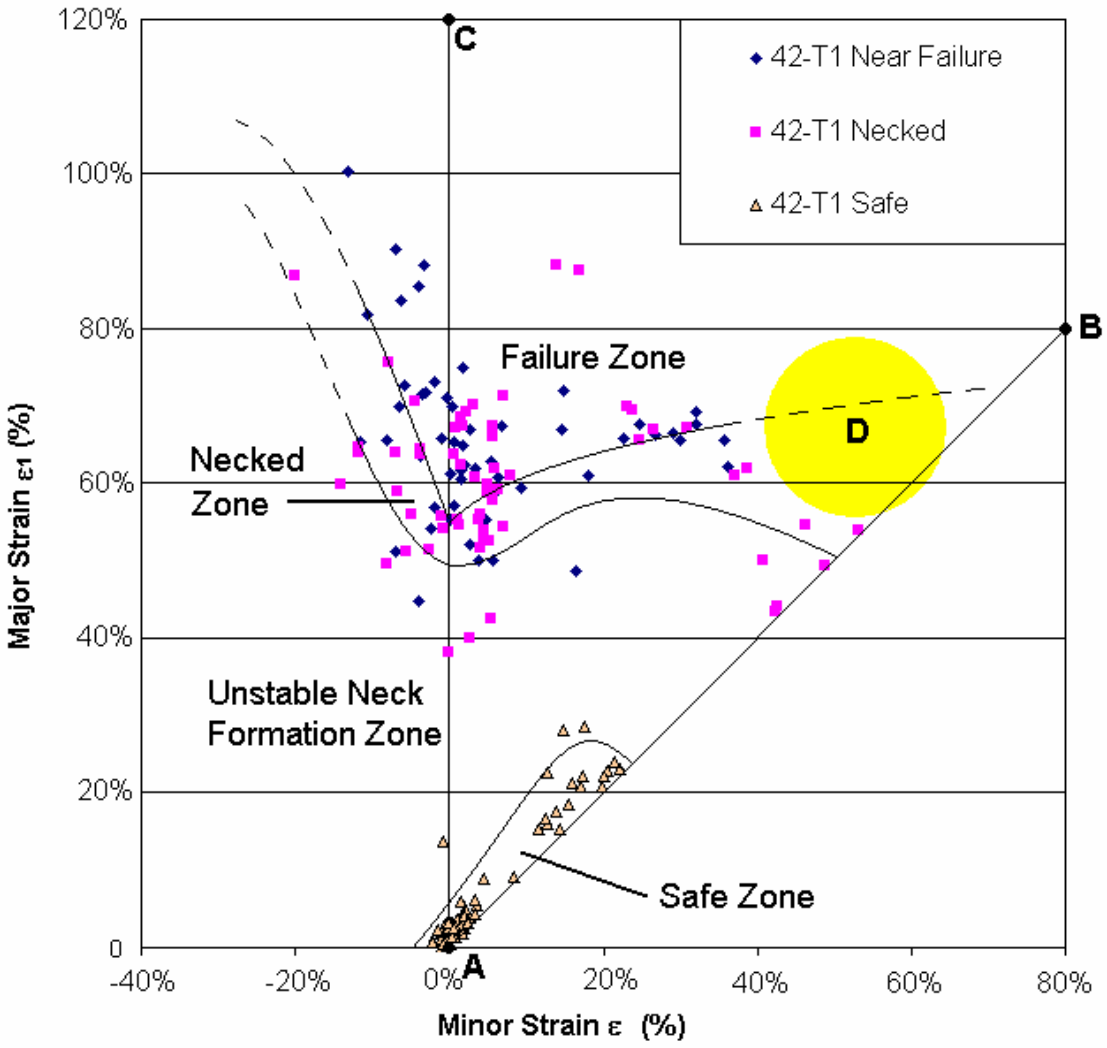

Figure 4.11: Forming limit diagram for group 42-T1.

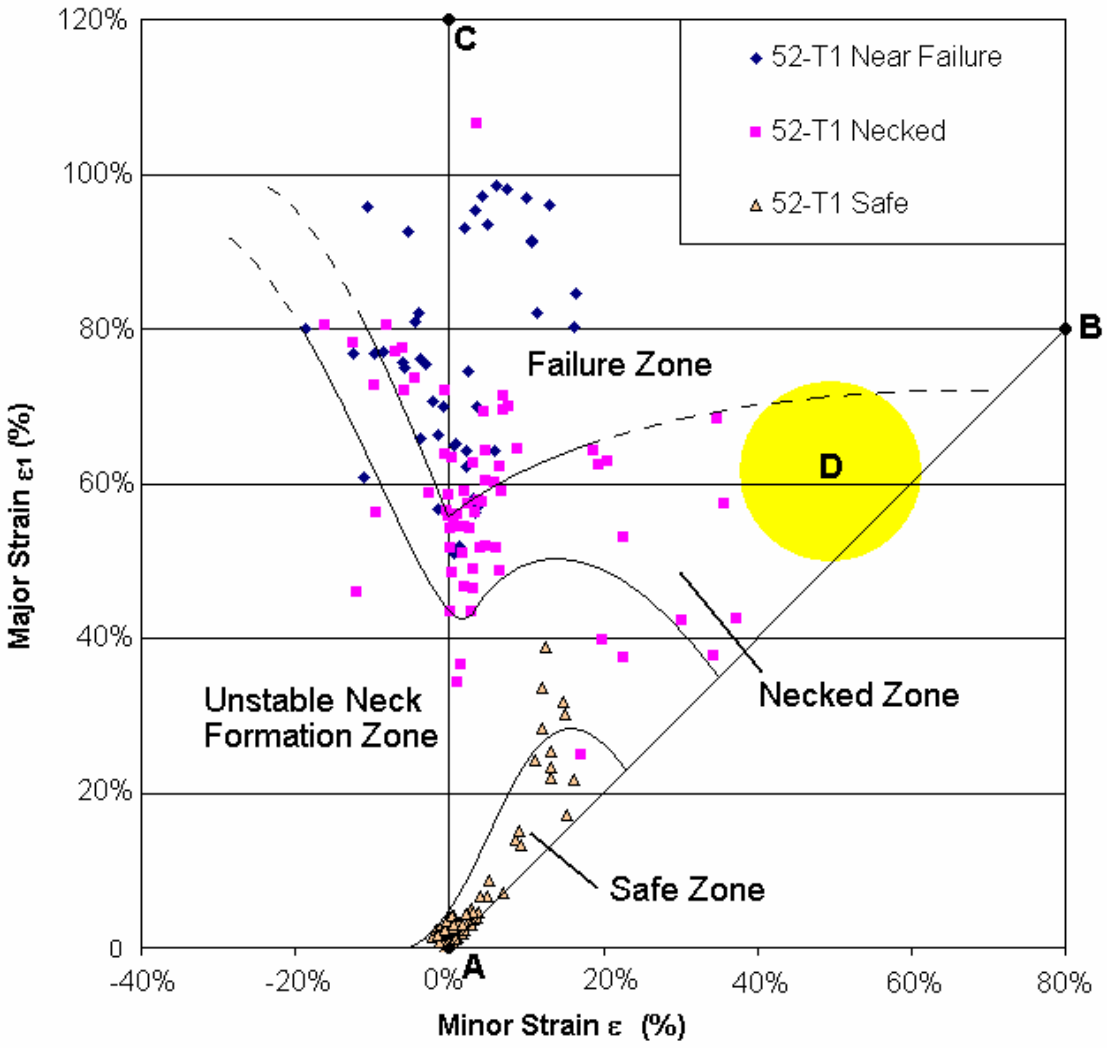

Figure 4.12: Forming limit diagram for group 52-T1.

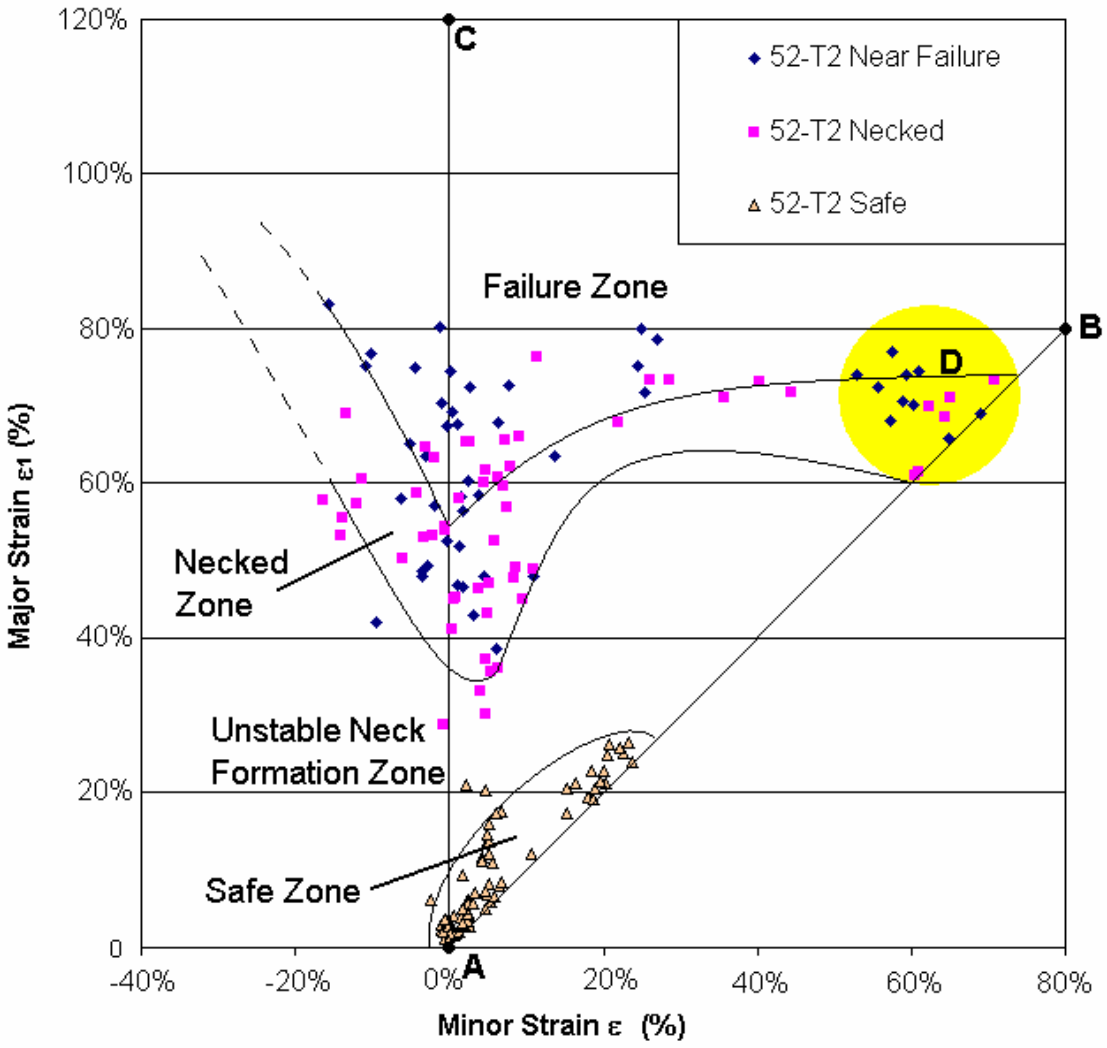

Figure 4.13: Forming limit diagram for group 52-T2.

In Figure 4.11, Figure 4.12 and Figure 4.13 line AB shows the biaxial strain line, where the strain in the major and minor directions is equal ($\varepsilon_1 = \varepsilon_2$). Line AC shows the plane-strain line, where there is no strain in the minor direction ($\varepsilon_2 = 0$). The yellow area, D, is highlighted to show the lack of points near failure for materials 42-T1 and 52-T1.

The failure zone and safe zones were consistent for all three polycarbonates tested. The failure zone descended quickly to approximately 55% major strain at the line AC ($\varepsilon_2 = 0$) and gradually increased with increasing positive minor strain. For the thinner sheets (42-T1 and 52-T1) there were no measurements near failure within area D. This is most likely due to geometry effects. For the thinner samples, the specimen was formed into a dome head that began to elongate at the base. Failure took place at the base, where the strains were no longer biaxial, but closer to uniaxial. For the thicker specimen, the failure occurred through the top of the piece while the strain was still biaxial. The difference in failure modes results in the presence of a large void with no points near failure in area D. Figure 4.14 shows the two different failure modes described.

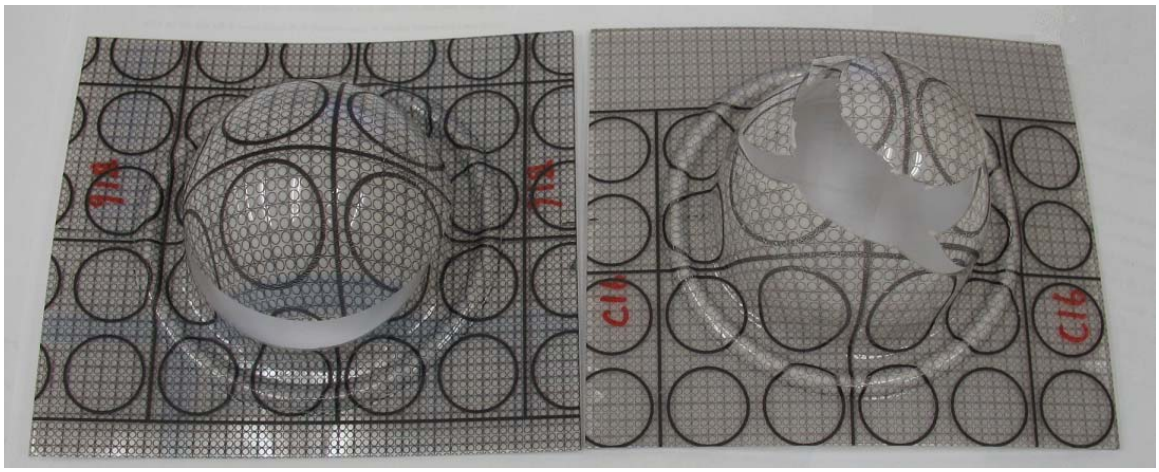

Figure 4.14: Failure mode for 7" wide specimens for 52-T1 (left) and 52-T2 (right).

There is a clear safe zone which indicates that the polycarbonate will experience the largest deformation; this zone runs along line AB ($\varepsilon_1 = \varepsilon_2$). By stretching in both directions at the same time, the unstable neck formation is delayed and significant plastic deformation (without localized necking) can be achieved for all polycarbonate sheets.

The curve separating the unstable neck formation zone and the necked zone varied greatly between the three different polycarbonate materials. The general shape was similar in all cases, but differed slightly from that of most metals [2,14], as illustrated in Figure 1.18. A small decrease in the forming limit curve occurred near line AB that is not common to metals.

Overall, polycarbonate shows good promise as a candidate material that can be stretch formed. The deformations were up to 20% which is comparable to typical metals [14]. However, very large deformation of PC is almost exclusively a post-necking phenomenon. This is opposite to highly formable metals, which have large deformations

before necking begins, and smaller deformations between the onset of necking and eventual failure. This means that although the FLDs show promise for developing PC forming techniques as a feasible industrial process, the end formed product may contain regions of necked material. These regions will differ greatly from the rest of the un-necked material and may not retain the desired mechanical and physical properties typically associated with PC. Instability effects tend to fall away from the biaxial strain line (line AB). Therefore, it is feasible to “safely” form polycarbonate for biaxial strains up to 20%.

5 Conclusions and Recommendations

5.1 Conclusions

Based on the tensile and dome forming tests completed on two different molecular weights and thicknesses of polycarbonate, the following conclusions can be drawn:

- There was minimal difference between the yield stresses and strains of three polycarbonate materials studied even though the molecular weights were quite different. Correspondingly, the activation volumes at yield were not dependent on molecular weight.

- Qualitative comparison of polycarbonate free volume distribution using differential scanning calorimetry showed minimal difference between the two molecular weights.

- Polycarbonate displays characteristics of high formability. The limiting dome height (LDH) for polycarbonate was extremely large in some cases giving equivalent strains greater than 100%. The LDH also greatly increased with specimen width ranging from ~50 mm for 1" -wide specimens to over 90 mm for 7"- wide specimens.

- The forming limit diagrams for polycarbonate are similar to metals with two notable exceptions: a decrease in the forming limit curve occurs near the biaxial

stress line and a large gap containing little to no data between the safe and necked areas. Therefore, instead of fitting a single curve to the boundary between the safe and necked areas, an additional curve was added. One curve was used to show the upper boundary of the safe area, and another to show the lower boundary of the necked area. The area between these lines was referred to as the unstable neck formation area. This zone defines unstable polycarbonte neck formation.

- The three polycarbonate materials tested exhibited different behaviour from metals along the biaxial strain line. Within the safe area, it is possible to achieve "safe" strains up to 20%. However, with uniaxial strain, the "safe" strain is very limited; it is only possible to strain up to 5%. Beyond that, unstable neck formation area occurs,

- The large deformations that occur in polycarbonate take place after necking. This is opposite behaviour to metals, which can sustain large deformations before necking and eventual failure. This is expected based on the differences in stress-strain curves of polycarbonate and metals, although it brings a unique complication to forming. Although polycarbonate displays good forming characteristics, necking took place early in the process, continuing until failure.

- It is possible to cold-form polycarbonate as long as the process avoids unstable neck formation conditions.

5.2 Recommendations

Research in this area has only just begun. There are many different process avenues yet to be explored and recommendations for future works include:

- More FLDs should be created and materials of different molecular weights should be studied. There are other factors that affect the forming characteristics, but have not yet been characterized. The formability as affected by strain rate, small temperature changes (below T_g), thermal aging and mechanical aging are of particular interest.

- Springback is a major obstacle of forming, but has not been studied. Advancing polymer forming technology requires the characterization of springback effects.

- Biaxial stress effects should be further explored for polycarbonate.

- A bulk property analysis of necked polycarbonate should be done. Material property data would need to be completed if formed parts containing polycarbonate necks were manufactured. Temperature effects should also be explored to be sure that the material would maintain its structural integrity through the same range.

References

1 W. Callister. *Materials Science and Engineering – An Introduction.* Sixth Edition. John Wiley & Sons, Inc. New York, NY. (2003).

2 S. Kalpakjian, S.R. Schmid. *Manufacturing Processes for Engineering Materials*. Fourth Edition. Pearson Education, Inc. Upper Saddle River, NJ. (2003).

3 M.C. Boyce, D.M. Parks, A.S. Argon. *Large Inelastic Deformation of Glassy Polymers. Part I: Rate Dependant Constitutive Model*. Mechanics of Materials. (1988) 7:15-33.

4 P. Quinson, J. Perez, M. Rink, A. Pavan. *Yield Criteria for Glassy Polymers*. Journal. of Material Science. (1997) 32:1371-1379.

5 Z.H. Stachurski. *Deformation Mechanisms and Yield Strength in Amorphous Polymers*. Progress in Polymer Science. (1997) 22:407-474.

6 N.G. McCrum, C.P. Buckley, C.B. Bucknall. *Principles of Polymer Engineering*. Oxford University Press. Toronto, ON. (1988)

7 Z. Xixong. *Analysis of Mechanical Behavior in Cold-Drawing Deformation of Polymers*. Journal of Polymer Science: Part B: Polymer Physics. (1993) 31:1667-1675.

8 D.G. Fesko. *Post-Yield Behavior of Thermoplastics and the Application to Finite Element Analysis.* Polymer Engineering and Science. (2000) 40(5):1190-1199.

9 A.P. Boresi, R.J. Schmidt. *Advanced Mechanics of Materials*. Sixth Edition. John Wiley & Sons, Inc. Danvers, MA. (2003)

10 G.E. Dieter, H.A. Kuhn, S.L. Semiatin. *Handbook of Workability and Process Design*. ASM International. Materials Park, OH. (2003).

11 S. Hashemi. *Plane-Stress Fracture of Polycarbonate Films*. Journal of Materials Science. (1993) 28:6178-6184.

12 J.A. Schey. *Introduction to Manufacturing Processes.* Second Edition. McGraw-Hill Inc. Toronto, ON. (1987).

13 Y.W. Lee, N.N.S. Chen, P.I.F. Niem. *The Effect of Cold Rolling on the Formability of Polymers*. Plastics and Rubber Processing and Applications. (1987) 7:221-228.

14 ASTM E 2218 – 02. *Standard Test Method for Determining Forming Limit Curves*. ASTM International, West Crocken PA. (2006).

15 R.H. Wagoner, K.S. Chan, S.P. Keeler. *Forming Limit Diagrams: Concepts, Methods and Applications.* The Minerals, Metals & Materials Society. Warrandale, PA. (1989).

16 J.L. Thorne. *Thermoforming.* Hanser Publishers. New York, NY. (1987).

17 G. Gruenwald. *Thermoforming: A Plastics Processing Guide.* Technomic Publishing Company, Inc. Lancaster, PA. (1987).

18 Y.W. Lee. *Formability of Cold-Rolled Poly(Vinyl Chloride).* Plastics and Rubber Processing and Applications. (1990) 13:29-35.

19 Y.W. Lee, *The Forming Properties of High Molecular Weight Polyethylene*. Journal of Applied Polymer Science. (1991) 43:29-37.

20 L.E. Govaert, T.A. Tervoort. *Strain Hardening of Polycarbonate in the Glassy State: Influence of Temperature and Molecular Weight*. Journal of Polymer Science; Part B: Polymer Physics. (2004) 42:2041-2049.

21 M. Wendalt, T.A. Tervoort, U.W. Suter. Non-linear Strain-hardening Behaviour of Polymer Glasses. Polymer. (2005) 46:11786-11797.

22 W. Brostow, R.D. Corneliussen. *Failure of Plastics*. Hanser Publishers. New York, NY. (1989).

23 L.A. Utracki and T. Sedlacek. *Free Volume Dependence of Polymer Viscosity*. Rheol. Acta. (2007) 46:479-494.

24 Q. Guo, C.B. Park, X. Xu, J. Wang. *Relationship of Fractional Free Volumes Derived from the Equations of State (EOS) and the Doolittle Equation*. Journal of Cellular Plastics. (2007) 43(1):69-82.

25 A. K. Doolittle. *Studies in Newtonian Flow II. The Dependence of the Viscosity of Liquids on Free-Space*. Journal of Applied Physics. (1951) 28(8):1471-1475.

26 J. Ho, L. Govaert, M. Utz. *Plastic Deformation of Glassy Polymers: Correlation between Shear Activation Volume and Entanglement Density*. Macromolecules. (2003) 36:7398-7404.

27 *The Arrhenius Equation.* http://www.shodor.org/UNChem/advanced/kin/arrhenius.html University of North Carolina at Chapel Hill. [August 2008]

28 Z. Zhou, A. Chudnovsky, C. P. Bosnyak, K. Sehanobish. *Cold-Drawing (Necking) Behavior of Polycarbonate as a Double Glass Transition*. Polymer Engineering and Science. (1995) 35(4):304-309.

29 A. Masud, A. Chudnovsky. *A Constitutive Model of Cold-Drawing in Polycarbonates*. International Journal of Plasticity. (1999) 15:1139-1157.

30 R.N. Haward, G. Thackray. *Use of a Mathematical Model to Describe Isothermal Stress-Strain Curves in Glassy Thermoplastics*. Proceedings of the Royal Society of London, Series A (Mathematical and Physical Sciences). (1968) 302(23):453-472.

31 E.A. Arruda, M.C. Boyce. *Evolution of Plastic Anisotropy in Amorphous Polymers During Finite Straining*. International Journal of Plasticity. (1993) 9:607-720.

32 *Polycarbonate Products*. http://www.nalgene-outdoor.com/PDFs/PC_Safety-April_25_2006.pdf American Plastics Council. [August 2008]

33 *Polycarbonate Plastic*. http://www.sdplastics.com/polycarb.html San Diego Plastics, Inc. [August 2008]

34 D.J. Brunelle, M.R. Korn. *Advances in Polycarbonates.* American Chemical Society. Washington, DC. (2005).

35 *Lexan* http://en.wikipedia.org/wiki/Image:Lexan.png [August 2008]

36 D. Cangialosi, H. Schut, A. van Veen, S.J. Picken. *Positron Annihilation Lifetime Spectoscopy for Measuring Free Volume during Physical Aging of Polycarbonate*. Macromolecules. (2003) 36:142-147.

37 E. Kontou. *Effect of Tthermal Treatments on the Yielding of Polycarbonate*. Journal of Applied Polymer Science. (2005) 98:796-805.

38 R.W. Hertzberg. *Deformation and Fracture Mechanics of Engineering Materials*. Fourth Edition. John Wiley and Sons Inc. New York, NY. (1996).

39 P. Lee-Sullivan, M. Bettle. *Comparison of Enthalpy Relaxation Between Two Different Molecular Masses of Bishpenol-A Polycarbonate.* Journal of Thermal Analysis and Calorimetry. (2005) 81:167-177.

40 J.M. Hutchinson, S. Smith, B. Horne, G.M. Gourlay. *Physical Aging in Polycarbonate: Enthalpy Relaxation, Creep Response and Yielding Behavior.* Macromolecules. (1999) 32:5046-5061.

41 S.E.B. Petre. Thermal Behavior of Annealed Organic Glasses. Journal of Polymer Science: Part A-2. (1972) 10:1255-1272.

42 ASTM D 638 – 03. *Standard Test Method for Tensile Properties of Plastics*. ASTM International, West Crocken PA. (2006).

43 D.C. Montgomery. *Design and Analysis of Experiments*. Sixth Edition. John Wiley & Inc. New York, NY. (2005).

APPENDIX A:

Material Data Sheets

SABIC Innovative Plastics™

Lexan* 9030 and Lexan* 9030 TG Sheet

Product Datasheet

Description

Lexan* 9030 sheet is the standard Lexan sheet without UV nor Mar resistant surface treatment. Lexan 9030 sheet combines high impact and temperature resistance with optical clarity and can be utilized for secondary glazing behind existing glazing for economical protection against breakage or intrusion. Lexan 9030 sheet can be cut, sawn, drilled and milled by using standard workshop equipment without the risk of cracking and breakage and is therefore an excellent candidate for fabricating a wide range of indoor applications such as machine guards etc. Lexan 9030 sheet can be easily thermoformed into complex parts while retaining its excellent properties necessary for demanding applications such as vandal proof street furniture. Lexan 9030 sheet may be decorated using a wide variety of modern techniques such as painting and screen printing.

Typical Property Values ◆

Property		Test Method	Unit	Value
Physical				
Density		ISO 1183	g/cm³	1.20
Water absorption, 50% RH / 23 °C		ISO 62	%	0.15
Water absorption, saturation /23°C		ISO 62	%	0.35
Mould shrinkage		SABIC-Method	%	0.6-0.8
Poison's ratio		ASTM-D638	-	0.38
Mechanical				
Tensile stress at yield 50 mm/min		ISO 527	MPa	60
Tensile stress at break 50 mm/min		ISO 527	MPa	70
Tensile strain at yield 50 mm/min		ISO 527	%	6
Tensile strain at break 50 mm/min		ISO 527	%	120
Tensile modulus 1 mm/min		ISO 527	MPa	2300
Flexural stress at yield 2 mm/min		ISO 178	MPa	90
Flexural modulus 2 mm/min		ISO 178	MPa	2300
Hardness H358/30 95		ISO 2039/1	MPa	95
Impact				
Charpy impact, notched		ISO 179/1C	kJ/m²	35
Izod impact, unnotched 23°C		ISO 180/4U	kJ/m²	NB
Izod impact, unnotched -30°C		ISO 180/4U	kJ/m²	NB
Izod impact, notched 23°C		ISO 180/4A	kJ/m²	65
Izod impact, notched -30°C		ISO 180/4A	kJ/m²	10
Thermal				
Vicat Softening Temperature, rate B/120		ISO 306	°C	145
HDT/Ae, 1.8 MPa edgew. 120*1*04/sp=100		ISO 75	°C	127
Thermal conductivity		ISO 8302	W/m.°C	0.2
Coeff.of Lin.Therm.Exp.extr. 23-80°C		ISO 11359-2	1/°C	7.00 E-05
Ball pressure test 125 ±2°C		IEC 60695-10-2	-	Passes
Relative Thermal Index. Electrical Properties		UL746B	°C	130
Relative Thermal Index. Mech. prop.with impact		UL746B	°C	125
Relative Thermal Index. Mech.prop.w/o impact		UL746B	°C	125
Electrical				
Volume Resistivity		IEC 60093	Ohm.cm	10 E15
Relative Permittivity	50/60Hz	IEC 60250	-	2.7
Relative Permittivity	1Mhz	IEC 60250	-	2.7
Dissipation Factor	50/60 Hz	IEC 60250	-	0.001
Dissipation Factor	1 Mhz	IEC 60250	-	0.01
Arc Resistance Tungsten	ASTM-D495	sec.	119	
Optical				
Light transmission ¥) 3 mm		ASTM-D1003	%	89

◆ These property values have been derived from Lexan*resin data for the material used to produce this sheet product. Variation within normal tolerances are possible for various colors. These typical values are not intended for specification purposes. If minimum certifiable properties are required please contact your local SABIC Innovative Plastics, Specialty Film & Sheet representative. All values are measured at least after 48 hours storage at 23°C/50% relative humidity. All properties are measured on injection molded samples. All samples are prepared according ISO 294.

¥) Light transmission value may vary by + or - 5%.

Lexan*

SABIC Innovative Plastics™

Lexan* 9030 and Lexan* 9030 TG Sheet

Product Datasheet

Light transmission

Transparent Lexan 9030 sheet have excellent light transmission, dependent of thickness between 84 - 87%.

Fire performance

Lexan* 9030 sheet has good fire behavior characteristics. Lexan sheet does not contribute significantly to the spread of fire or to the generation of toxic gases. For details please contact your local sales office.

Product Availability •)

Lexan 9030TG sheet:

Standard Sizes	Masking	Standard Colors
Thin gauge in mm	0.75#-1-1.5	
625 x 1250#	Top side: Coex opal white PE	transparent code 112 and
1250 x 1250	dark blue print	opal white code 82103
Bottom Side:	Coex transparent PE	

Lexan 9030 sheet:

Standard gauge in mm	2-3-4-5-6-8-9.5-12-15	
2050 x 3050	Top side: Coex opal white PE	transparent code 112 and
2050 x 6050	dark blue print	opal white code 82103
Bottom Side:	Coex transparent PE	

#Dimensions only for 0.75 mm.

•) Lexan* 9030 sheet can be supplied by prior arrangements in non - standard widths, lengths and color. Such arrangements may affect prices, terms and/or other conditions of sales and are subject to minimum order quantities.

Lexan* Polycarbonate Sheet — Tough Virtually Unbreakable

* Trademark of SABIC Innovative Plastics IP BV

Americas:
SABIC Innovative Plastics
Specialty Film & Sheet
One Plastics Avenue
Pittsfield, MA 01201
USA
Tel. (1) (413) 448 5400
Fax. (1) (413) 448 7506
Toll free: 1-800 451 3147

Europe:
SABIC Innovative Plastics
Specialty Film & Sheet
Plasticslaan 1
NL - 4612 PX Bergen op Zoom
The Netherlands
Tel. (31) (164) 292911
Fax. (31) (164) 293272

Pacific:
SABIC Innovative Plastics
Specialty Film & Sheet
1266 Nanjin Road (W)
Plaza 66, 17th Floor
200040 Shanghai, China
Tel. (86) 21 62881088
Fax. (86) 21 62880818

www.sabic-ip.com

Latest update SABIC 01/2008

APPENDIX B:

GPC Data Reports

Group 42-T1 Data (Two runs from two samples)

Avg. Molecular Wt.

Sample ID	Run #	Mn	Avg.	Mw	Avg.	Mz	Avg.	Mw/Mn	Avg.
Sample#1	1	8,589	8,599	42,928	42,680	66,315	65,985	5.00	4.96
	2	8,609		42,432		65,655		4.93	
Sample#2	1	10,212	10,071	42,195	42,156	65,229	65,088	4.13	4.19
	2	9,930		42,116		64,946		4.24	

Relative to polystyrene standards

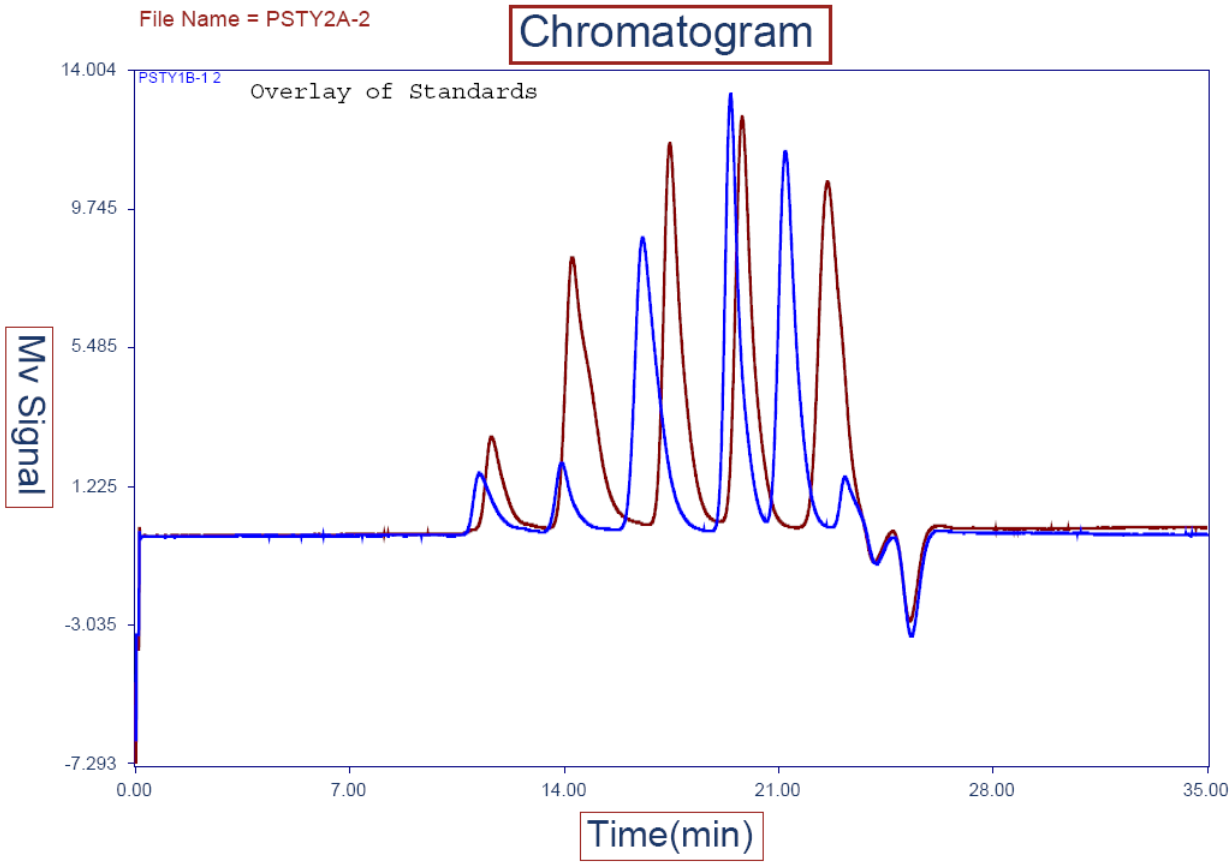

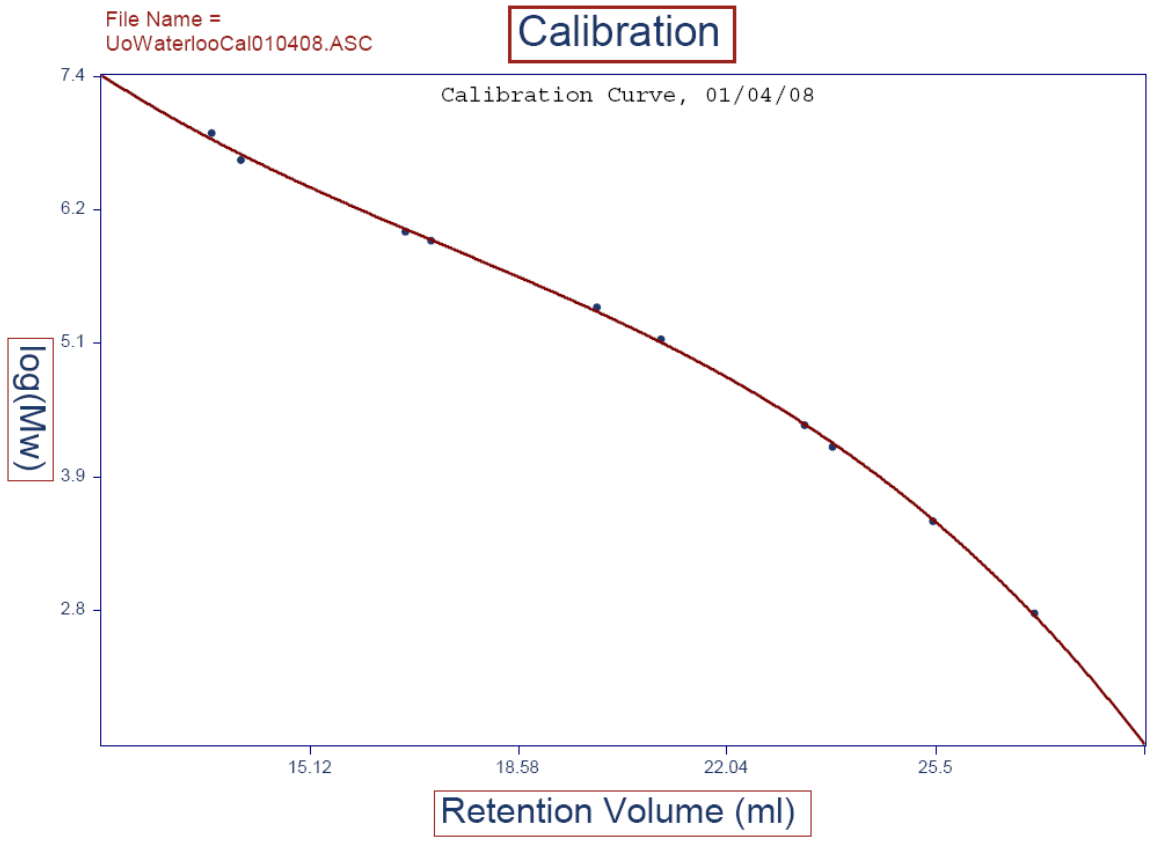
File Name =
UoWaterlooCal010408.ASC
Calibration
Calibration Curve, 01/04/08
7.4
6.2
5.1
3.9
2.8
log(Mw)
15.12
18.58
22.04
25.5
Retention Volume (ml)

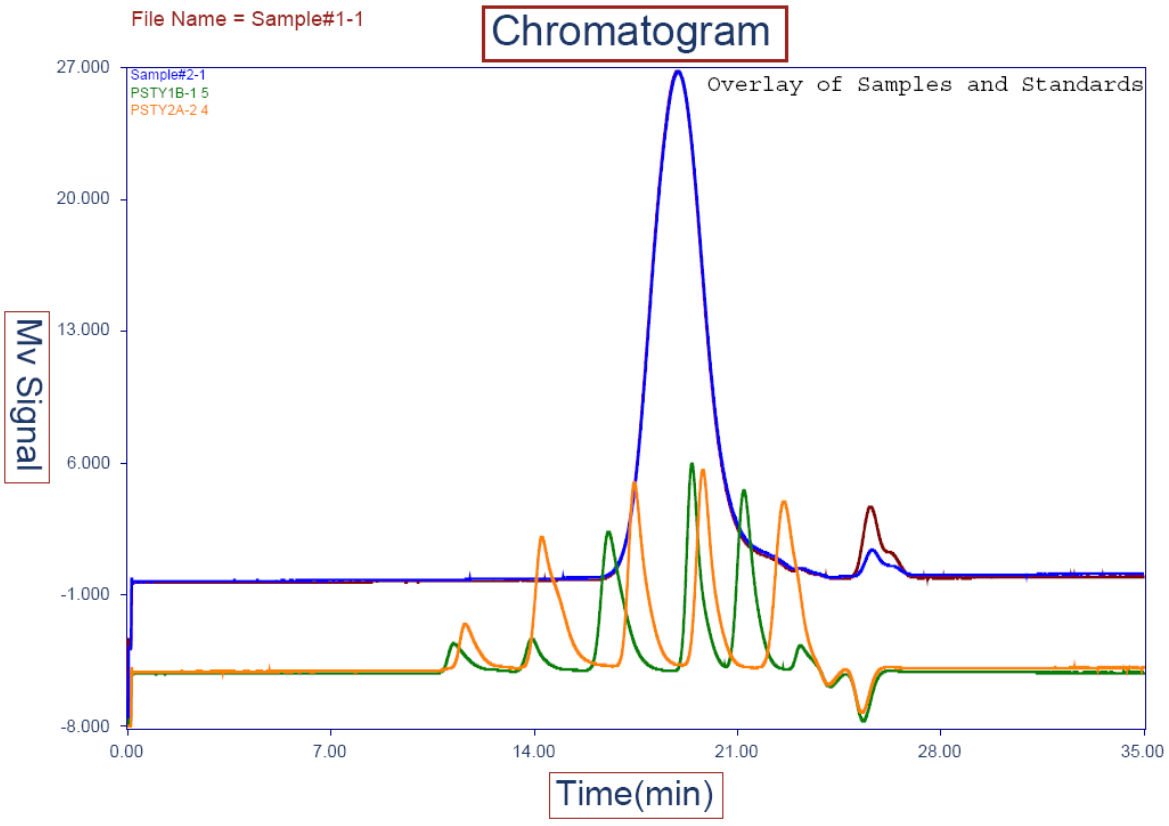
File Name = Sample#1-1
Chromatogram
Sample#2-1
PSTY1B-1 5
PSTY2A-2 4
Overlay of Samples and Standards
27.000
20.000
13.000
6.000
-1.000
-8.000
Mv Signal
0.00
7.00
14.00
21.00
28.00
35.00
Time(min)

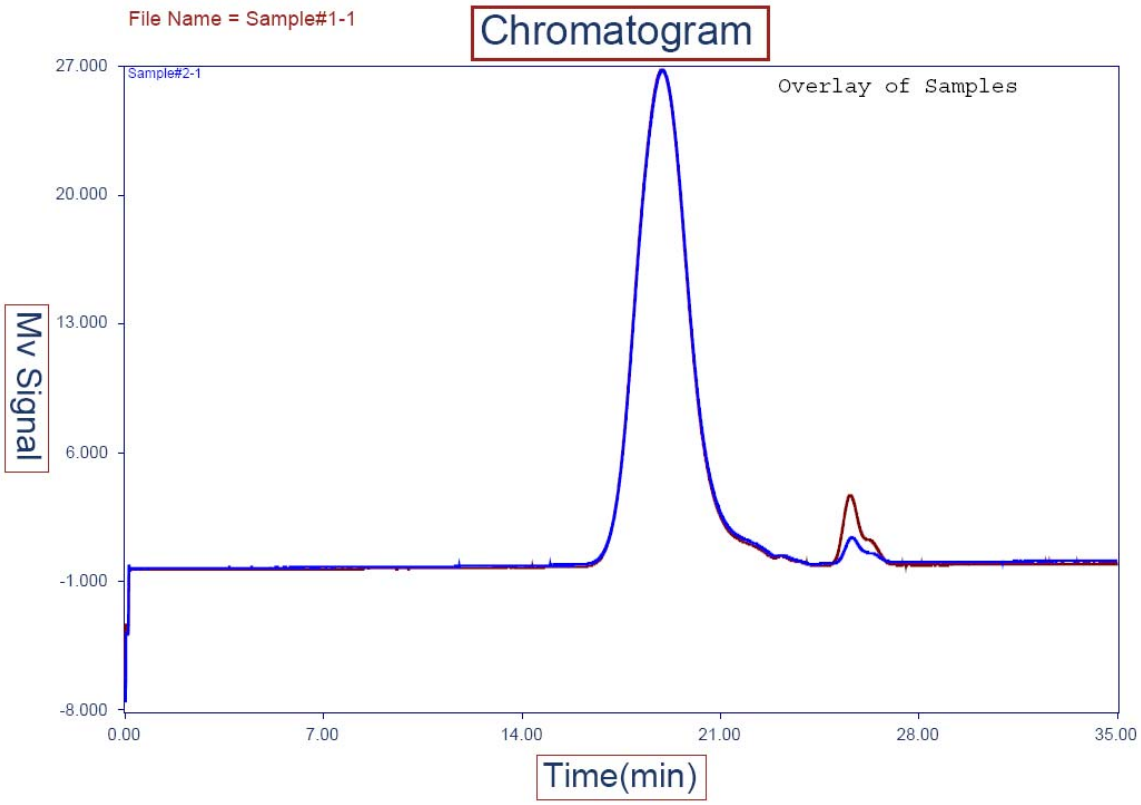
File Name = Sample#1-1
Chromatogram
Sample#2-1
Overlay of Samples
27.000
20.000
13.000
6.000
-1.000
-8.000
Mv Signal
0.00
7.00
14.00
21.00
28.00
35.00
Time(min)

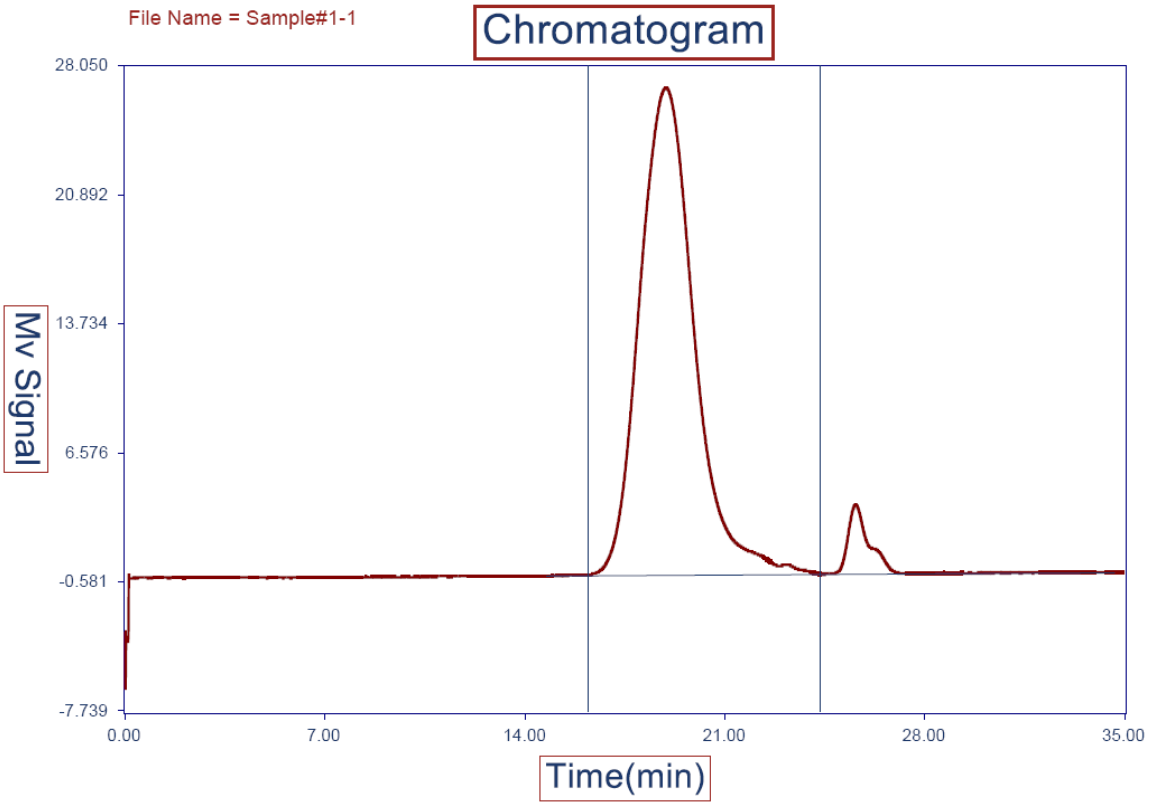
File Name = Sample#1-1
Chromatogram
28.050
20.892
13.734
6.576
-0.581
-7.739
Mv Signal
0.00
7.00
14.00
21.00
28.00
35.00
Time(min)

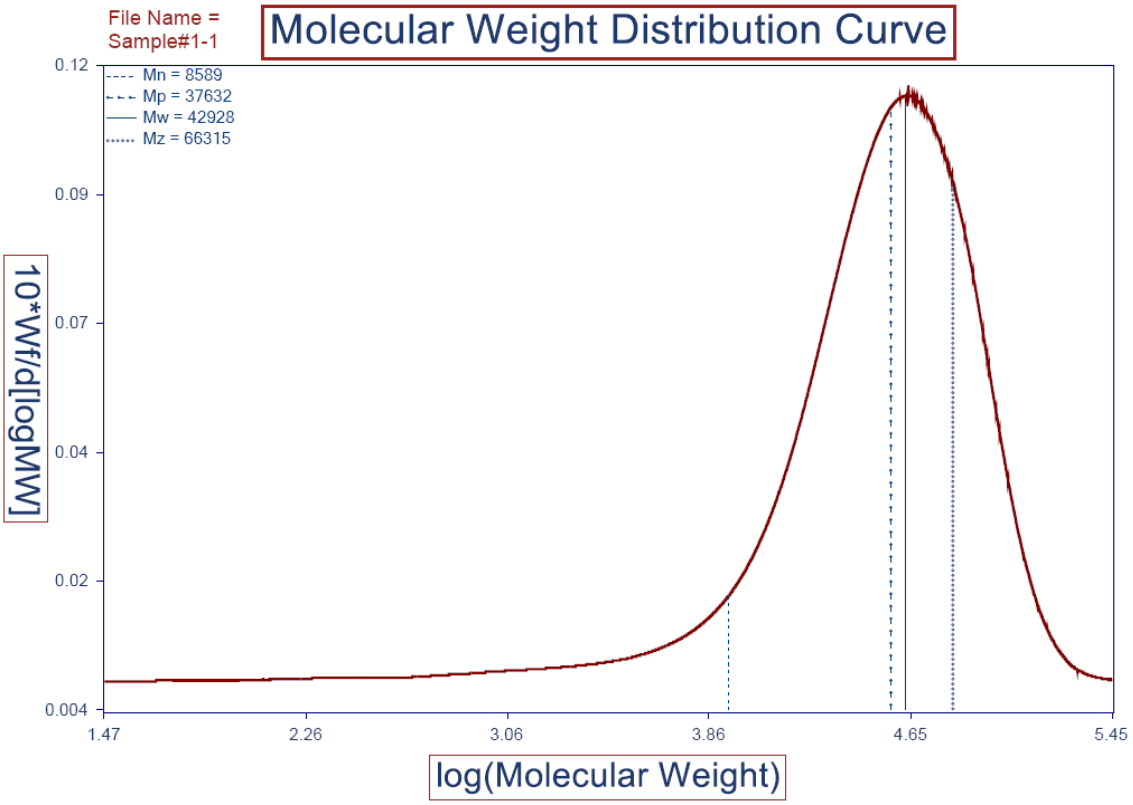
File Name =
Sample#1-1
Molecular Weight Distribution Curve
Mn = 8589
Mp = 37632
Mw = 42928
Mz = 66315
10*Wf/d[logMW]
0.12
0.09
0.07
0.04
0.02
0.004
1.47
2.26
3.06
3.86
4.65
5.45
log(Molecular Weight)

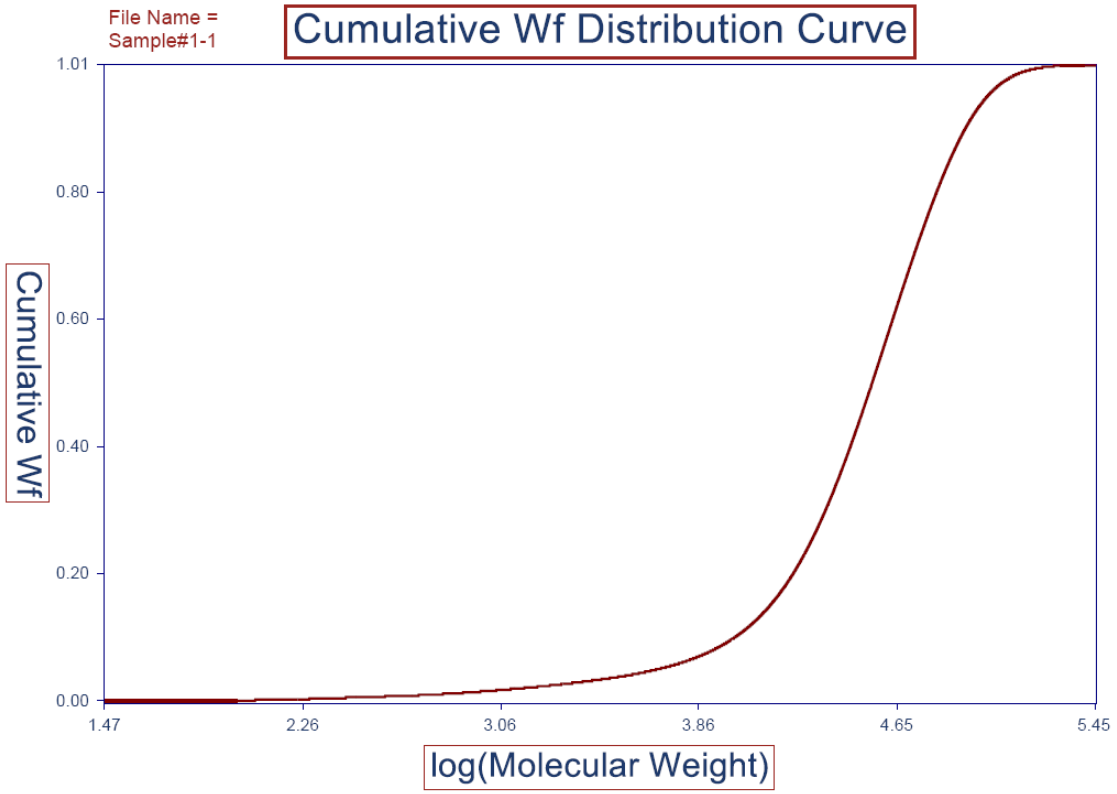
File Name =
Sample#1-1
Cumulative Wf Distribution Curve
Cumulative Wf
1.01
0.80
0.60
0.40
0.20
0.00
1.47
2.26
3.06
3.86
4.65
5.45
log(Molecular Weight)

Summary of Molecular Weights

File Name = Sample#1-1.ASC
Sample Name = Unknown
Calibration File Name = UoWaterlooCal010408.ASC

Number Average Molecular Weight (Mn) = 8589
Weight Average Molecular Weight (Mw) = 42928
Z Average Molecular Weight (Mz) = 66315
Peak Maximum Molecular Weight (Mp) = 37632
Polydispersity = 5.00
Peak Area = 36005

Integration Limits =
Left = 19.45
Right = 29.24

Mobile Phase = THF
Detector = Refractive Index
Concentration = 2.5 mg/ml
Run Date = 1/3/2008 11:48:27 AM
Column = Jordi Gel DVB Mixed Bed 50cm x 10cm

Temperature = 45 ° C
Inj. Volume = 200 uL
Flow Rate = 1.2 ml/min

Comments = None

Summary of Molecular Weights

File Name = Sample#1-2
Sample Name = Unknown
Calibration File Name = UoWaterlooCal010408.ASC

Number Average Molecular Weight (Mn) = 8609
Weight Average Molecular Weight (Mw) = 42432
Z Average Molecular Weight (Mz) = 65655
Peak Maximum Molecular Weight (Mp) = 37154
Polydispersity = 4.93
Peak Area = 36041

Integration Limits =
Left = 19.45
Right = 29.24

Mobile Phase = THF
Detector = Refractive Index
Concentration = 2.5 mg/ml
Run Date = 1/3/2008 12:31:04 PM
Column = Jordi Gel DVB Mixed Bed 50cm x 10cm

Temperature = 45 ° C
Inj. Volume = 200 uL
Flow Rate = 1.2 ml/min

Comments = None

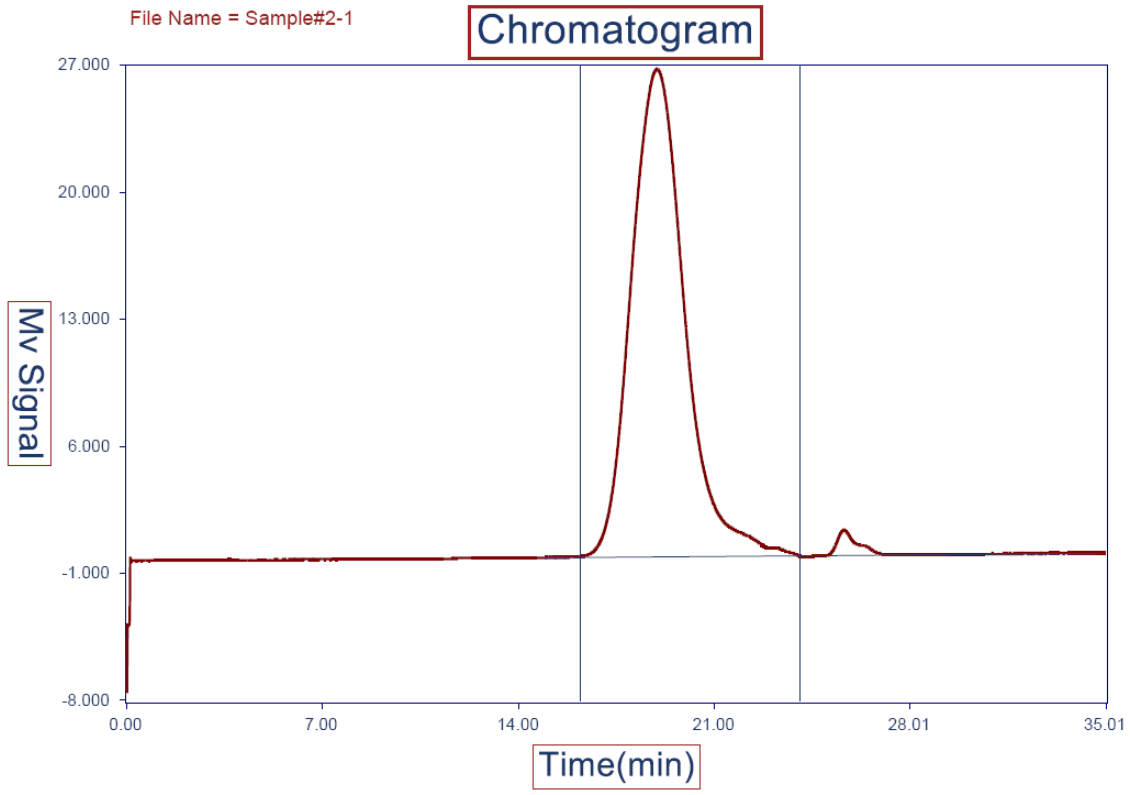
File Name = Sample#2-1
Chromatogram
27.000
20.000
13.000
6.000
-1.000
-8.000
Mv Signal
0.00
7.00
14.00
21.00
28.01
35.01
Time(min)

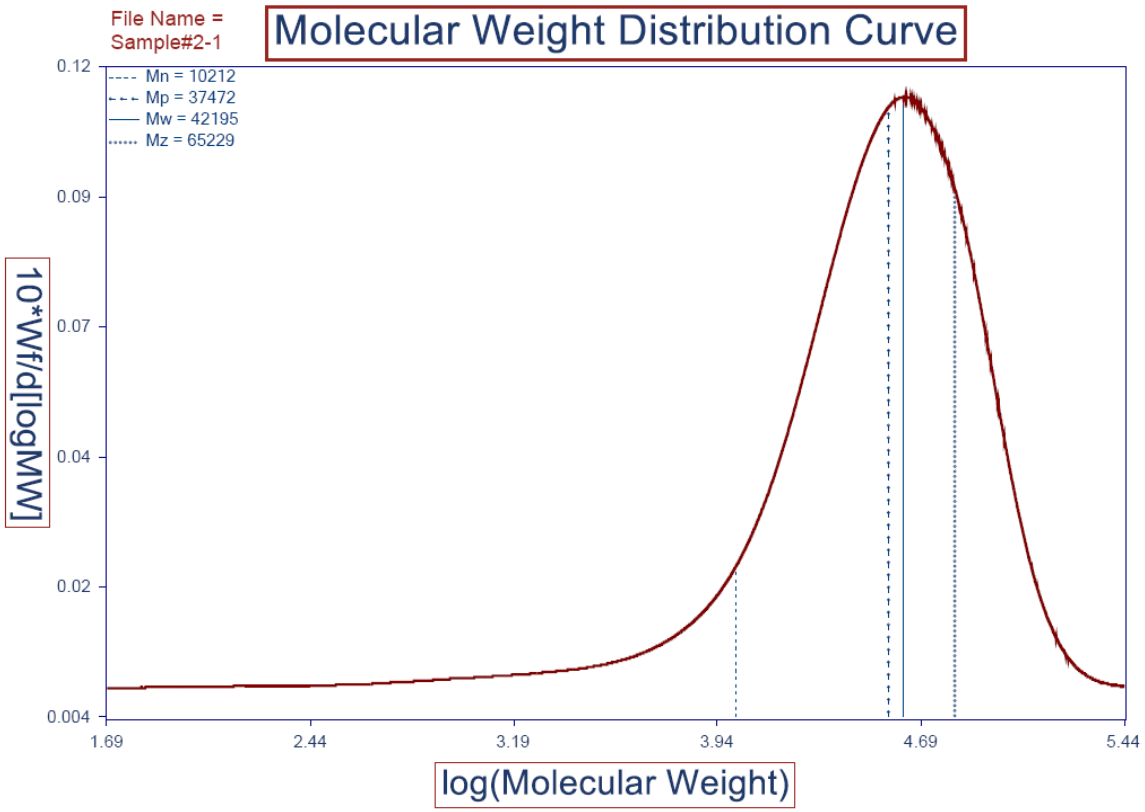
File Name =
Sample#2-1
Molecular Weight Distribution Curve
Mn = 10212
Mp = 37472
Mw = 42195
Mz = 65229
0.12
0.09
0.07
0.04
0.02
0.004
10*Wf/dlogMW]
1.69
2.44
3.19
3.94
4.69
5.44
log(Molecular Weight)

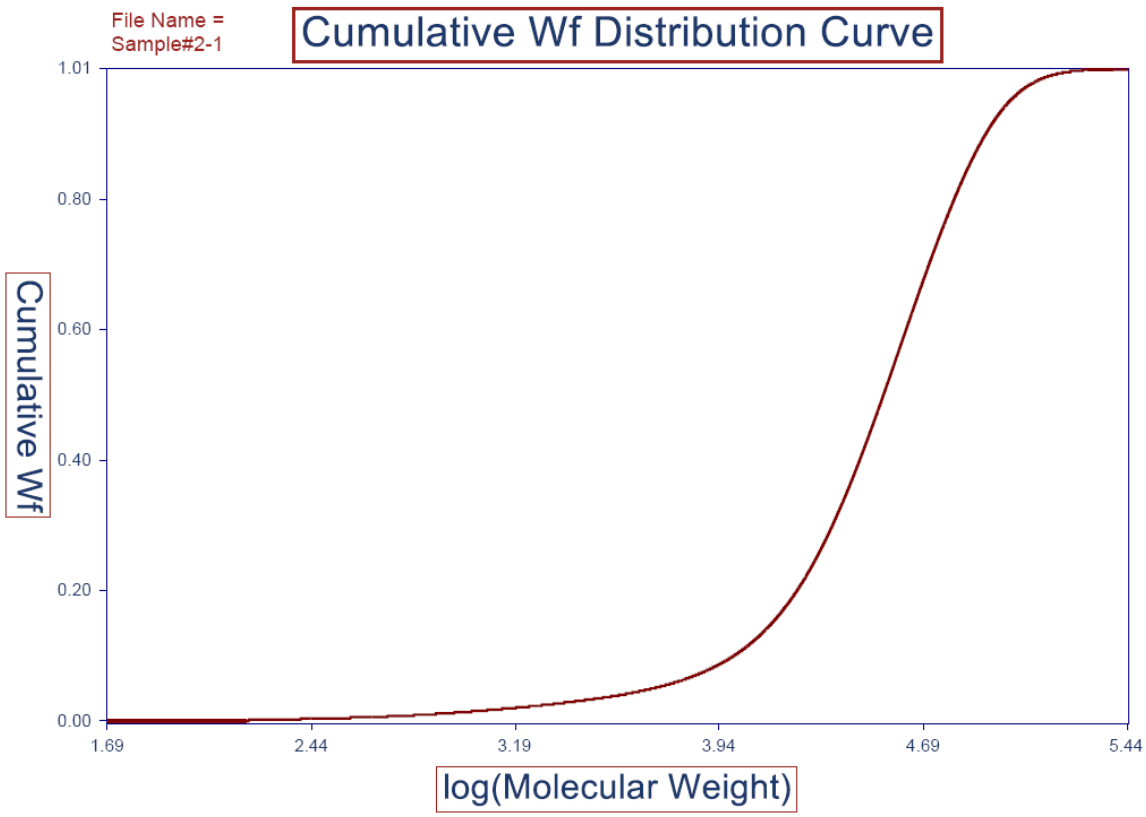

Summary of Molecular Weights

File Name = Sample#2-1.ASC

Sample Name = Unknown

Calibration File Name = UoWaterlooCal010408.ASC

Number Average Molecular Weight (Mn) = 10212

Weight Average Molecular Weight (Mw) = 42195

Z Average Molecular Weight (Mz) = 65229

Peak Maximum Molecular Weight (Mp) = 37472

Polydispersity = 4.13

Peak Area = 35693

Integration Limits =
Left = 19.49
Right = 28.91

Mobile Phase = THF
Detector = Refractive Index
Concentration = 2.5 mg/ml
Run Date = 1/3/2008 1:56:19 PM
Column = Jordi Gel DVB Mixed Bed 50cm x 10cm

Comments = None

Temperature = 45 ° C
Inj. Volume = 200 uL
Flow Rate = 1.2 ml/min

Summary of Molecular Weights

File Name = Sample#2-2

Sample Name = Unknown

Calibration File Name = UoWaterlooCal010408.ASC

Number Average Molecular Weight (Mn) = 9930

Weight Average Molecular Weight (Mw) = 42116

Z Average Molecular Weight (Mz) = 64946

Peak Maximum Molecular Weight (Mp) = 37375

Polydispersity = 4.24

Peak Area = 35741

Integration Limits =

Left = 19.49

Right = 28.91

Mobile Phase = THF

Detector = Refractive Index

Concentration = 2.5 mg/ml

Run Date = 1/3/2008 2:38:56 PM

Column = Jordi Gel DVB Mixed Bed 50cm x 10cm

Comments = None

Temperature = 45 ° C

Inj. Volume = 200 uL

Flow Rate = 1.2 ml/min

Group 52-T1 and 52-T2 Data (Two runs from two samples each)

52-T1: Samples 1 & 2
52-T2: Samples 3 & 4

Avg. Molecular Wt.

Sample ID	Run #	Mn	Avg.	Mw	Avg.	Mz	Avg.	Mw/Mn	Avg.
Sample 1	1	24,393	24,221	51,768	51,526	77,657	77,471	2.12	2.13
	2	24,050		51,283		77,285		2.13	
Sample 2	1	24,784	24,607	51,435	51,702	76,844	77,340	2.08	2.10
	2	24,430		51,969		77,836		2.13	
Sample 3	1	24,651	24,480	53,087	52,508	80,707	80,182	2.15	2.14
	2	24,309		51,930		79,658		2.14	
Sample 4	1	24,570	24,525	52,116	52,156	79,191	79,308	2.12	2.13
	2	24,481		52,196		79,425		2.13	

Relative to polystyrene standards

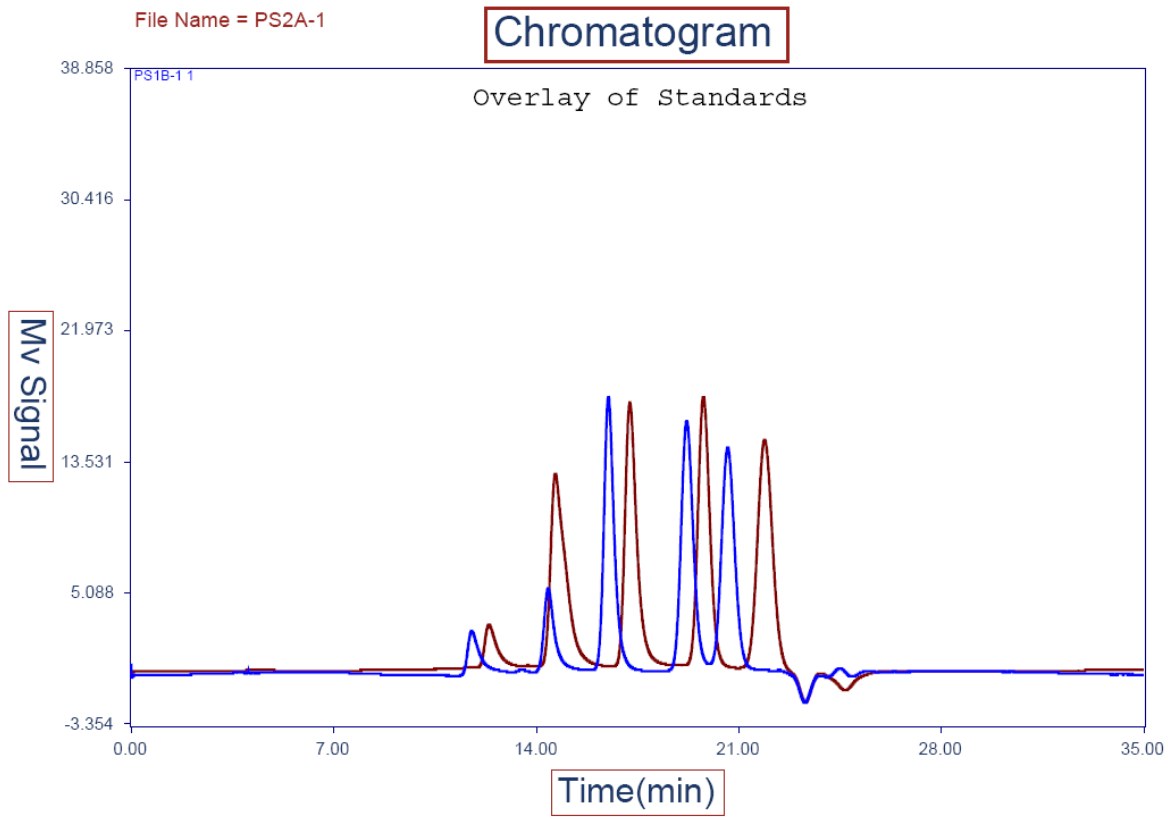
File Name = PS2A-1
Chromatogram
PS1B-1 1
Overlay of Standards
38.858
30.416
21.973
13.531
5.088
-3.354
Mv Signal
0.00
7.00
14.00
21.00
28.00
35.00
Time(min)

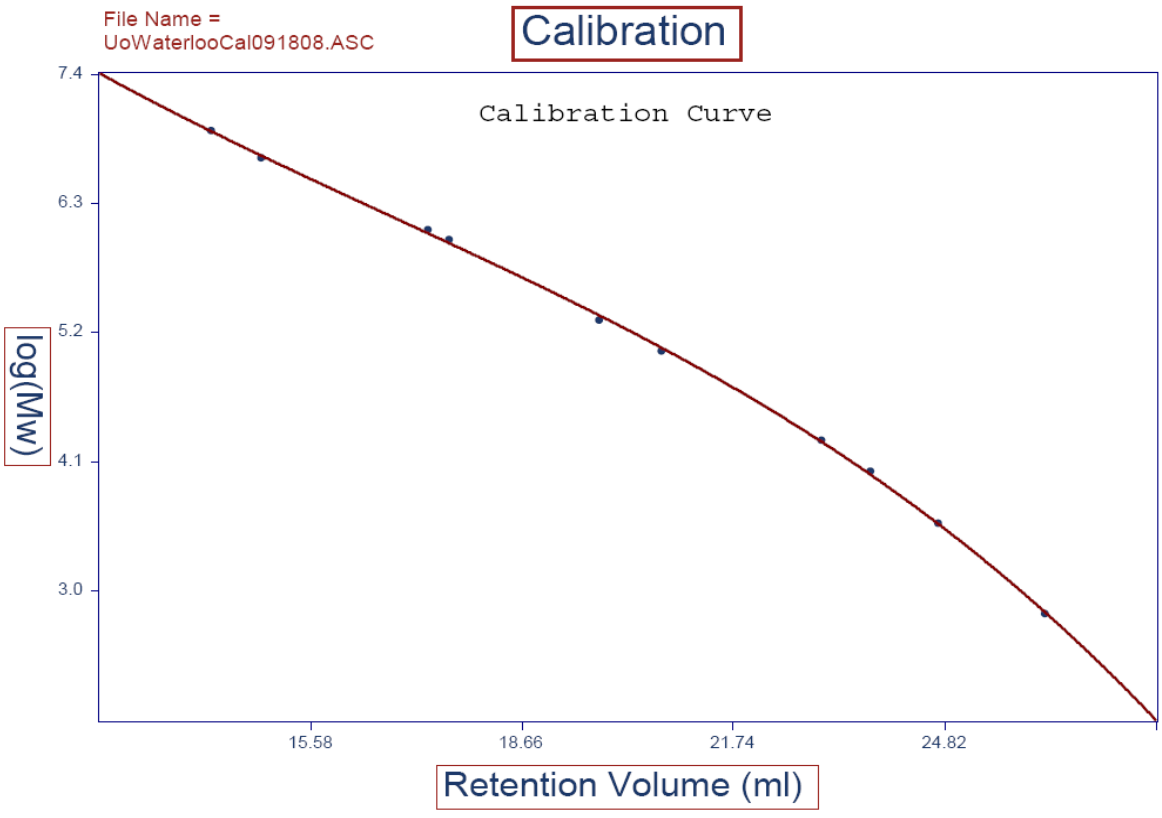
File Name =
UoWaterlooCal091808.ASC
Calibration
Calibration Curve
7.4
6.3
5.2
4.1
3.0
log(Mw)
15.58
18.66
21.74
24.82
Retention Volume (ml)

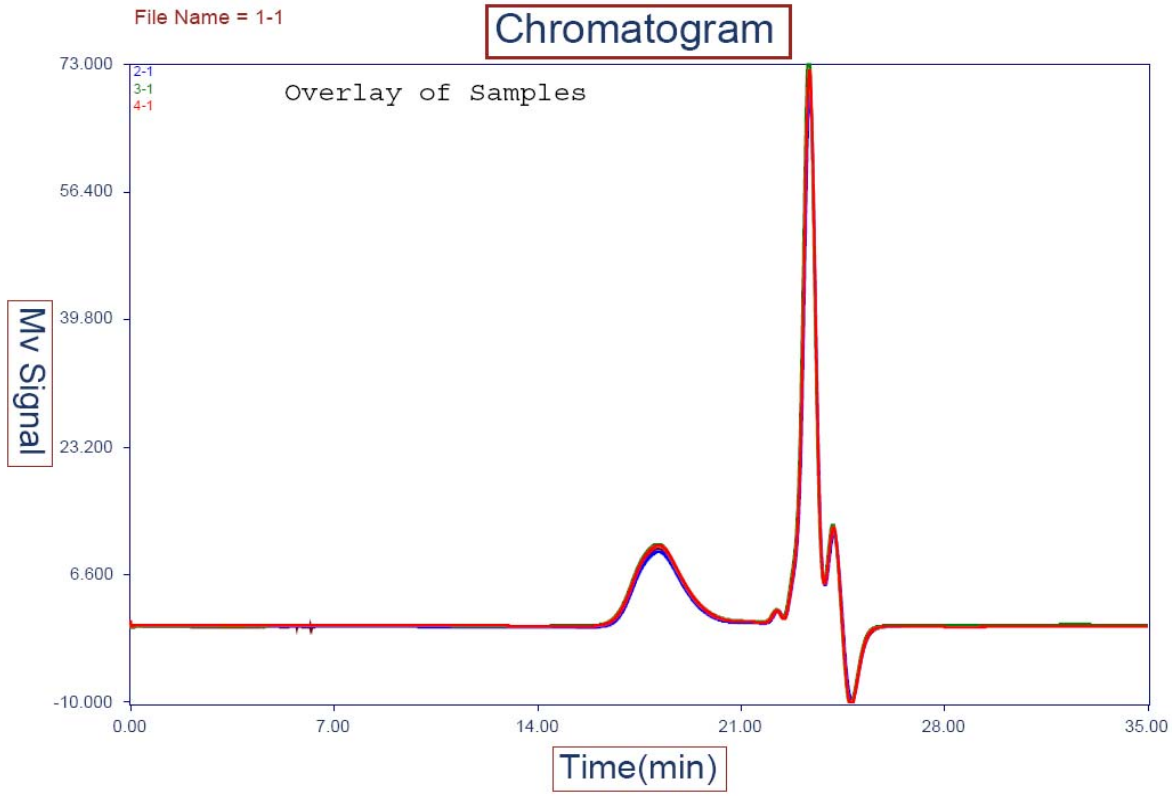
File Name = 1-1
Chromatogram
Overlay of Samples
2-1
3-1
4-1
73.000
56.400
39.800
23.200
6.600
-10.000
Mv Signal
0.00
7.00
14.00
21.00
28.00
35.00
Time(min)

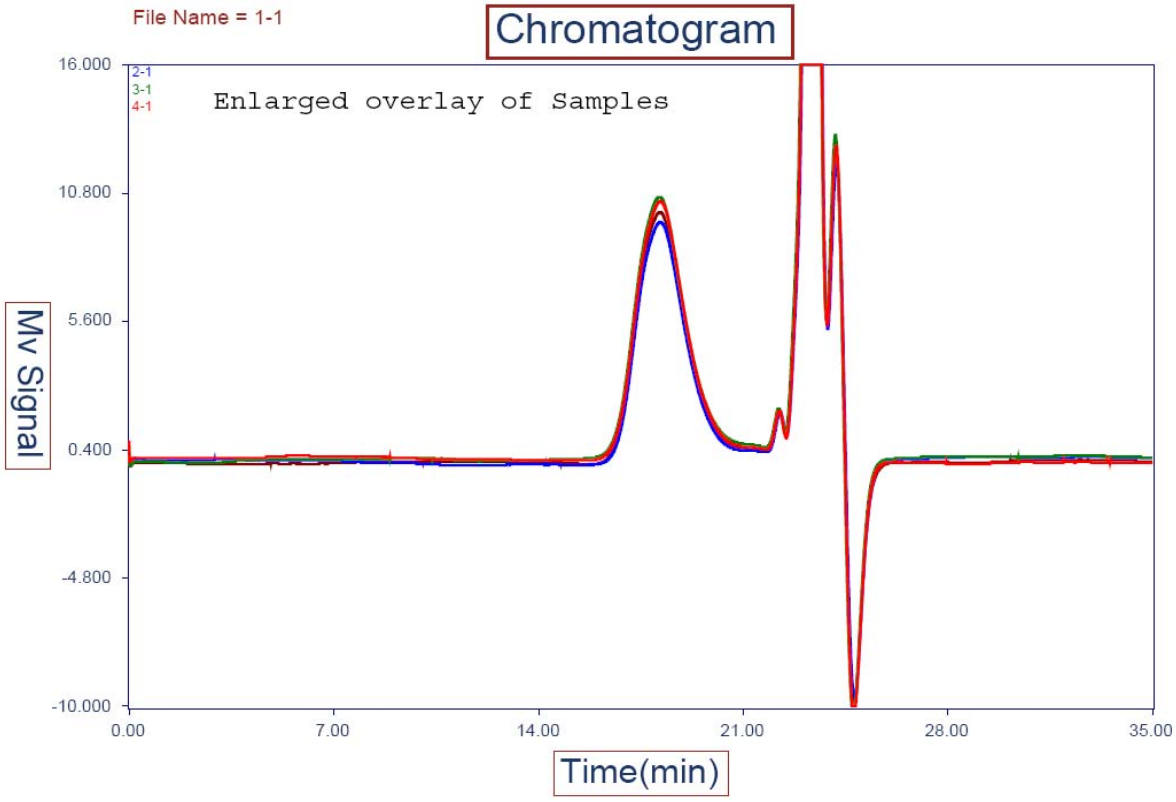
File Name = 1-1
Chromatogram
Enlarged overlay of Samples
2-1
3-1
4-1
16.000
10.800
5.600
0.400
-4.800
-10.000
Mv Signal
0.00
7.00
14.00
21.00
28.00
35.00
Time(min)

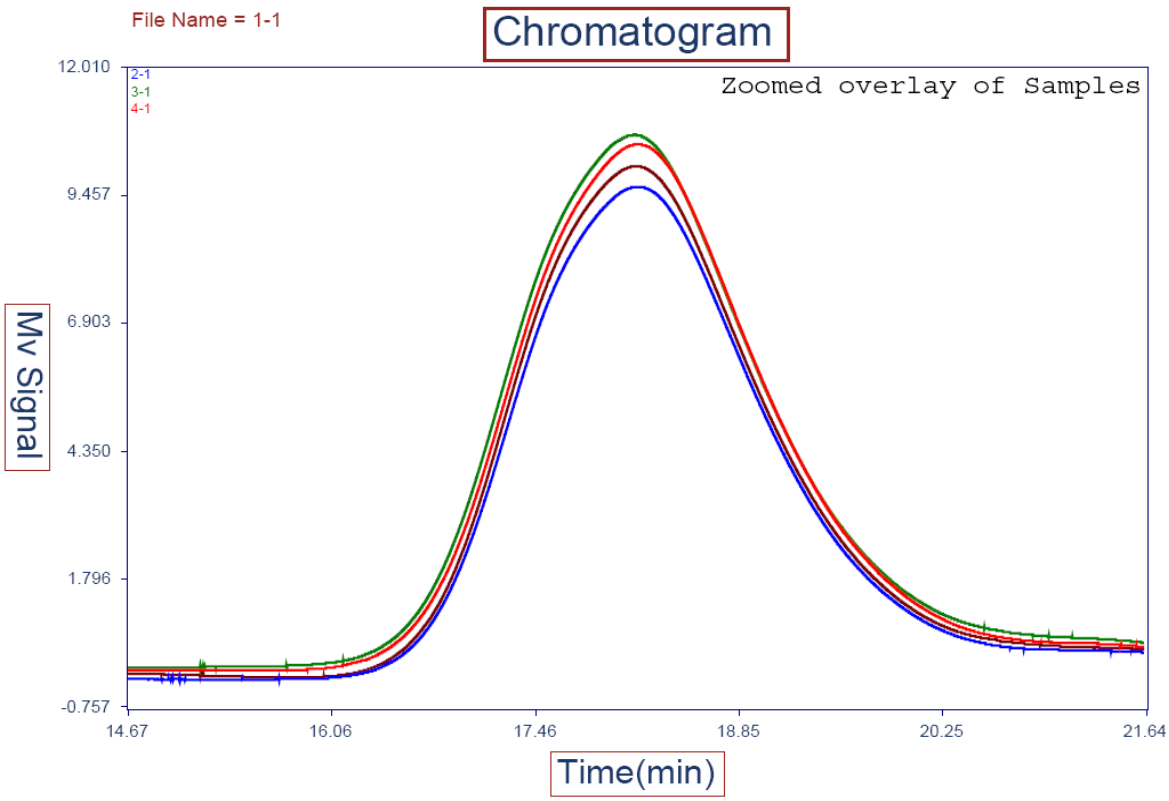
File Name = 1-1
Chromatogram
Zoomed overlay of Samples
2-1
3-1
4-1
12.010
9.457
6.903
4.350
1.796
-0.757
Mv Signal
14.67
16.06
17.46
18.85
20.25
21.64
Time(min)

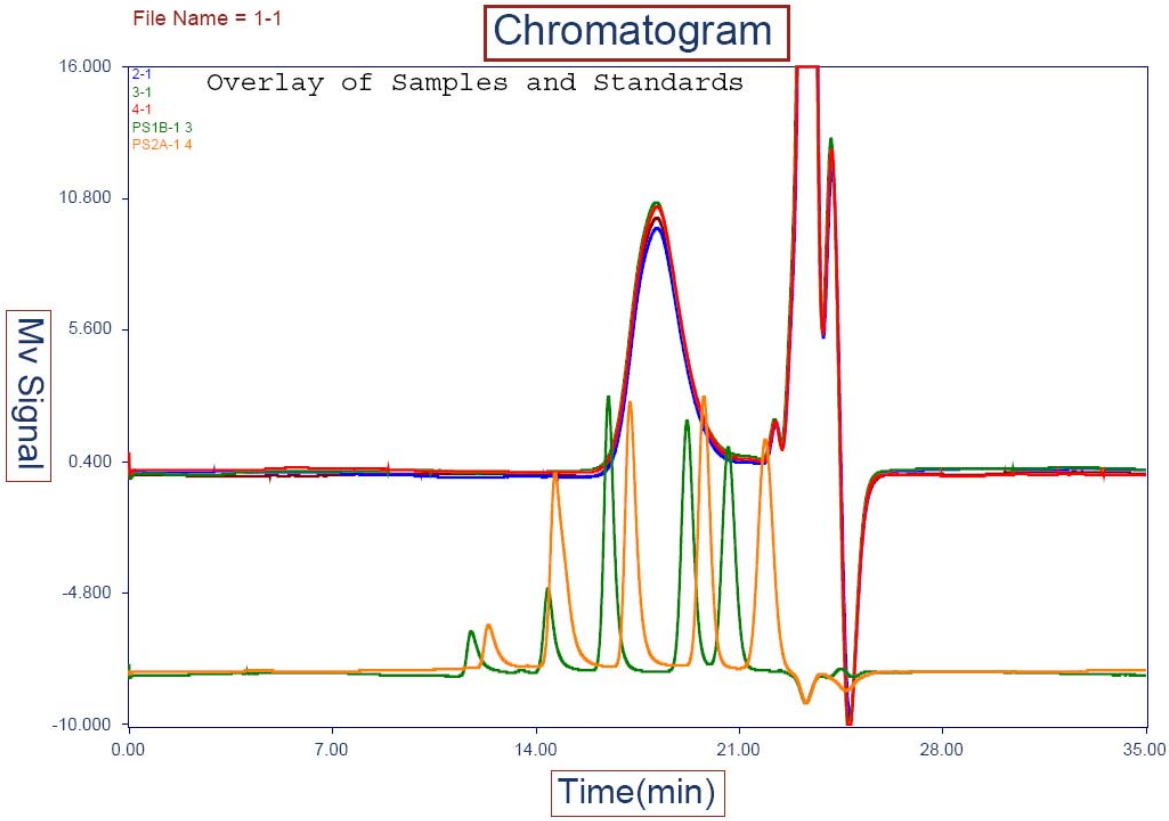
File Name = 1-1
Chromatogram
Overlay of Samples and Standards
2-1
3-1
4-1
PS1B-1 3
PS2A-1 4
16.000
10.800
5.600
0.400
-4.800
-10.000
Mv Signal
0.00
7.00
14.00
21.00
28.00
35.00
Time(min)

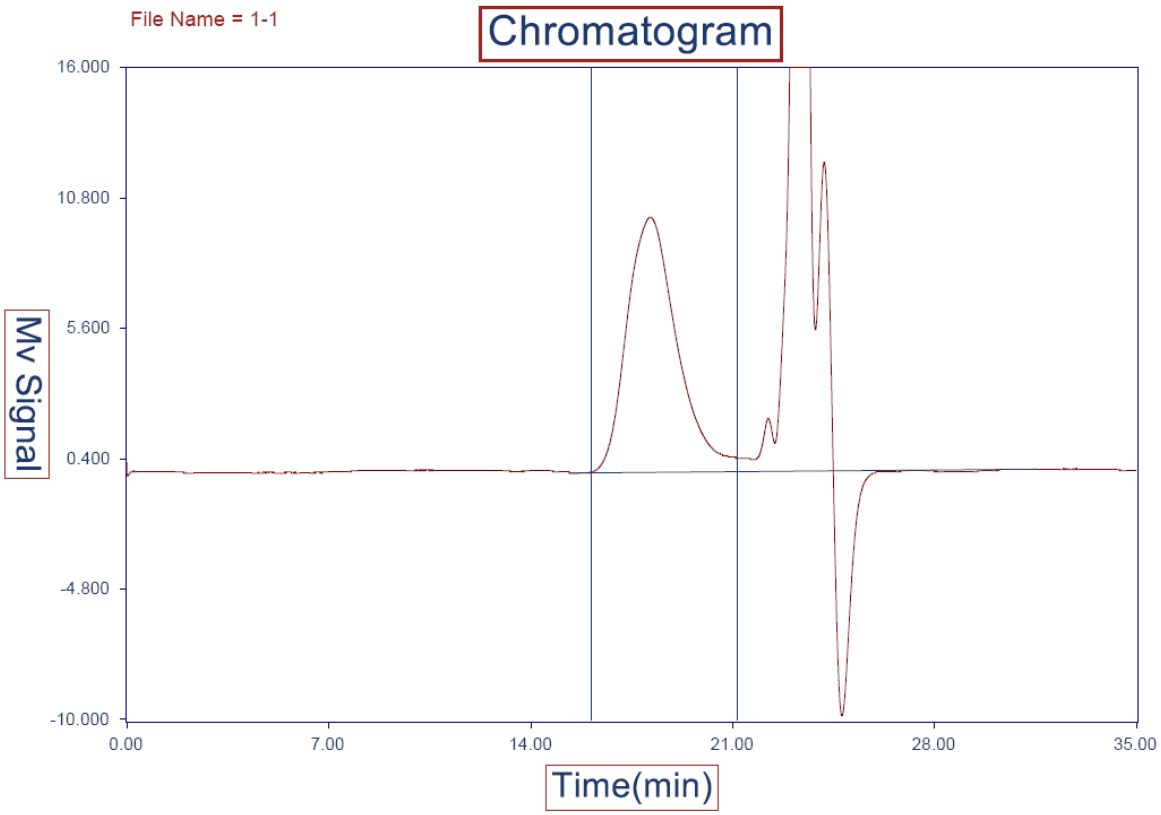
File Name = 1-1
Chromatogram
16.000
10.800
5.600
0.400
-4.800
-10.000
Mv Signal
0.00
7.00
14.00
21.00
28.00
35.00
Time(min)

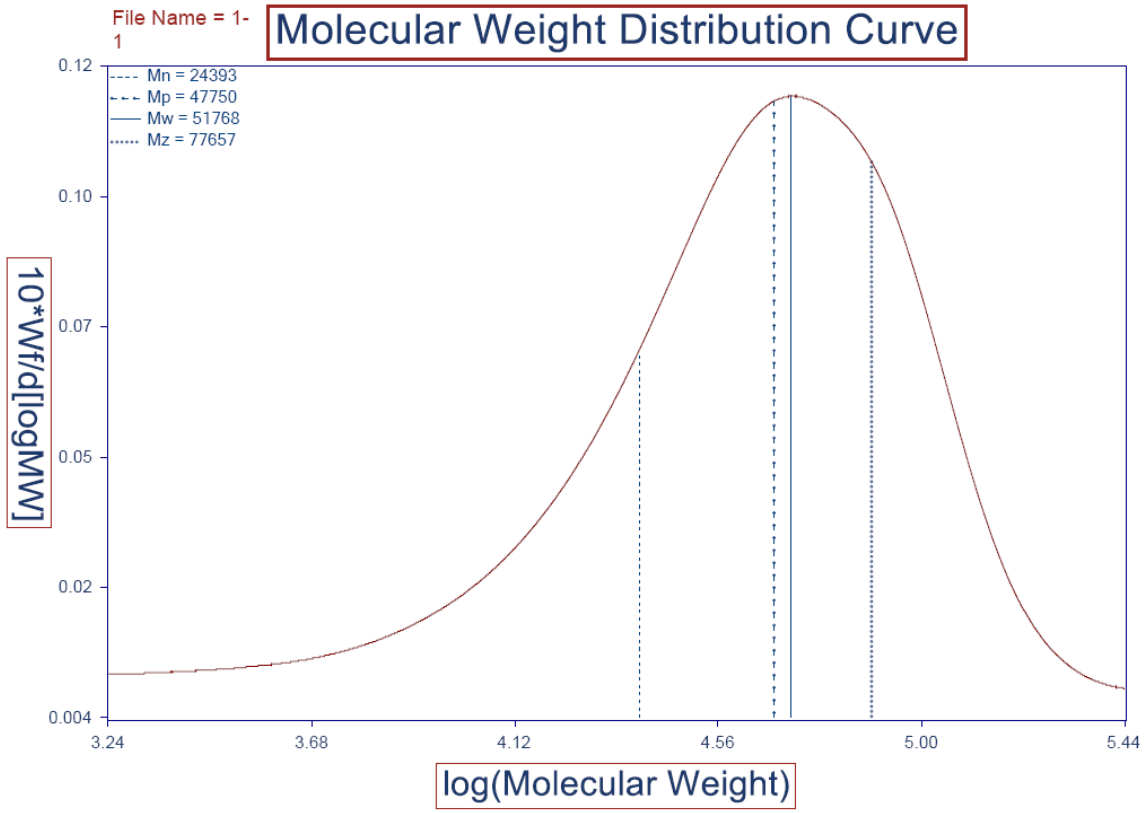
File Name = 1-1
Molecular Weight Distribution Curve
Mn = 24393
Mp = 47750
Mw = 51768
Mz = 77657
0.12
0.10
0.07
0.05
0.02
0.004
10*Wf/d[logMW]
3.24
3.68
4.12
4.56
5.00
5.44
log(Molecular Weight)

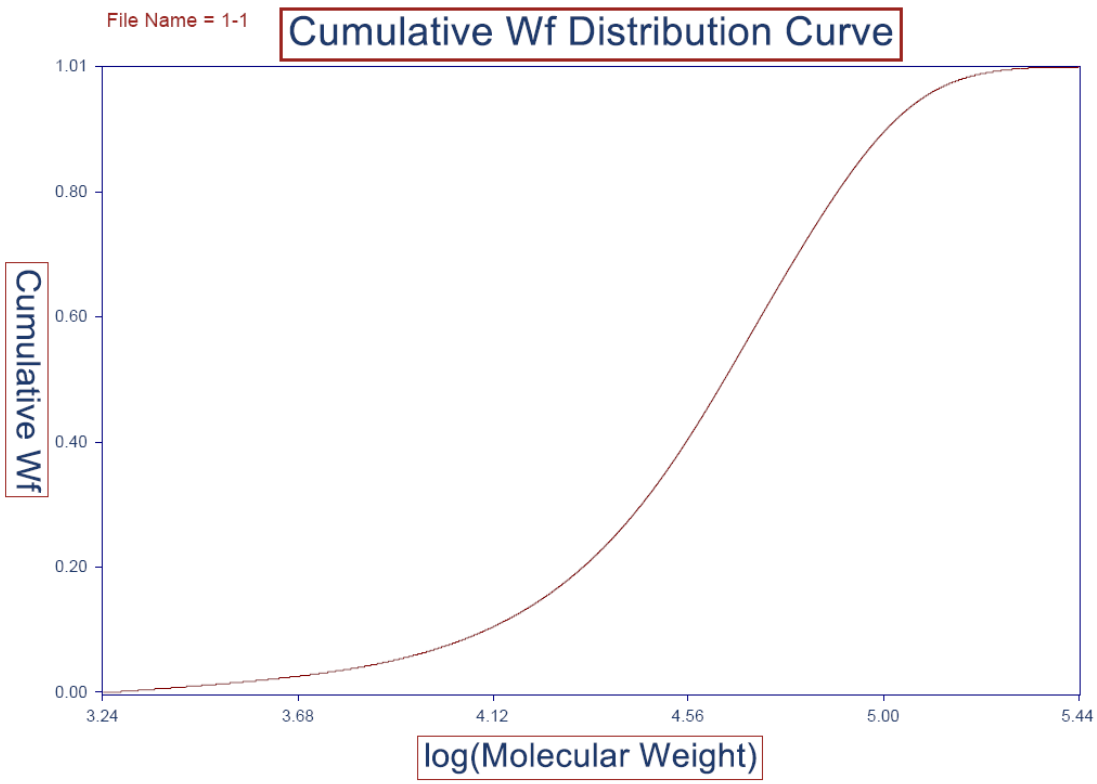

Summary of Molecular Weights

File Name = 1-1.ASC

Sample Name = Sample 1

Calibration File Name = UoWaterlooCal091808.ASC

Number Average Molecular Weight (Mn) = 24393
Weight Average Molecular Weight (Mw) = 51768
Z Average Molecular Weight (Mz) = 77657
Peak Maximum Molecular Weight (Mp) = 47750
Polydispersity = 2.12
Peak Area = 12264

Integration Limits =
Left = 19.32
Right = 25.37

Mobile Phase = Tetrahydrofuran
Detector = Refractive Index
Concentration = 0.625 mg/ml
Run Date = 9/17/2008 3:49:34 PM
Column = Jordi Gel DVB Mixed Bed 50cm x 10cm

Temperature = 45 ° C
Inj. Volume = 200 uL
Flow Rate = 1.2 ml/min

Comments = None

Summary of Molecular Weights

File Name = 1-2

Sample Name = Sample 1

Calibration File Name = UoWaterlooCal091808.ASC

Number Average Molecular Weight (Mn) = 24050
Weight Average Molecular Weight (Mw) = 51283
Z Average Molecular Weight (Mz) = 77285
Peak Maximum Molecular Weight (Mp) = 46790
Polydispersity = 2.13
Peak Area = 12194

Integration Limits =
Left = 19.32
Right = 25.37

Mobile Phase = Tetrahydrofuran
Detector = Refractive Index
Concentration = 0.625 mg/ml
Run Date = 9/17/2008 4:32:12 PM
Column = Jordi Gel DVB Mixed Bed 50cm x 10cm

Temperature = 45 ° C
Inj. Volume = 200 uL
Flow Rate = 1.2 ml/min

Comments = None

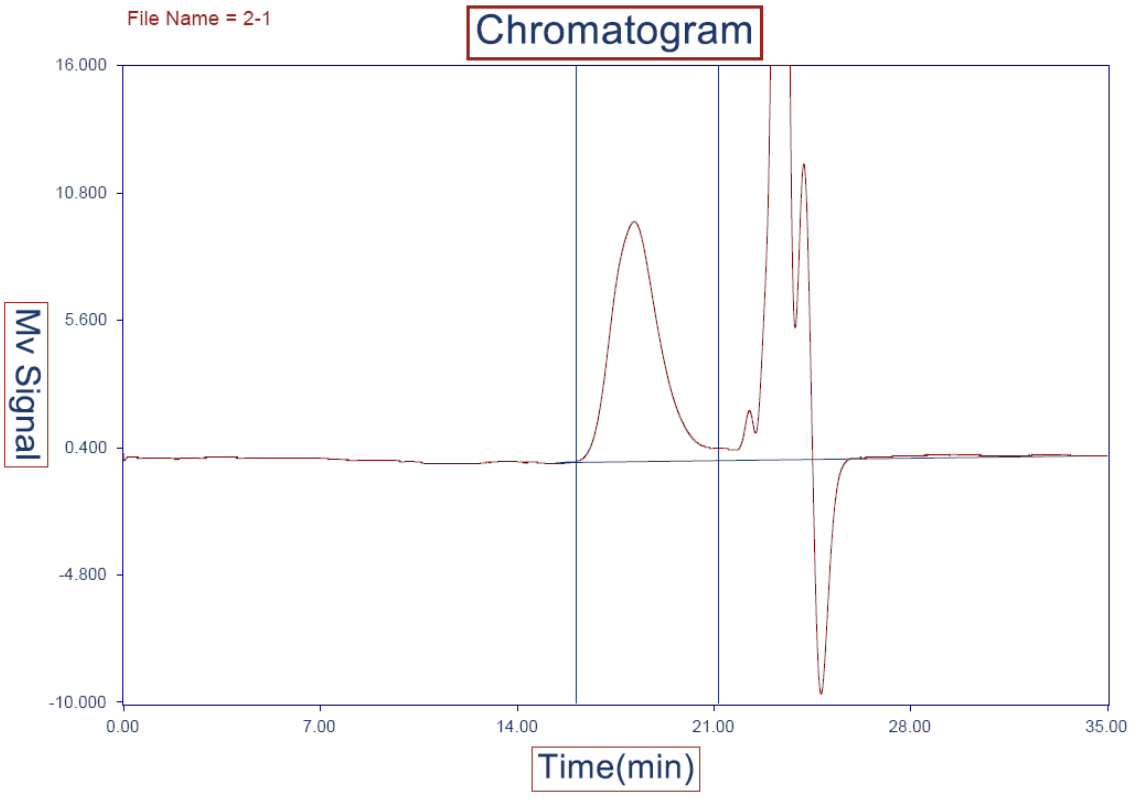

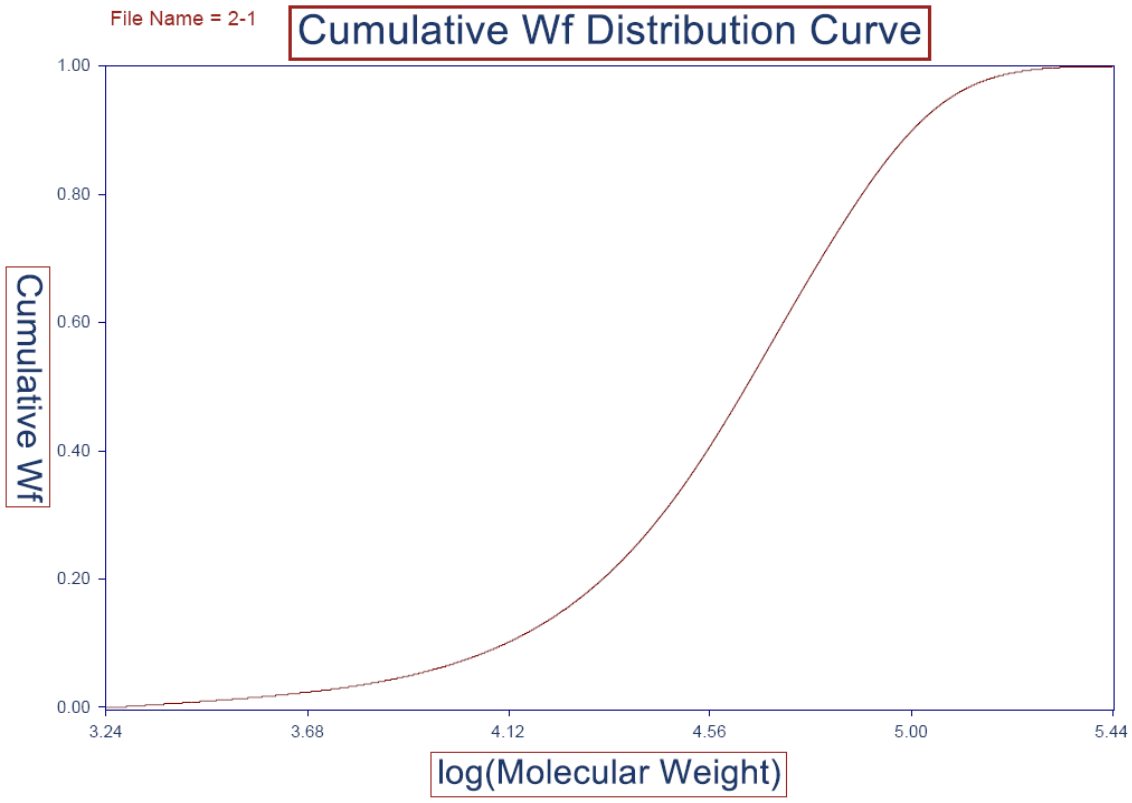
File Name = 2-1
Cumulative Wf Distribution Curve
1.00
0.80
0.60
0.40
0.20
0.00
Cumulative Wf
3.24
3.68
4.12
4.56
5.00
5.44
log(Molecular Weight)

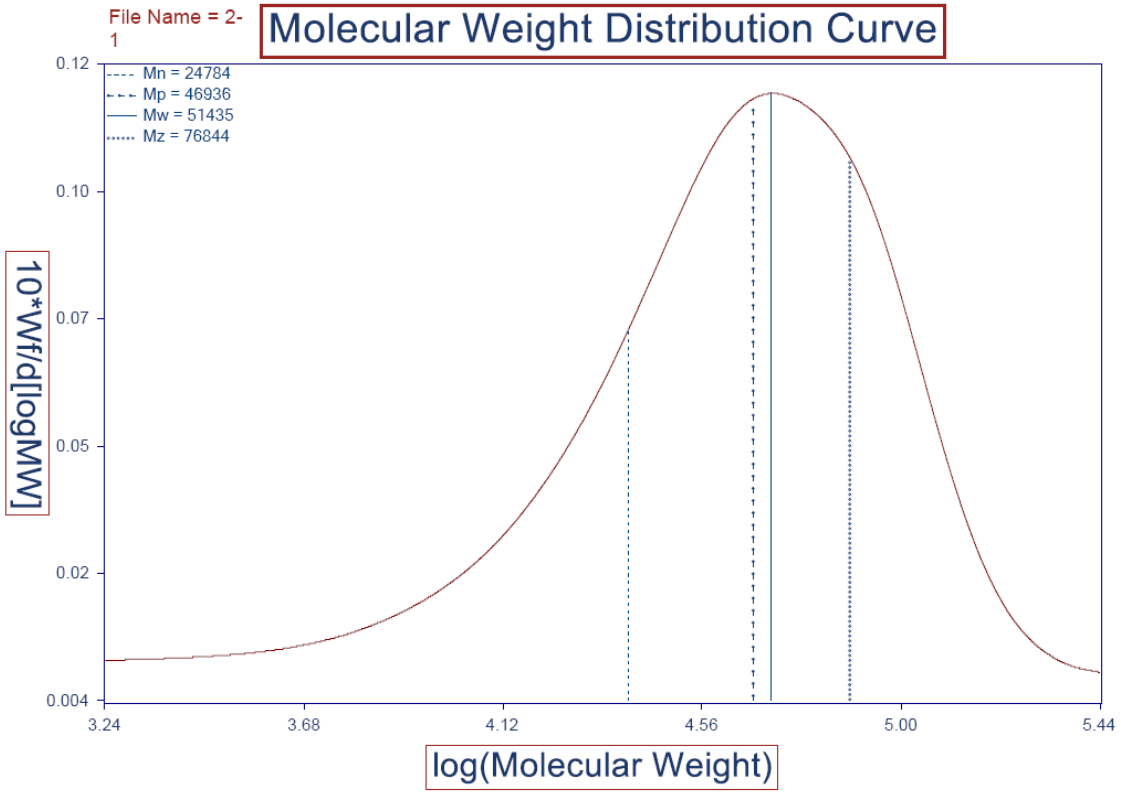
File Name = 2-1
Molecular Weight Distribution Curve
Mn = 24784
Mp = 46936
Mw = 51435
Mz = 76844
0.12
0.10
0.07
0.05
0.02
0.004
10*Wf/d[logMW]
3.24
3.68
4.12
4.56
5.00
5.44
log(Molecular Weight)

Summary of Molecular Weights

File Name = 2-1.ASC

Sample Name = Sample 2

Calibration File Name = UoWaterlooCal091808.ASC

Number Average Molecular Weight (Mn) = 24784
Weight Average Molecular Weight (Mw) = 51435
Z Average Molecular Weight (Mz) = 76844
Peak Maximum Molecular Weight (Mp) = 46936
Polydispersity = 2.08
Peak Area = 11709

Integration Limits =
Left = 19.32
Right = 25.37

Mobile Phase = Tetrahydrofuran
Detector = Refractive Index
Concentration = 0.625 mg/ml
Run Date = 9/17/2008 5:57:27 PM
Column = Jordi Gel DVB Mixed Bed 50cm x 10cm

Temperature = 45 ° C
Inj. Volume = 200 uL
Flow Rate = 1.2 ml/min

Comments = None

Summary of Molecular Weights

File Name = 2-2

Sample Name = Sample 2

Calibration File Name = UoWaterlooCal091808.ASC

Number Average Molecular Weight (Mn) = 24430
Weight Average Molecular Weight (Mw) = 51969
Z Average Molecular Weight (Mz) = 77836
Peak Maximum Molecular Weight (Mp) = 47601
Polydispersity = 2.13
Peak Area = 11922

Integration Limits =
Left = 19.32
Right = 25.37

Mobile Phase = Tetrahydrofuran
Detector = Refractive Index
Concentration = 0.625 mg/ml
Run Date = 9/17/2008 6:40:04 PM
Column = Jordi Gel DVB Mixed Bed 50cm x 10cm

Temperature = 45 ° C
Inj. Volume = 200 uL
Flow Rate = 1.2 ml/min

Comments = None

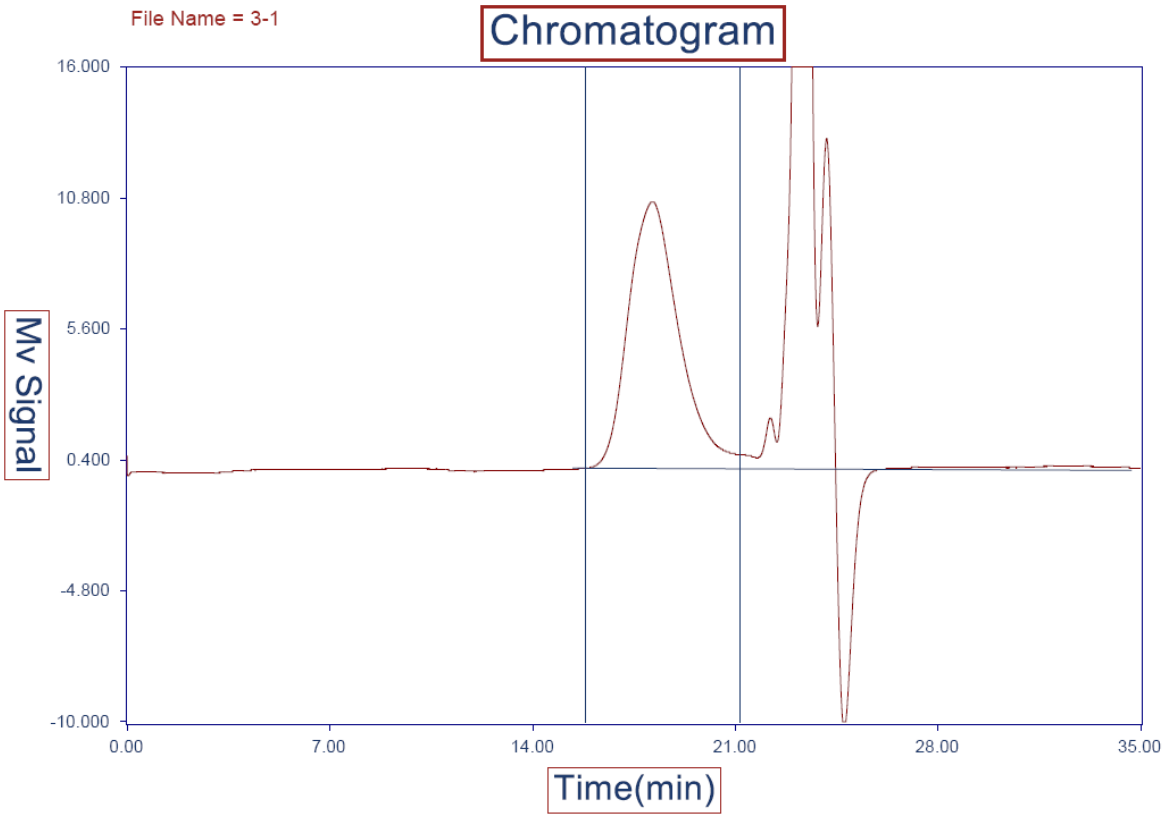
File Name = 3-1
Chromatogram
16.000
10.800
5.600
0.400
-4.800
-10.000
Mv Signal
0.00
7.00
14.00
21.00
28.00
35.00
Time(min)

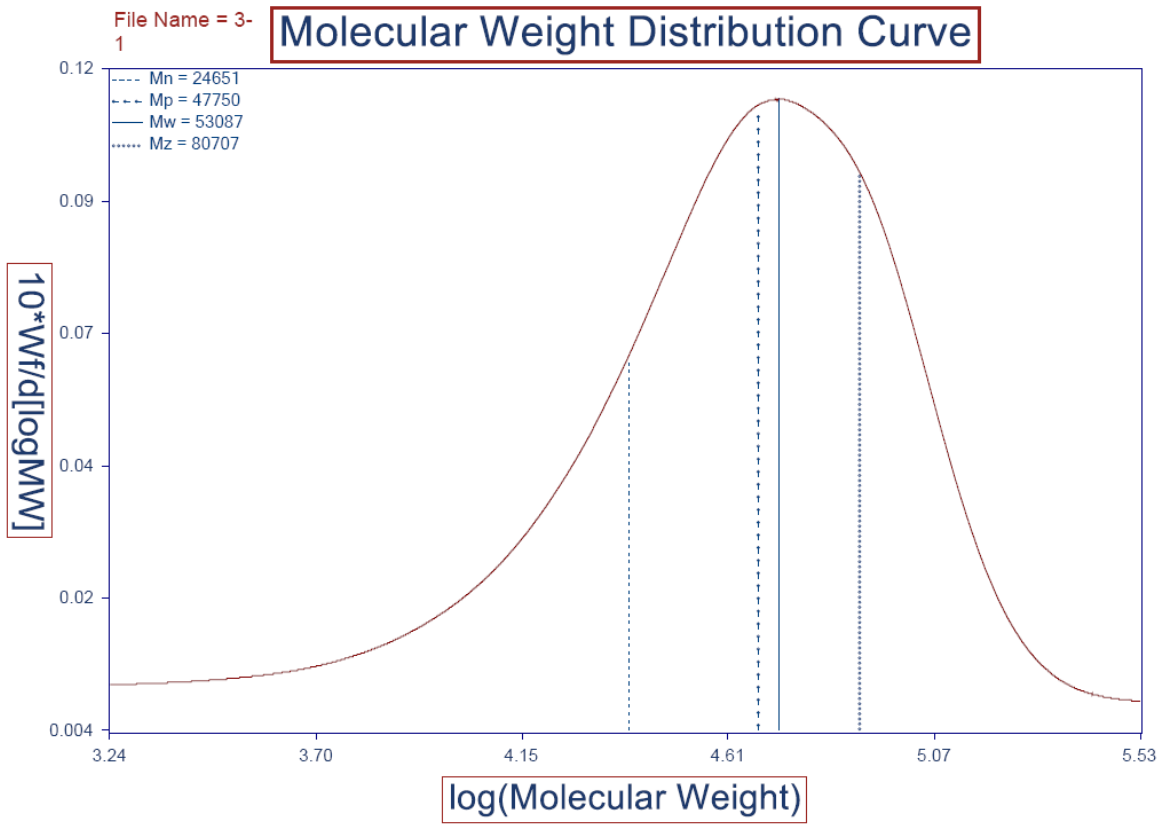
File Name = 3-1
Molecular Weight Distribution Curve
Mn = 24651
Mp = 47750
Mw = 53087
Mz = 80707
0.12
0.09
0.07
0.04
0.02
0.004
10*Wf/d[logMW]
3.24
3.70
4.15
4.61
5.07
5.53
log(Molecular Weight)

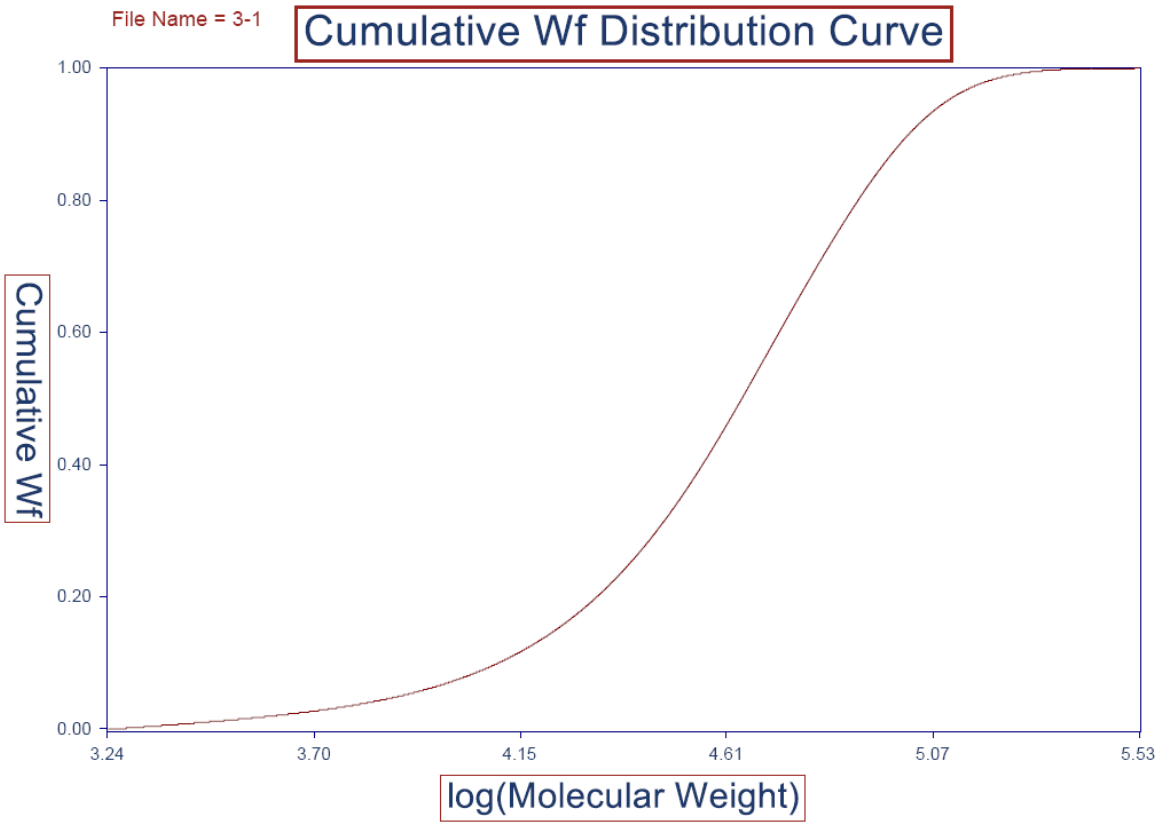

Summary of Molecular Weights

File Name = 3-1.ASC

Sample Name = Sample 3

Calibration File Name = UoWaterlooCal091808.ASC

Number Average Molecular Weight (Mn) = 24651
Weight Average Molecular Weight (Mw) = 53087
Z Average Molecular Weight (Mz) = 80707
Peak Maximum Molecular Weight (Mp) = 47750
Polydispersity = 2.15
Peak Area = 12927

Integration Limits =
Left = 19.00
Right = 25.37

Mobile Phase = Tetrahydrofuran
Detector = Refractive Index
Concentration = 0.625 mg/ml
Run Date = 9/17/2008 8:05:19 PM
Column = Jordi Gel DVB Mixed Bed 50cm x 10cm

Temperature = 45 ° C
Inj. Volume = 200 uL
Flow Rate = 1.2 ml/min

Comments = None

Summary of Molecular Weights

File Name = 3-2

Sample Name = Sample 3

Calibration File Name = UoWaterlooCal091808.ASC

Number Average Molecular Weight (Mn) = 24309
Weight Average Molecular Weight (Mw) = 51930
Z Average Molecular Weight (Mz) = 79658
Peak Maximum Molecular Weight (Mp) = 46644
Polydispersity = 2.14
Peak Area = 12770

Integration Limits =
Left = 19.00
Right = 25.37

Mobile Phase = Tetrahydrofuran
Detector = Refractive Index
Concentration = 0.625 mg/ml
Run Date = 9/17/2008 8:47:56 PM
Column = Jordi Gel DVB Mixed Bed 50cm x 10cm

Temperature = 45 ° C
Inj. Volume = 200 uL
Flow Rate = 1.2 ml/min

Comments = None

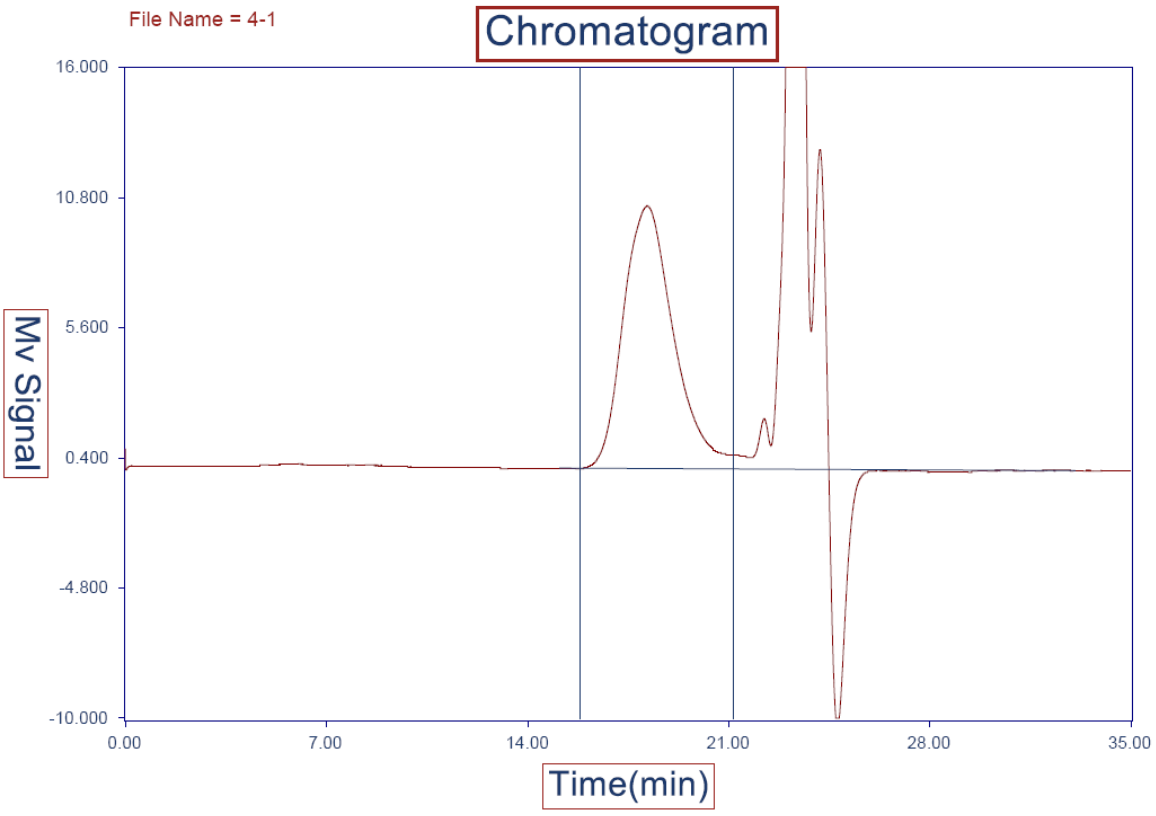

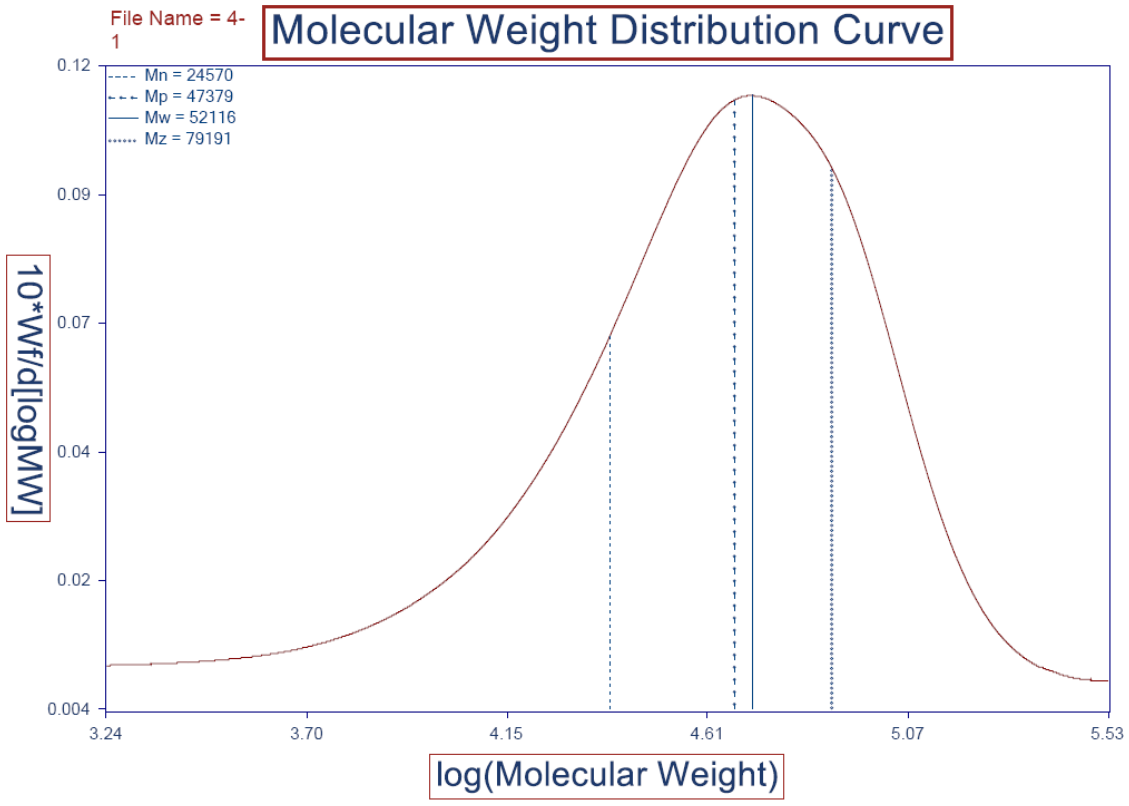
File Name = 4-1
Molecular Weight Distribution Curve
Mn = 24570
Mp = 47379
Mw = 52116
Mz = 79191
10*Wf/d[logMW]
0.12
0.09
0.07
0.04
0.02
0.004
3.24
3.70
4.15
4.61
5.07
5.53
log(Molecular Weight)

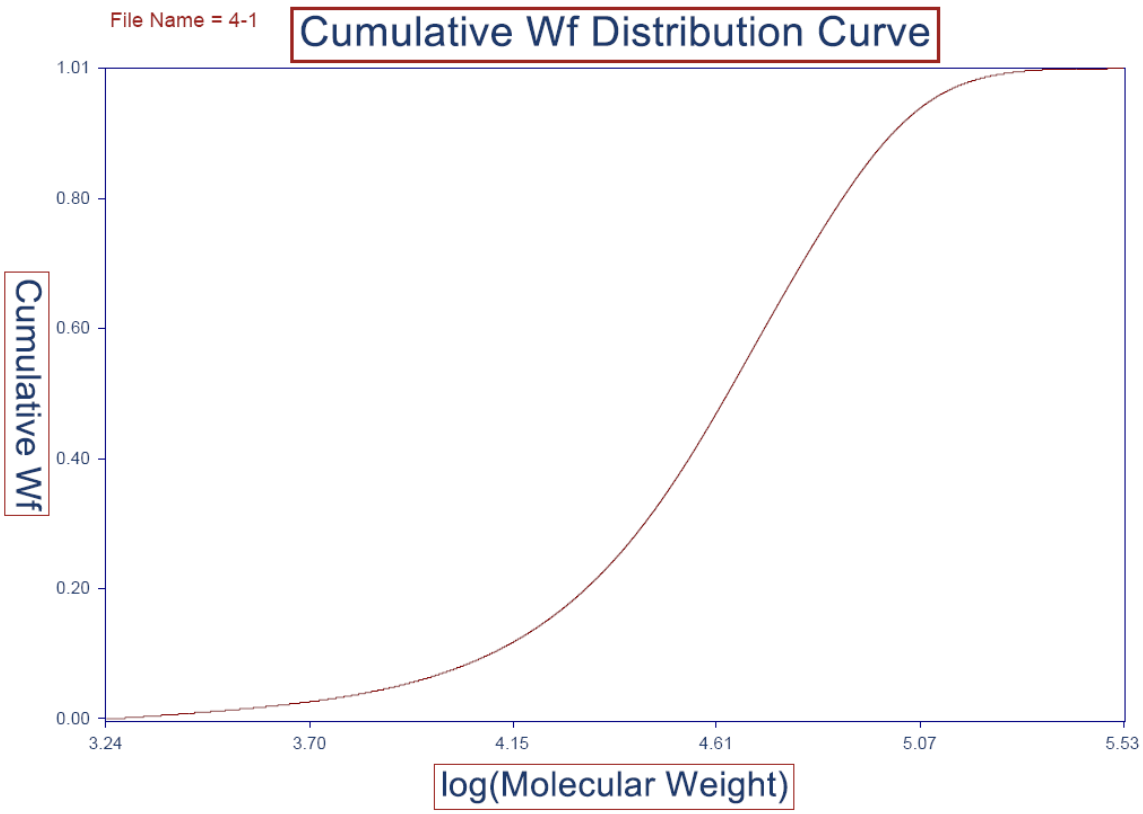
File Name = 4-1
Cumulative Wf Distribution Curve
Cumulative Wf
1.01
0.80
0.60
0.40
0.20
0.00
3.24
3.70
4.15
4.61
5.07
5.53
log(Molecular Weight)

Summary of Molecular Weights

File Name = 4-1.ASC

Sample Name = Sample 4

Calibration File Name = UoWaterlooCal091808.ASC

Number Average Molecular Weight (Mn) = 24570
Weight Average Molecular Weight (Mw) = 52116
Z Average Molecular Weight (Mz) = 79191
Peak Maximum Molecular Weight (Mp) = 47379
Polydispersity = 2.12
Peak Area = 12766

Integration Limits =
Left = 19.00
Right = 25.37

Mobile Phase = Tetrahydrofuran
Detector = Refractive Index
Concentration = 0.625 mg/ml
Run Date = 9/17/2008 10:13:11 PM
Column = Jordi Gel DVB Mixed Bed 50cm x 10cm

Temperature = 45 ° C
Inj. Volume = 200 uL
Flow Rate = 1.2 ml/min

Comments = None

Summary of Molecular Weights

File Name = 4-2

Sample Name = Sample 4

Calibration File Name = UoWaterlooCal091808.ASC

Number Average Molecular Weight (Mn) = 24481
Weight Average Molecular Weight (Mw) = 52196
Z Average Molecular Weight (Mz) = 79425
Peak Maximum Molecular Weight (Mp) = 47010
Polydispersity = 2.13
Peak Area = 12873

Integration Limits =
Left = 19.00
Right = 25.37

Mobile Phase = Tetrahydrofuran
Detector = Refractive Index
Concentration = 0.625 mg/ml
Run Date = 9/17/2008 10:55:48 PM
Column = Jordi Gel DVB Mixed Bed 50cm x 10cm

Temperature = 45 ° C
Inj. Volume = 200 uL
Flow Rate = 1.2 ml/min

Comments = None

APPENDIX C:

DSC Scans

DSC Scan for Specimen 42-T1-01 Tested at 10°C/min

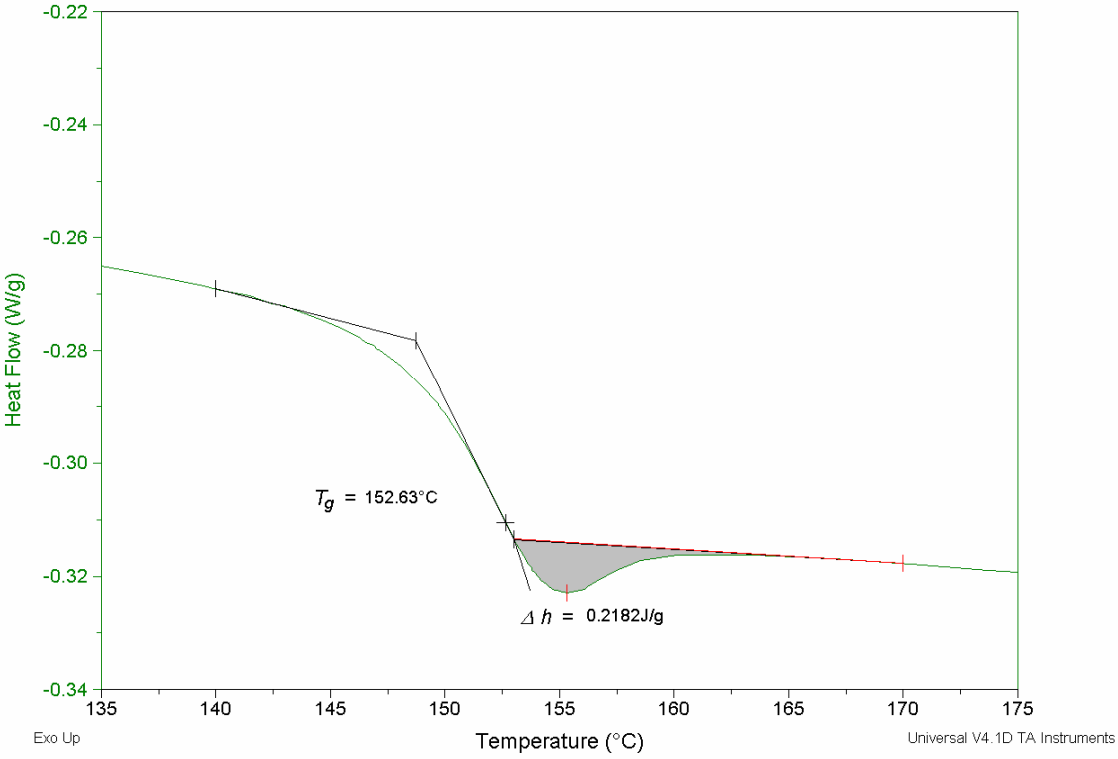

DSC Scan for Specimen 42-T1-02 Tested at 10°C/min

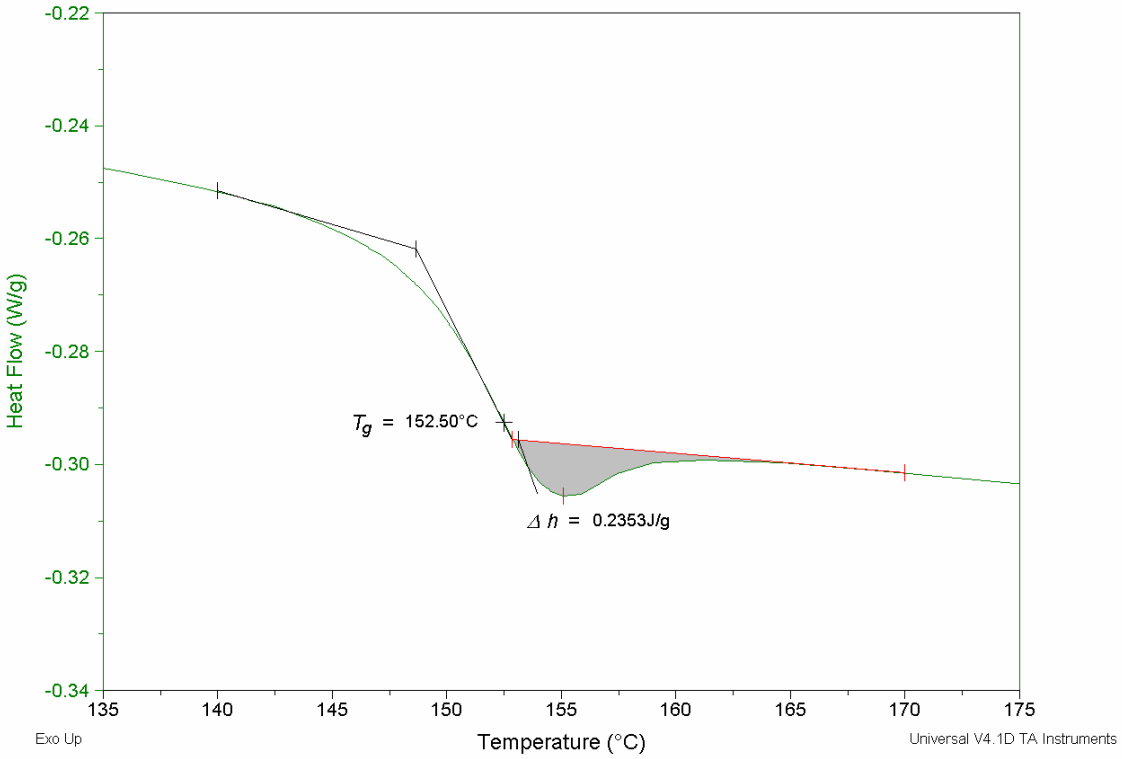

DSC Scan for Specimen 42-T1-03 Tested at 10°C/min

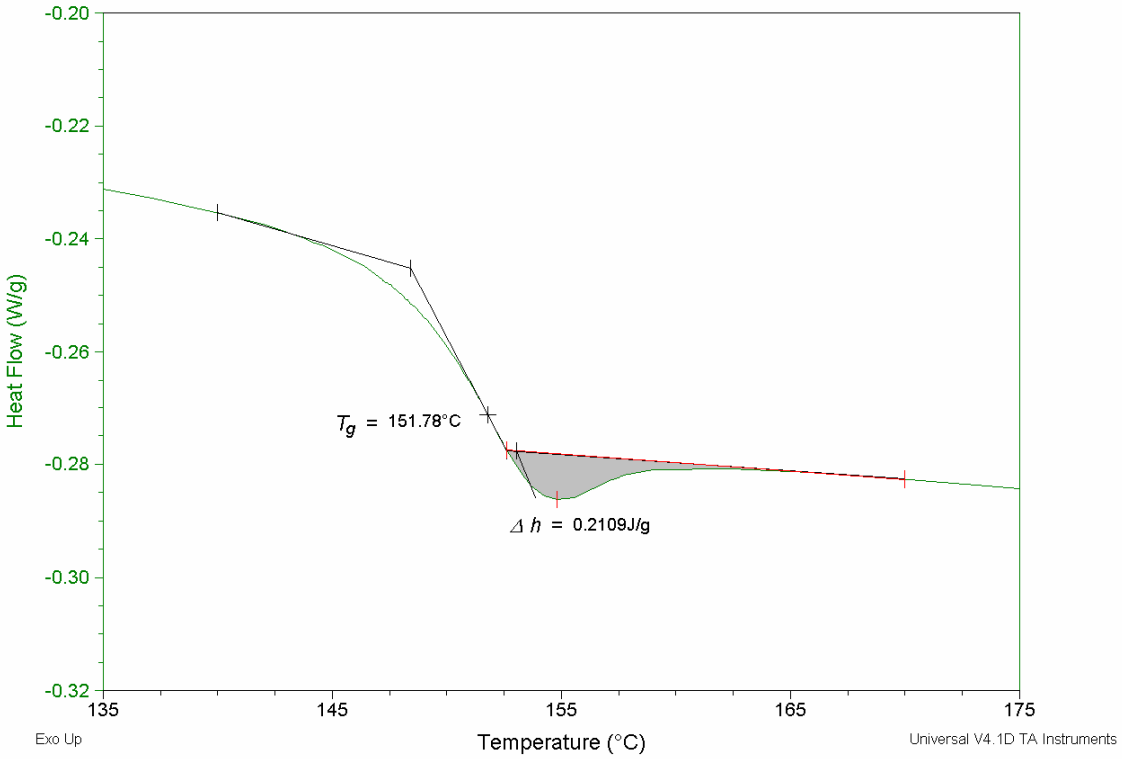

DSC Scan for Specimen 42-T1-04 Tested at 10°C/min

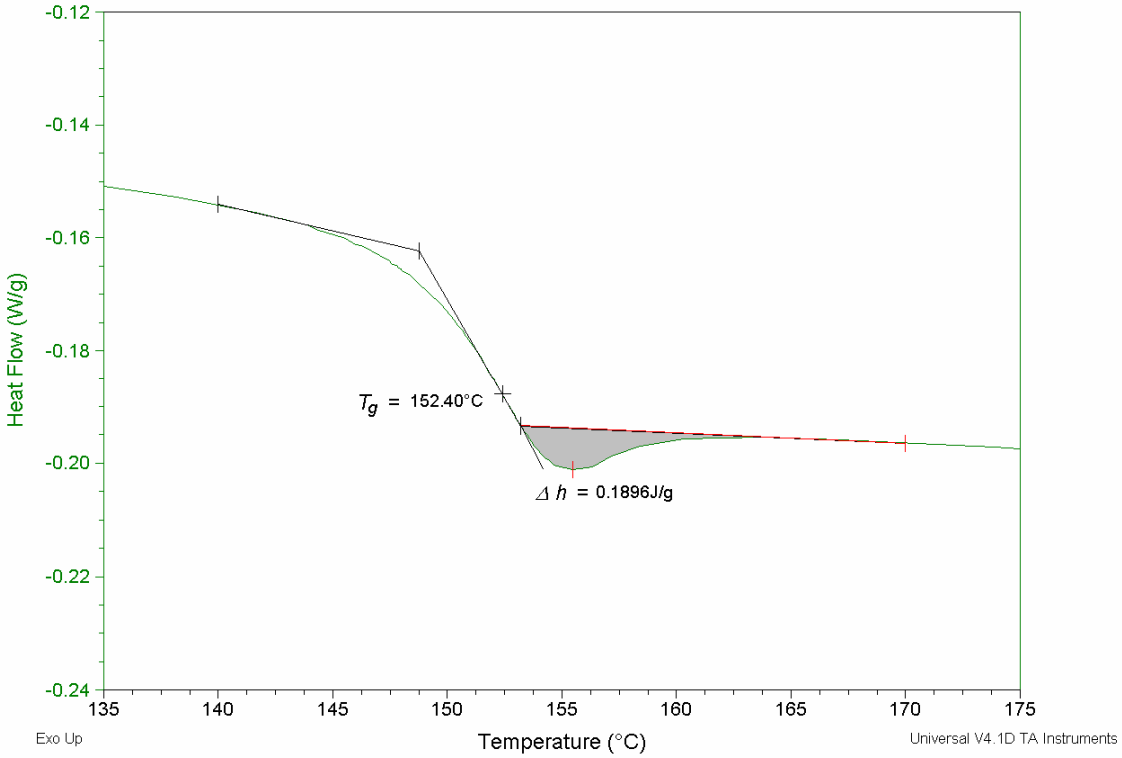

DSC Scan for Specimen 52-T1-01 Tested at 10°C/min

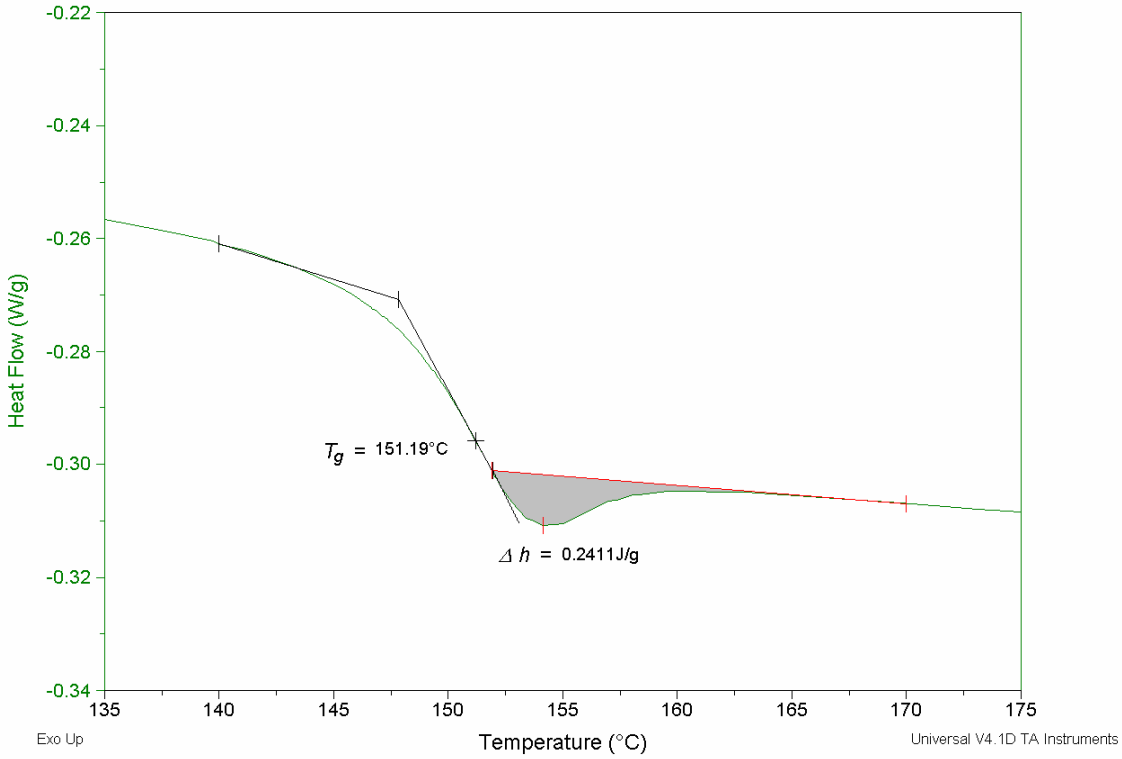

DSC Scan for Specimen 52-T1-02 Tested at 10°C/min

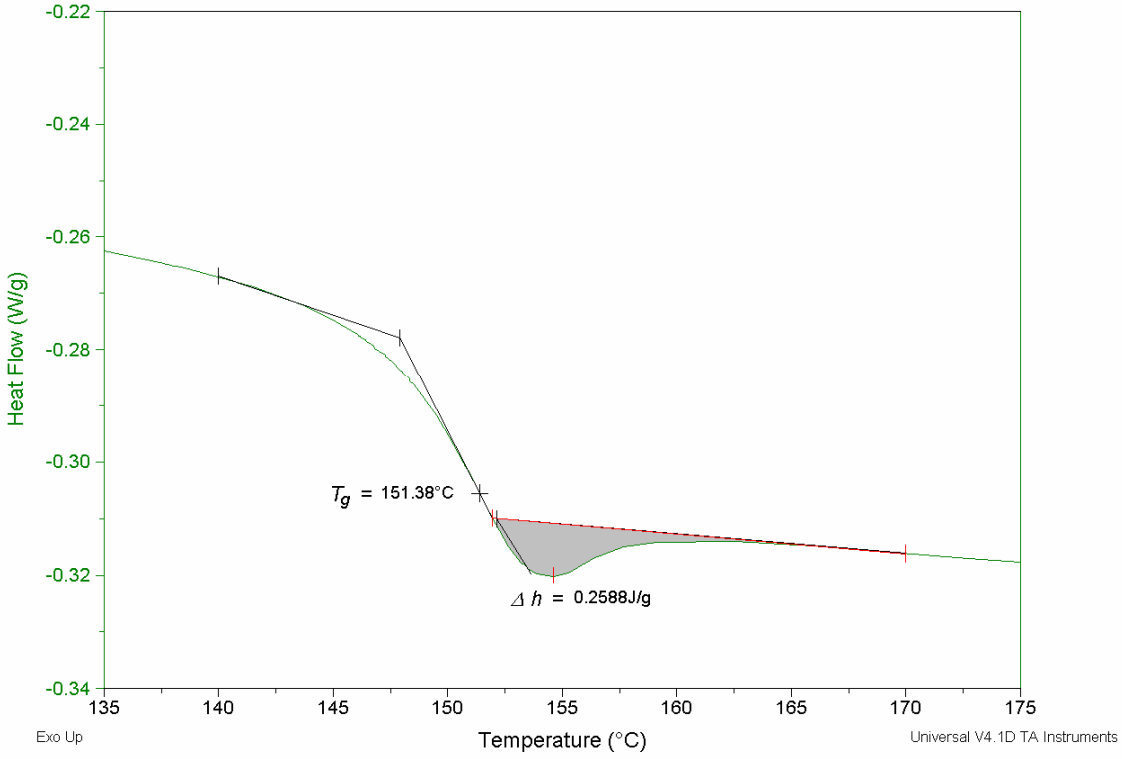

DSC Scan for Specimen 52-T1-03 Tested at 10°C/min

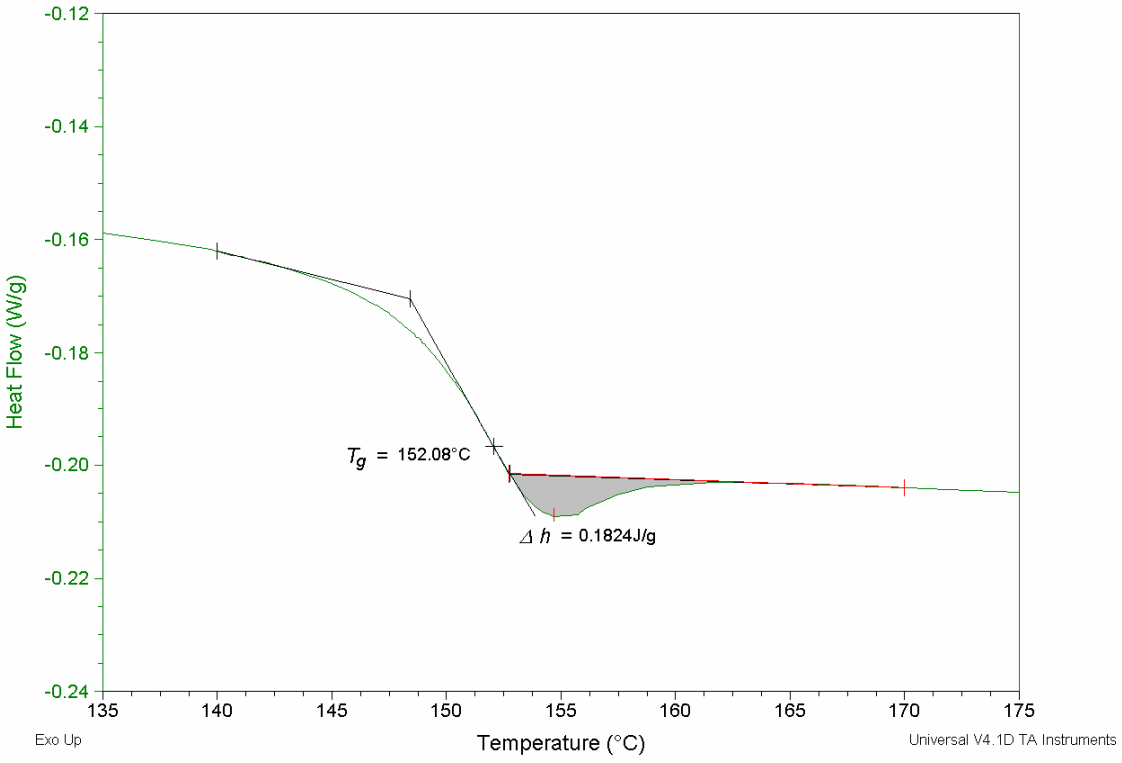

DSC Scan for Specimen 52-T1-04 Tested at 10°C/min

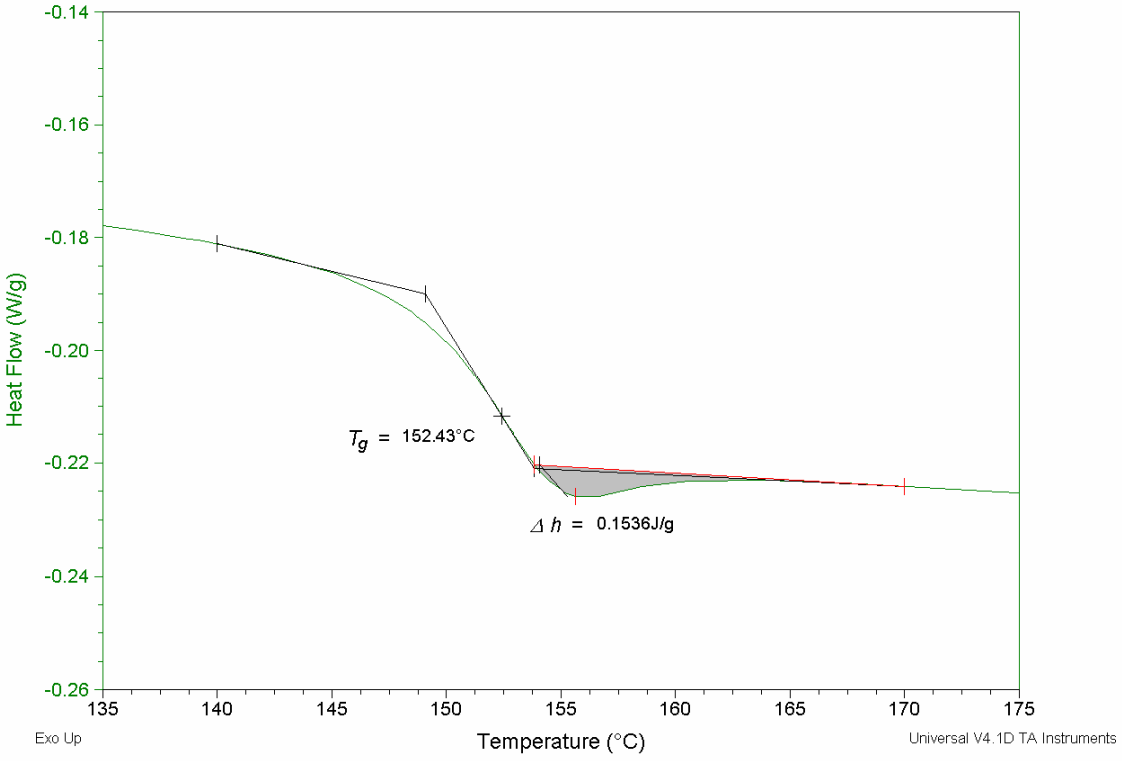

DSC Scan for Specimen 52-T2-01 Tested at 10°C/min

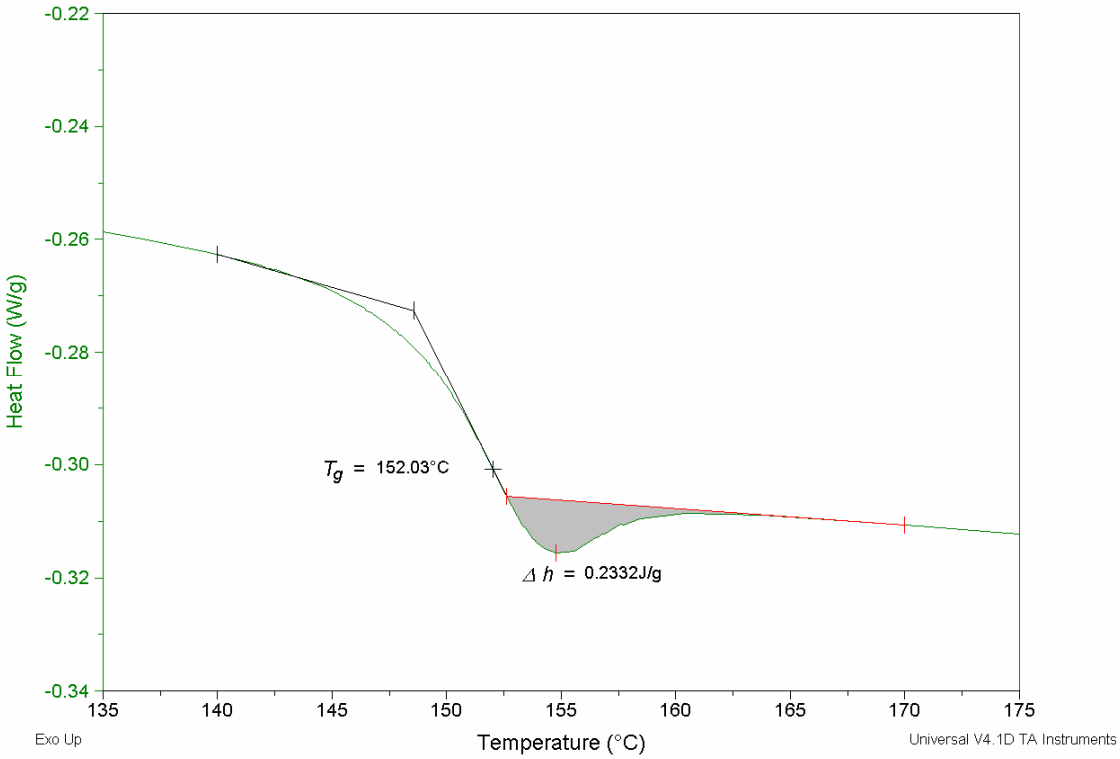

DSC Scan for Specimen 52-T2-02 Tested at 10°C/min

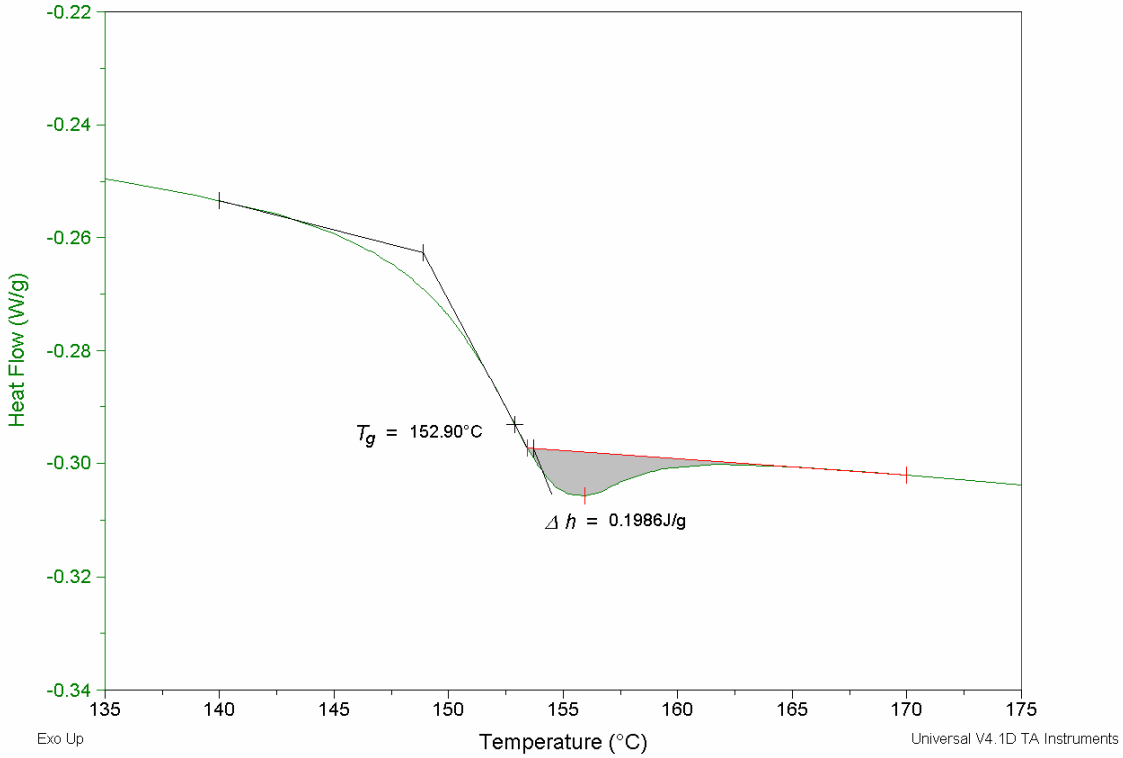

DSC Scan for Specimen 52-T2-03 Tested at 10°C/min

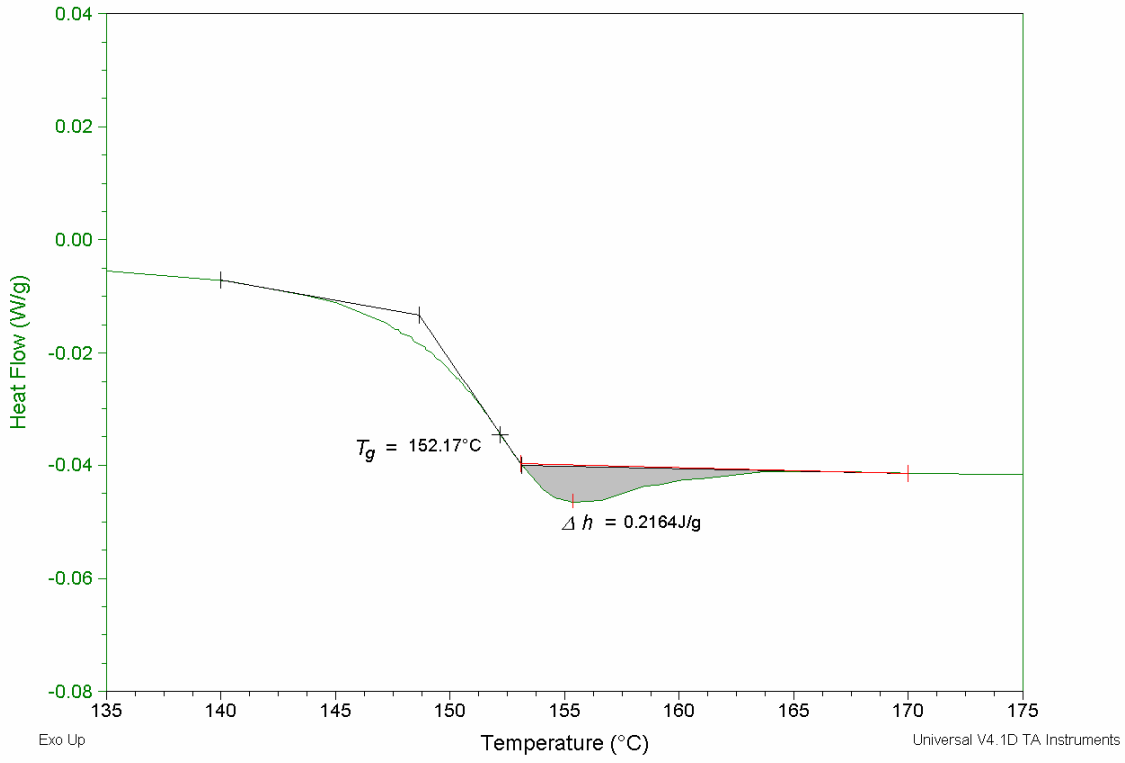

DSC Scan for Specimen 52-T2-04 Tested at 10°C/min

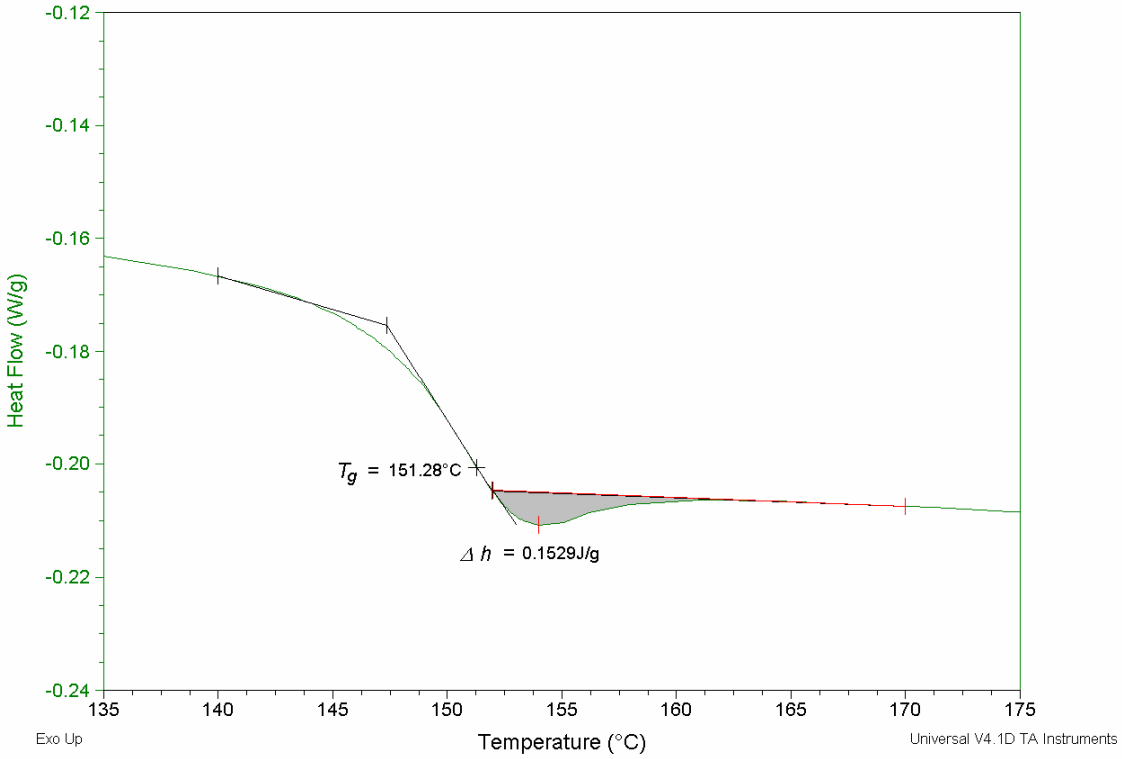

APPENDIX D:

Load-Displacement Plots from Tensile Tests

Load-Displacement Curve for 42-T1 Samples Tested at 2 mm/min

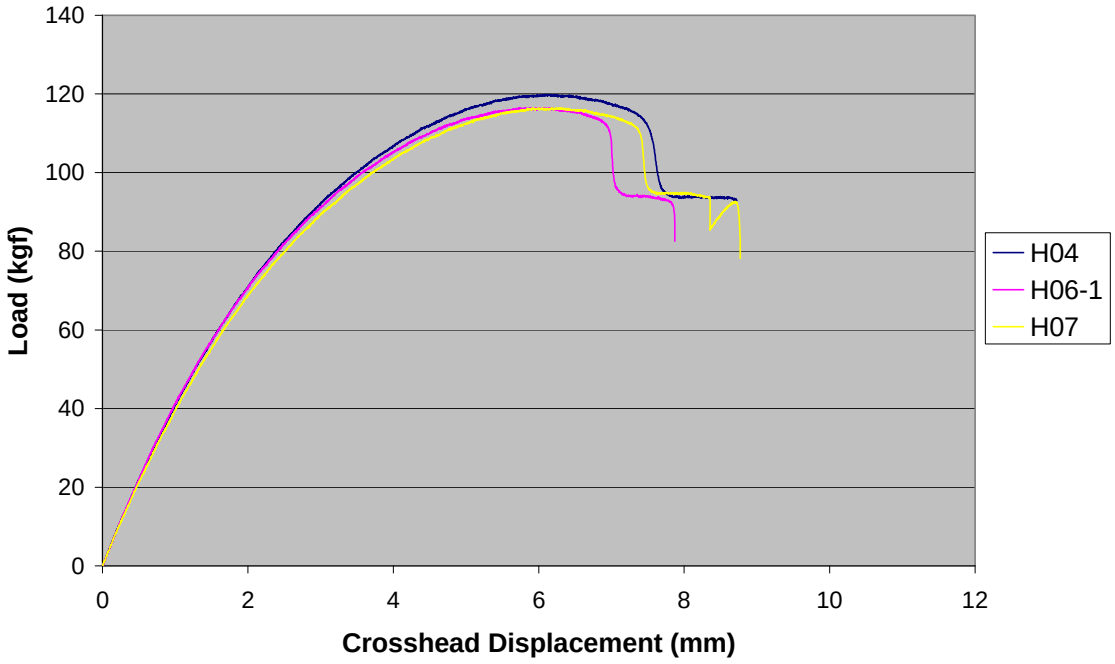

Load-Displacement Curve for 52-T1 Samples Tested at 2 mm/min

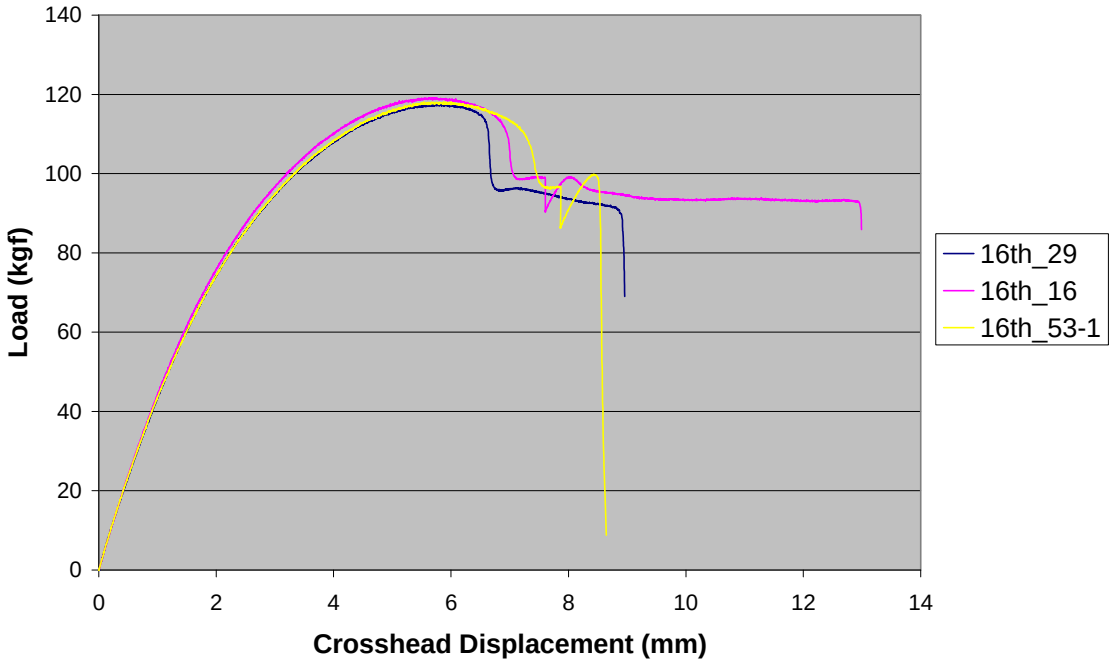

Load-Displacement Curve for 52-T2 Samples Tested at 2 mm/min

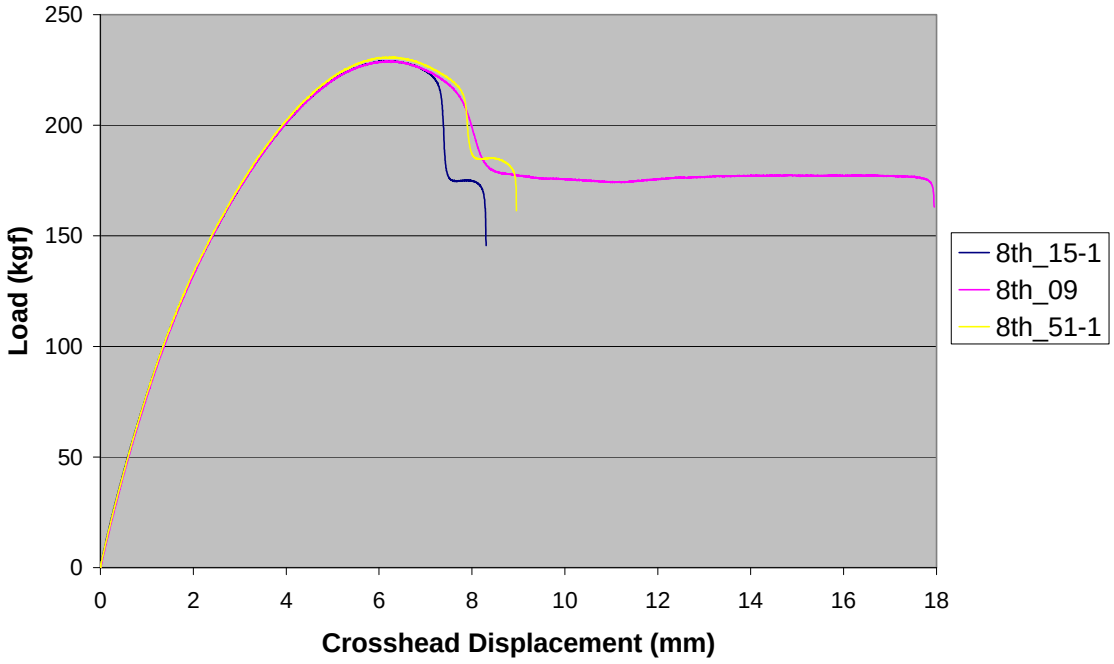

Load-Displacement Curve for 42-T1 Samples Tested at 20 mm/min

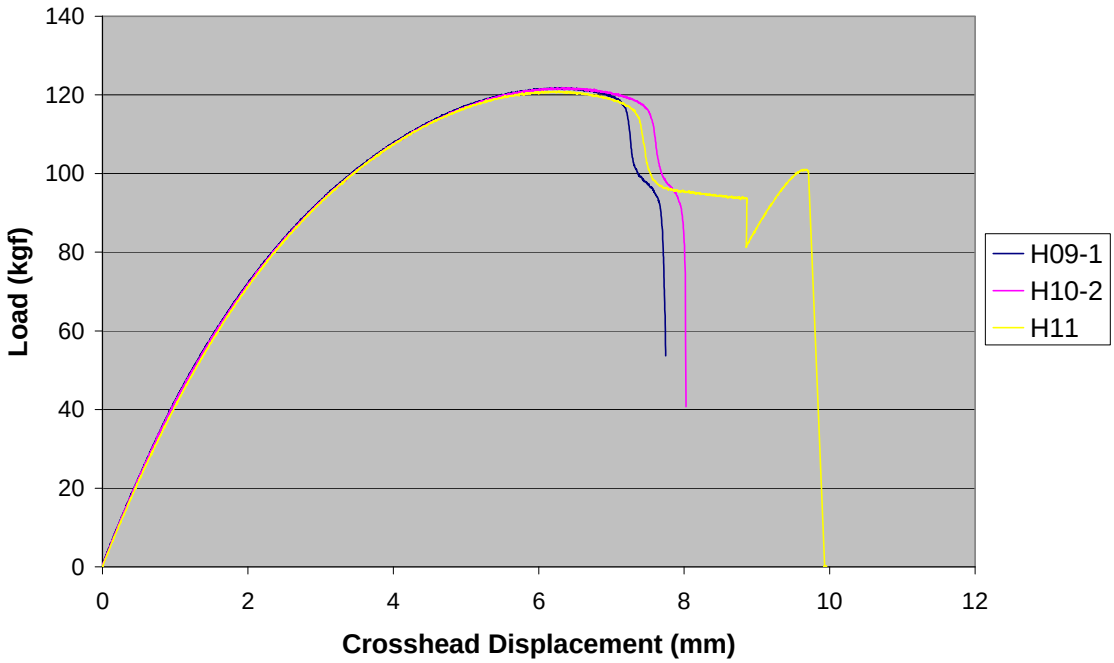

Load-Displacement Curve for 52-T1 Samples Tested at 20 mm/min

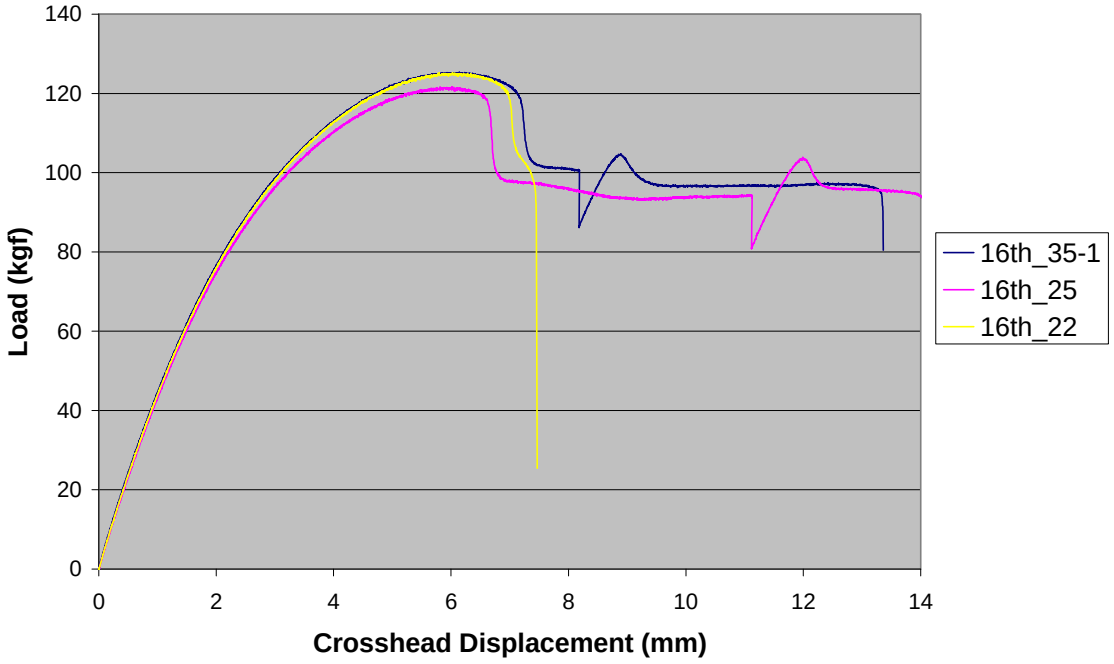

Load-Displacement Curve for 52-T2 Samples Tested at 20 mm/min

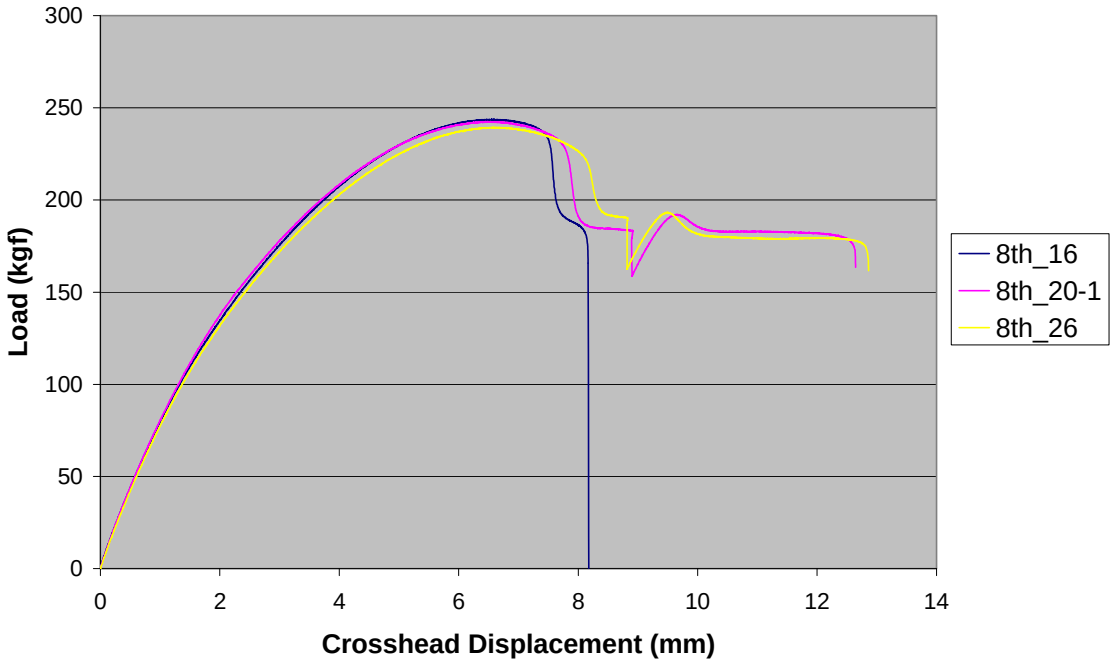

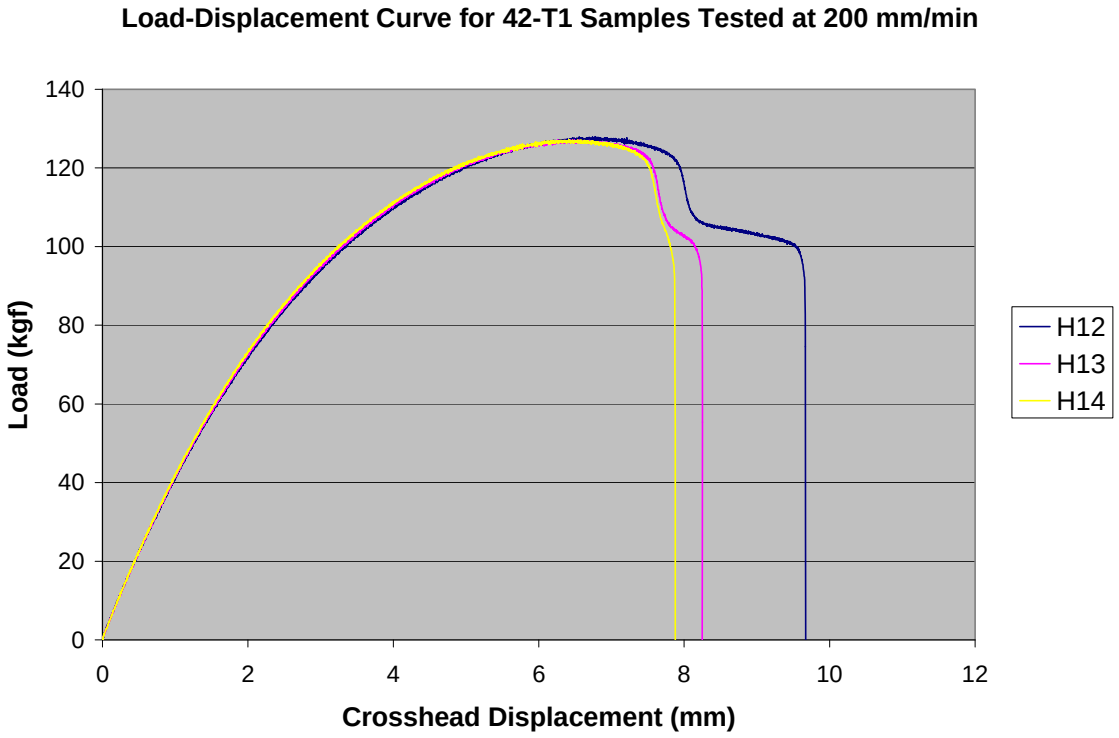
Load-Displacement Curve for 42-T1 Samples Tested at 200 mm/min
Load (kgf)
140
120
100
80
60
40
20
0
0
2
4
6
8
10
12
Crosshead Displacement (mm)
H12
H13
H14

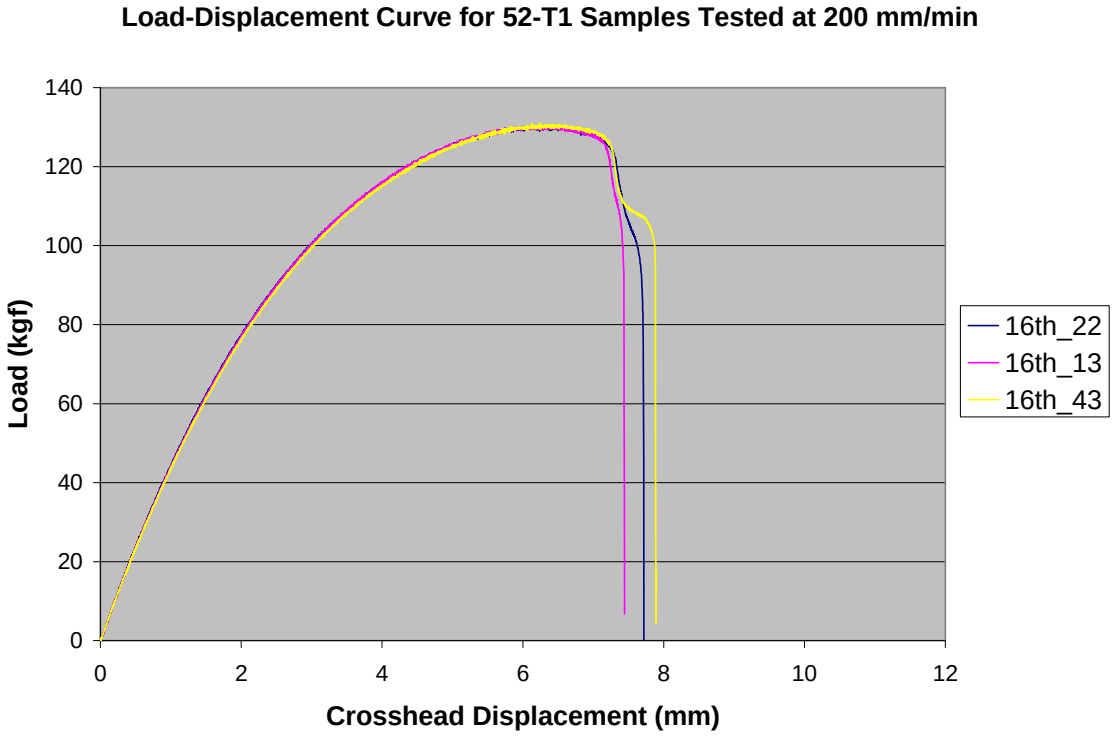
Load-Displacement Curve for 52-T1 Samples Tested at 200 mm/min
Load (kgf)
140
120
100
80
60
40
20
0
0
2
4
6
8
10
12
Crosshead Displacement (mm)
16th_22
16th_13
16th_43

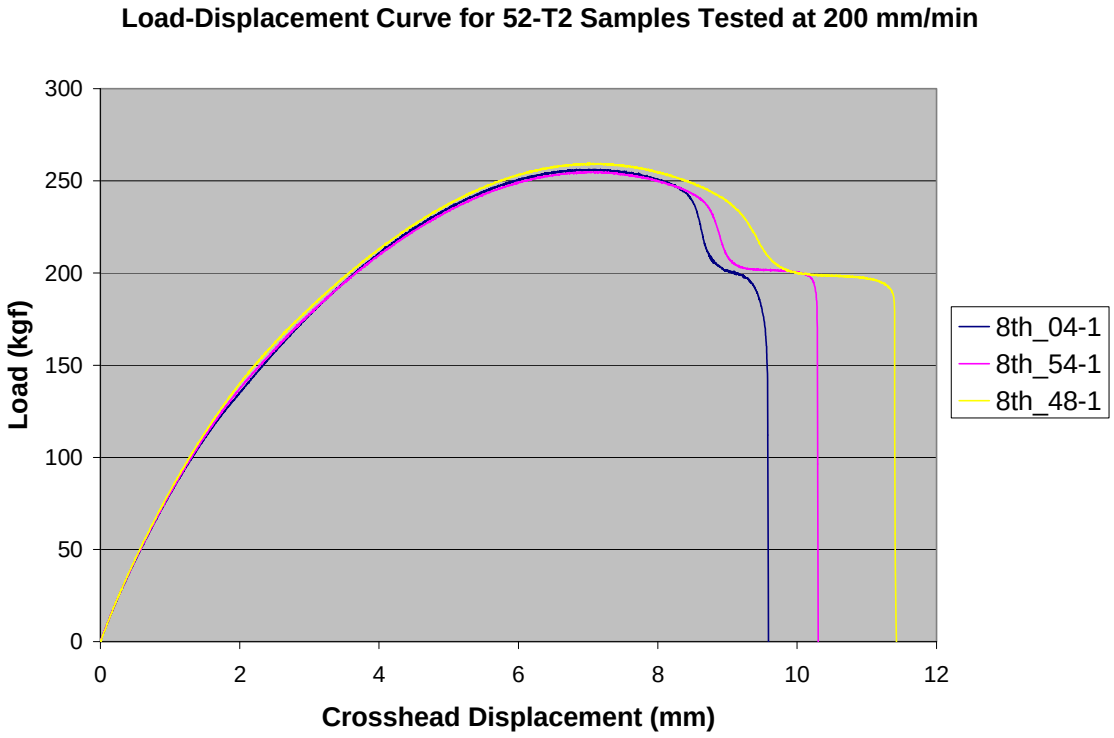
Load-Displacement Curve for 52-T2 Samples Tested at 200 mm/min
Load (kgf)
300
250
200
150
100
50
0
0
2
4
6
8
10
12
Crosshead Displacement (mm)
8th_04-1
8th_54-1
8th_48-1

APPENDIX E:

Engineering Stress-Strain Plots from Tensile Tests

Stress-Strain Curve for 42-T1 Samples Tested at 2 mm/min

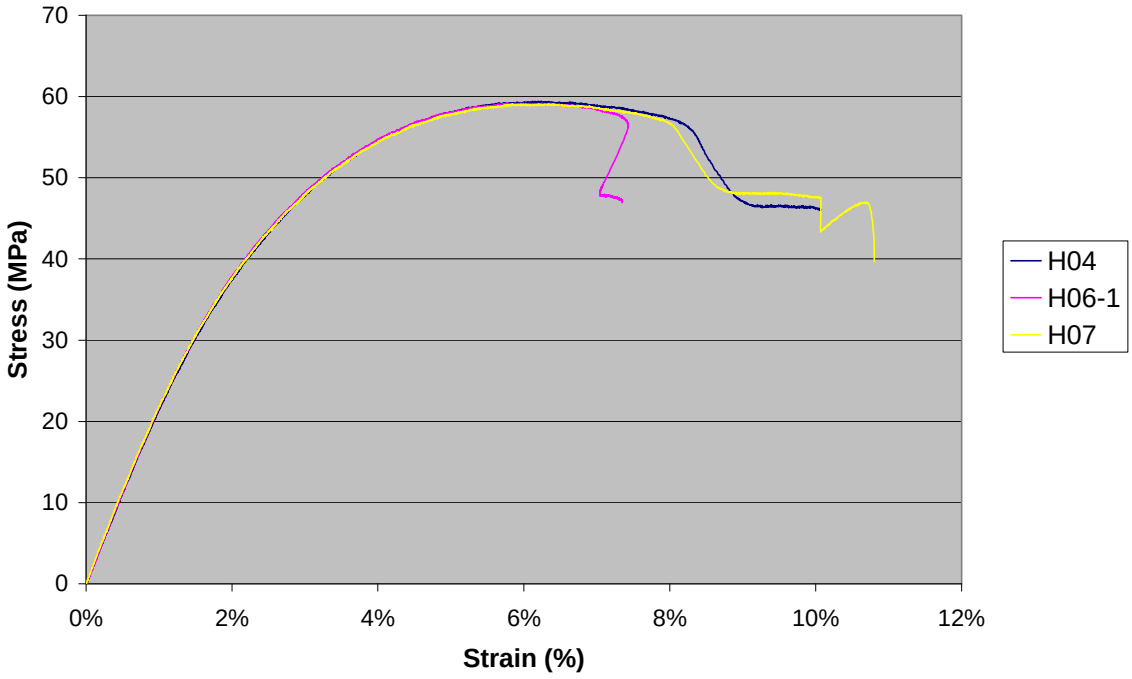

Stress-Strain Curve for 52-T1 Samples Tested at 2 mm/min

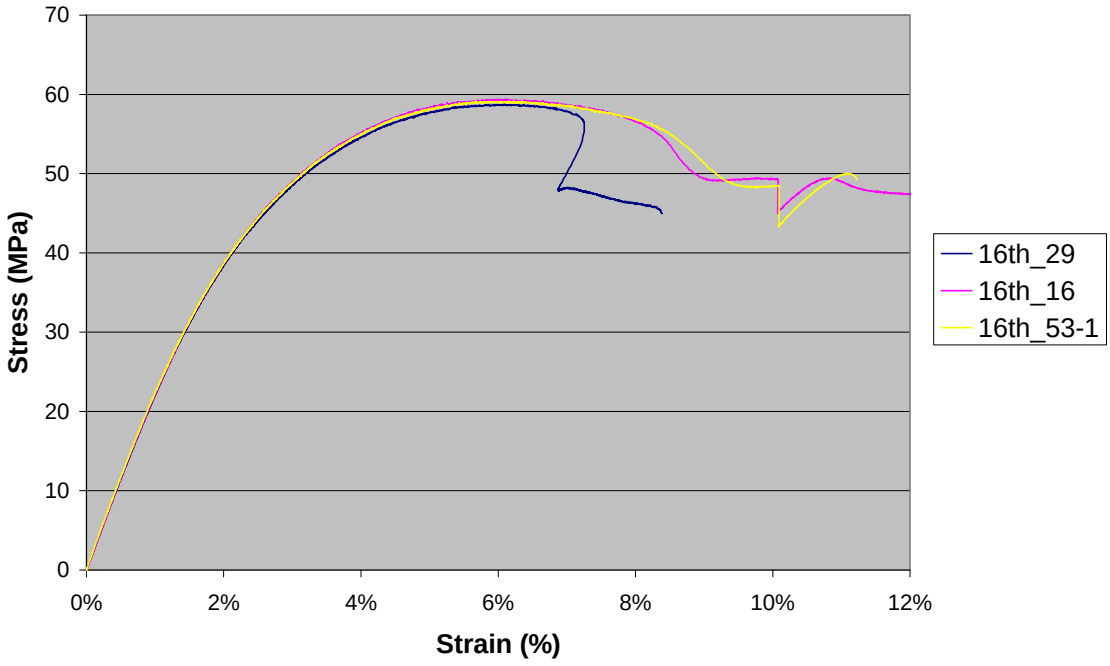

Stress-Strain Curve for 52-T2 Samples Tested at 2 mm/min

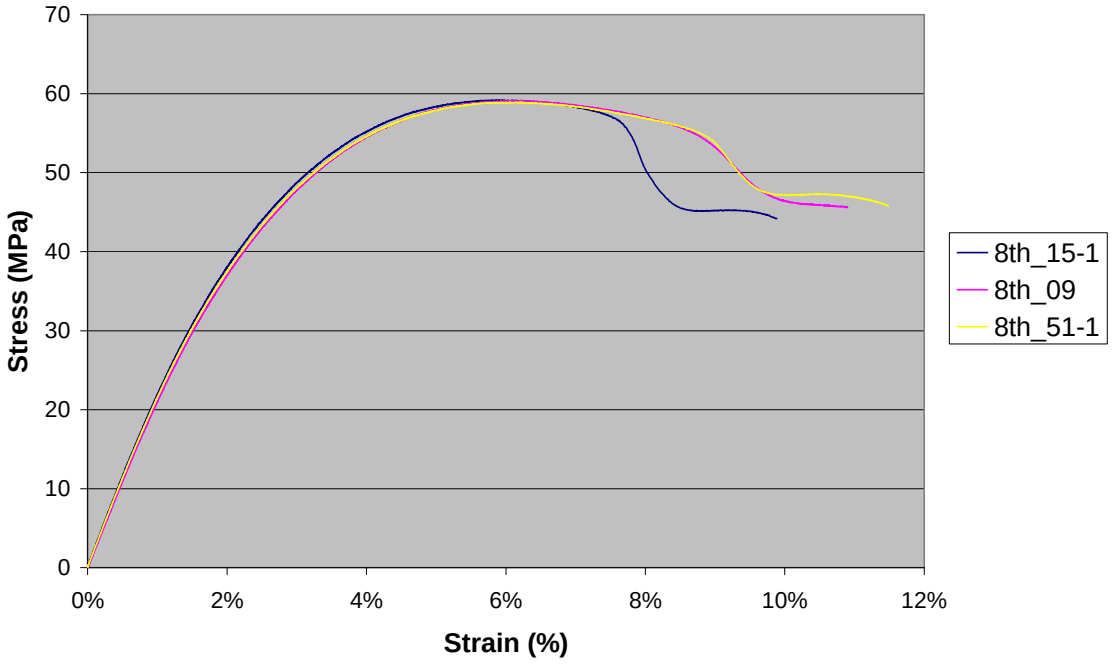

Stress-Strain Curve for 42-T1 Samples Tested at 20 mm/min

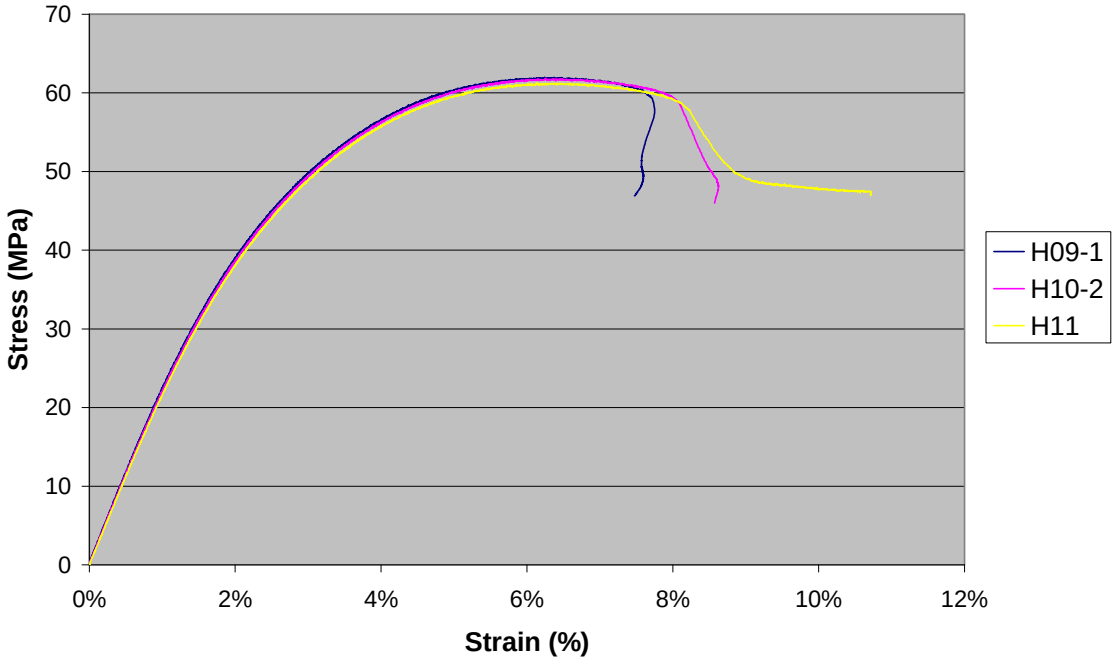

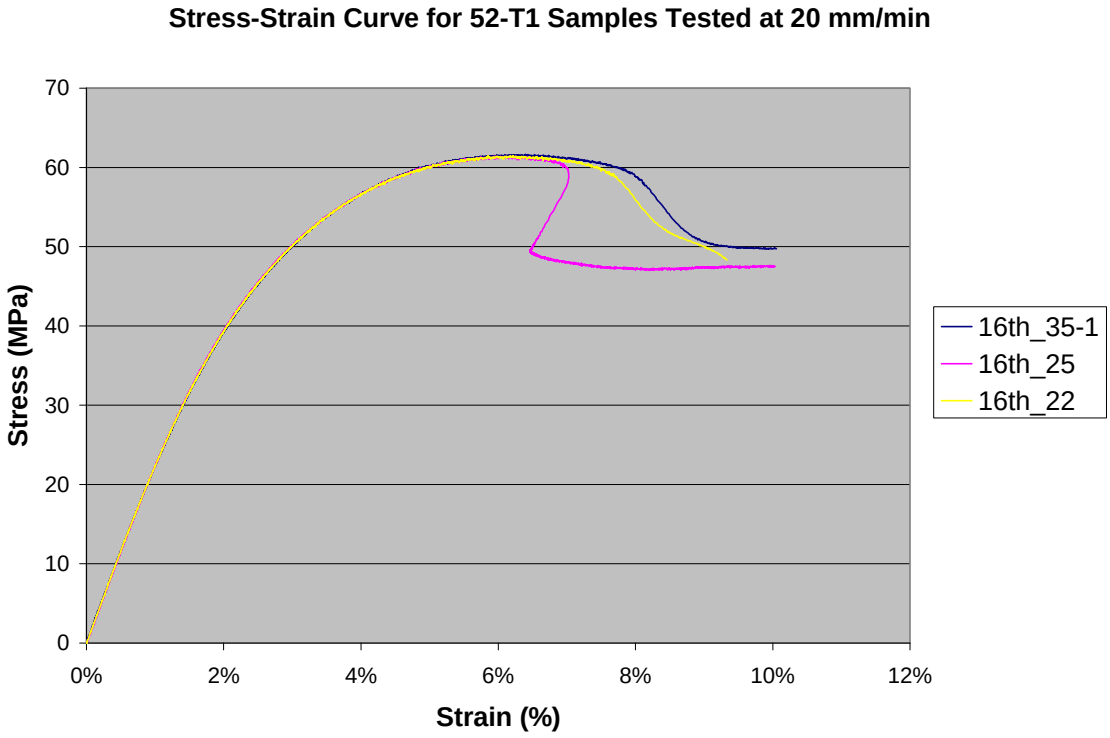
Stress-Strain Curve for 52-T1 Samples Tested at 20 mm/min
Stress (MPa)
70
60
50
40
30
20
10
0
0%
2%
4%
6%
8%
10%
12%
Strain (%)
16th_35-1
16th_25
16th_22

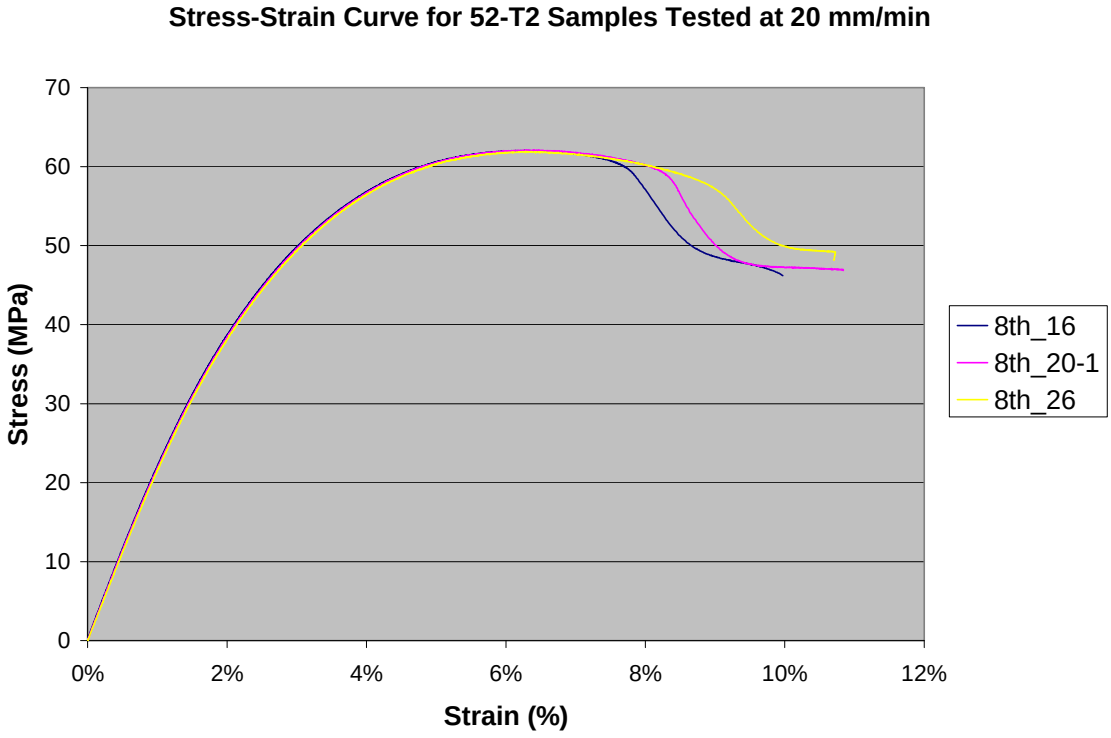
Stress-Strain Curve for 52-T2 Samples Tested at 20 mm/min
Stress (MPa)
70
60
50
40
30
20
10
0
0%
2%
4%
6%
8%
10%
12%
Strain (%)
8th_16
8th_20-1
8th_26

Stress-Strain Curve for 42-T1 Samples Tested at 200 mm/min

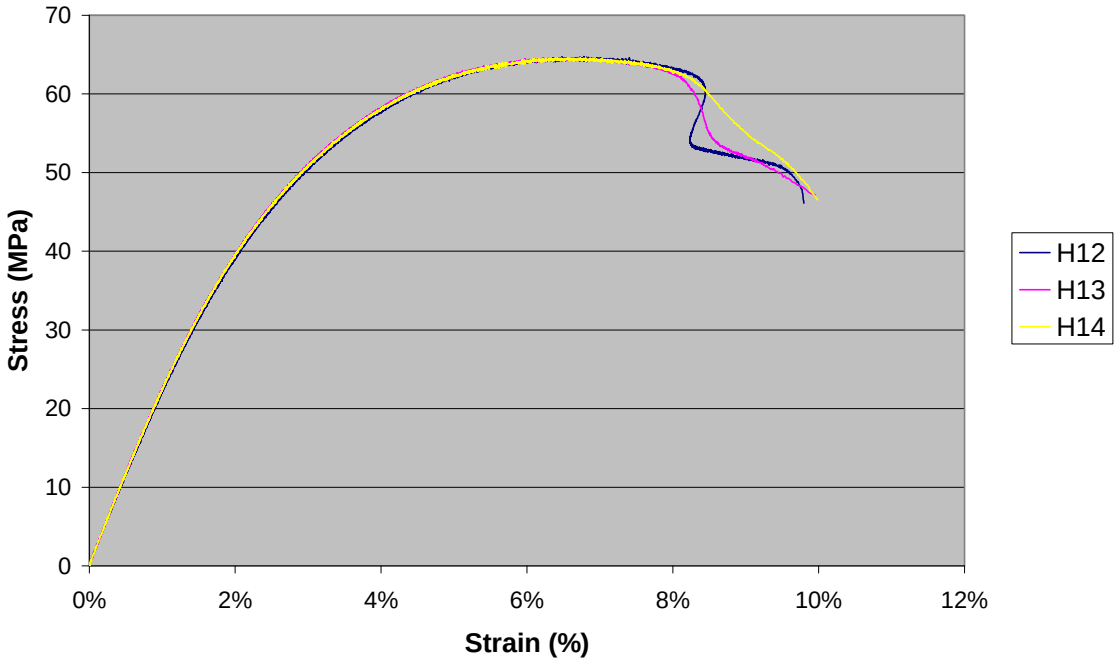

Stress-Strain Curve for 52-T1 Samples Tested at 200 mm/min

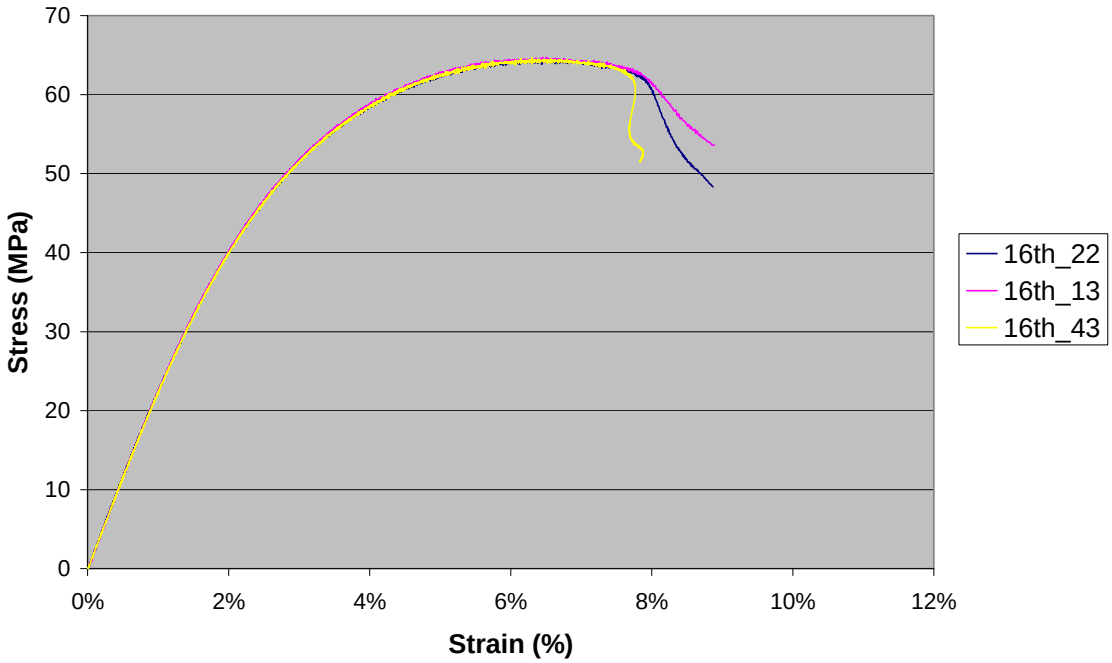

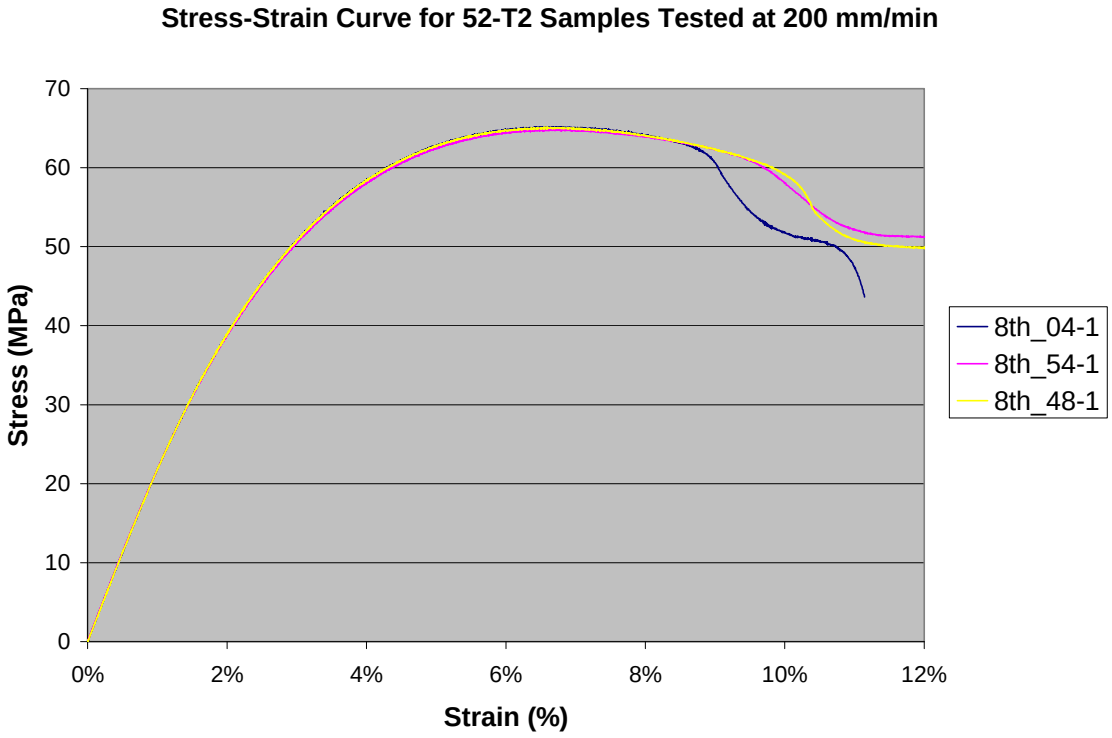
Stress-Strain Curve for 52-T2 Samples Tested at 200 mm/min
Stress (MPa)
70
60
50
40
30
20
10
0
0%
2%
4%
6%
8%
10%
12%
Strain (%)
8th_04-1
8th_54-1
8th_48-1